2009

Study of The Effects of Sodium and Absorber Microstructure for the Development of Cuin1-Xgaxse2-Ysy Thin Film Solar Cell Using an Alternative Selenium Precursor

Vinaykumar Hadagali
University of Central Florida

STUDY OF THE EFFECTS OF SODIUM AND ABSORBER MICROSTRUCTURE FOR THE DEVELOPMENT OF $CuIn_{1-x}Ga_xSe_{2-y}S_y$ THIN FILM SOLAR CELL USING AN ALTERNATIVE SELENIUM PRECURSOR.

By

Vinaykumar V. Hadagali
B.S. Karnataka University, 2000
M.S. University of Central Florida, 2005

A thesis submitted in partial fulfillment of the requirements
for the degree of Doctor of Philosophy
in the Department of Mechanical, Materials and Aerospace Engineering
in the College of Engineering and Computer Science
at the University of Central Florida
Orlando, Florida

Spring Term
2009

Major Professor: Neelkanth G. Dhere

ABSTRACT

Thin film solar cells have the potential to be an important contributor to the world energy demand in the 21st century. $CuInGaSe_2$ thin film solar cells have achieved the highest efficiency among all the thin film technologies. A steady progress has been made in the research and development of $CuInSe_2$ based thin film solar cells. However, there are many issues that need to be addressed for the development of $CuInSe_2$ based thin films solar cells. High price of PV modules has been a biggest factor impeding the growth of photovoltaic modules for terrestrial application. This thesis tries to address the effects of sodium on the CIGSe and CIGSeS thin film absorbers. A progressive increase in the grain size and the degree of preferred orientation for (112) was observed with the increase in the amount of sodium available during the absorber growth. The distribution of sulfur was also influenced by the microstructure of the film. The increase in the grain size influenced the diffusion of sulfur in the CIGSeS thin film absorber. Deposition of silicon nitride alkali barrier was successfully completed. A new selenium precursor, dimethyl selenide was successfully used for the preparation of CIGSe and CIGSeS thin film solar cells. Systematic approaches lead to the optimization process parameters for the fabrication of the thin films solar cells. CIGSeS thin film solar cell with a reduced thickness of ~2 μm and an efficiency of 9.95% was prepared on sodalime glass substrate. The research presented here proves the potential of dimethyl selenide as selenium precursor to prepare device quality CIGSe absorber. The process can be further optimized to prepare highly efficient absorbers. Electron backscattered diffraction technique was used for first time to analyze the CIGSeS thin film absorbers. Kikuchi patterns and EBSD maps were obtained on the polished CIGSeS thin film absorbers. Grains with various orientations in the EBSD maps were clearly observed. However, it can also be observed that some pixels have not been indexed by the

software. This might be due to the departure of crystalline structure of the film from $CuInSe_2$ or the presence of amorphous phases. Data files for indexing and grain orientation of CIGSeS does not exist. However, with the help of lattice parameters and the position of atoms in the base the data file can be created for CIGSeS material.

Dedicated To

"My Beloved Parents"

ACKNOWLEDGMENTS

First and foremost I would like to express gratitude to my advisor Dr. Neelkanth G. Dhere, for his help and support throughout this research work. I enjoyed working under his supervision and appreciate his constant guidance and encouragement. It really was a great experience and an overall growth of personality. I would like to thank Dr. Helge Heinrich, Dr. Kalpathy Sundaram, Dr. Arvinda Kar, Dr. Clovis Linkous and Dr. Christine Klemenz, for serving on my final examination committee and for their invaluable suggestions.

I want to thank Dr. Anant H. Jahagirdar and Dr. Ankur A. Kadam, words cannot truly express my gratitude for all the advice, help and encouragement from them. I thank all my colleagues at PV Materials Laboratory: Shirish A. Pethe, Sachin S. Kulkarni, Parag S. Vasekar and Ashwani Kaul, I would also like to thank my earlier colleagues, Vivek S. Gade, Sachin M. Bet, and Anil U. Pai, Upendra S. Avachat, Bhaskar Kumar, Miss. Jyoti S. Shirolikar and also other colleagues at the Florida Solar Energy Center. I really had excellent six years of my life spent at the PV Materials Lab.

Words cannot truly express my deepest gratitude and appreciation to my parents Vijay A. Hadagali, and Kusuma V. Hadagali, my brother Captain Vikram V. Hadagali, Shantinath R. Ghongadi, Shruti A. Jahagirdar and friends who always gave me their love and emotional support. I would also like to thank my wife, Veena V. Hadagali for her enormous help, support and love.

Finally I would like thank National Renewable Energy Laboratory for funding this research. I would like to thank the following people for their assistance on this project: Dr. Helio Moutinho and Bobby To for EPMA and XRD analysis, Paul Ciszek, Keith Emery and Tom Moriarty of NREL for I-V measurements. I would like to acknowledge AMPAC's Materials

Characterization Facility (MCF). A special word of thanks goes to all the personnel at MCF. I would like to extend my thanks to Haritha Nukala and Hilary Palmer for assistance during the TEM analyses.

TABLE OF CONTENTS

LIST OF FIGURES

LIST OF TABLES

LIST OF ACRONYMS/ABBREVIATIONS

CISe	Copper Indium Diselenide
CIGSe	Copper Indium Gallium Diselenide
CIGSeS	Copper Indium Gallium Selenide Sulfide
CdS	Cadmium Sulfide
i:ZnO	Intrinsic Zinc Oxide
ZnO:Al	Aluminum doped Zinc Oxide
DESe	Diethyl Selenide
DMSe	Dimethyl Selenide
J	Current Density (mA/cm^2)
J_0	Reverse Saturation Current Density (mA/cm^2)
J_D	Dark Current Density (ma/cm^2)
Q	Electronic Charge, 1.6×10^{-19} C
A	Diode Ideality Factor
K	Botlzmann's Constant , 8.61×10^{-5} eV/°C
R_s	Series Resistance (Ohm)
R_{sh}	Parallel or Shunt Resistance (Ohm)
V	Biased Voltage (Volts)
I_L	Photo generated Current (mA)
I_{max}	Maximum Current (mA)
V_{max}	Maximum Voltage (Volts)
W_d	Depletion Width
V_{oc}	Open Circuit Voltage (Volts)
J_{sc}	Short Circuit Current Density (mA/cm^2)
FF	Fill Factor (%)
η	Efficiency (%)
V_b	Built-in Voltage (Volts)
kV	kilo volts
eV	electron volts
EPMA	Electron Probe Micro Analysis

EDS	Energy Dispersive X-ray Spectroscopy
XRD	X-ray diffraction
AFM	Atomic Force Microscopy
SEM	Scanning Electron Microscopy
AES	Auger Electron Spectroscopy
EBSD	Electron Backscattered Diffraction
QE	Quantum Efficiency

1. INTRODUCTION

The growth and development of mankind is always closely related to the availability of energy. In the present scenario, the worldwide supply of energy is based on fossil fuels such as oil, coal and natural gas and also to some extent on nuclear and hydro electric. At present, the world's energy consumption is ~400 quadrillion BTU per year i.e. ~14 Quads/yr, ~85% of which is satisfied by fossil fuels. The world energy consumption is projected to increase by 50% from 2005 to 2030 as result of expanding population and strong economic growth of developing nations (Figure 1.1) [1]. However, some uncertainties exist about the total amount of available fossil fuels and also how long they will be able to meet the growing demand. Also the production of the present energy requirement poses a serious threat to the global environment. Burning of fossil fuels produces ~21.3 billion tonnes of CO_2 per year [2]. A major threat faced by mankind is the harmful effects of global warming due to the accumulation of greenhouse gases in the atmosphere. CO_2 (82%), methane (9%), nitrous oxide (5%), and pollutants (4%) make up the greenhouse gases in the atmosphere [3]. The effect of global warming on climatic changes seems to be multiplying with every passing year. Hence during the last two decades there has been an enhanced interest in the development of clean renewable resources for energy production. The most promising source of clean, safe and abundant energy is the sun. The total solar energy intercepted by the earth's surface in one hour is 14 TWyr. Thus solar has the great potential to meet a large fraction of energy needs.

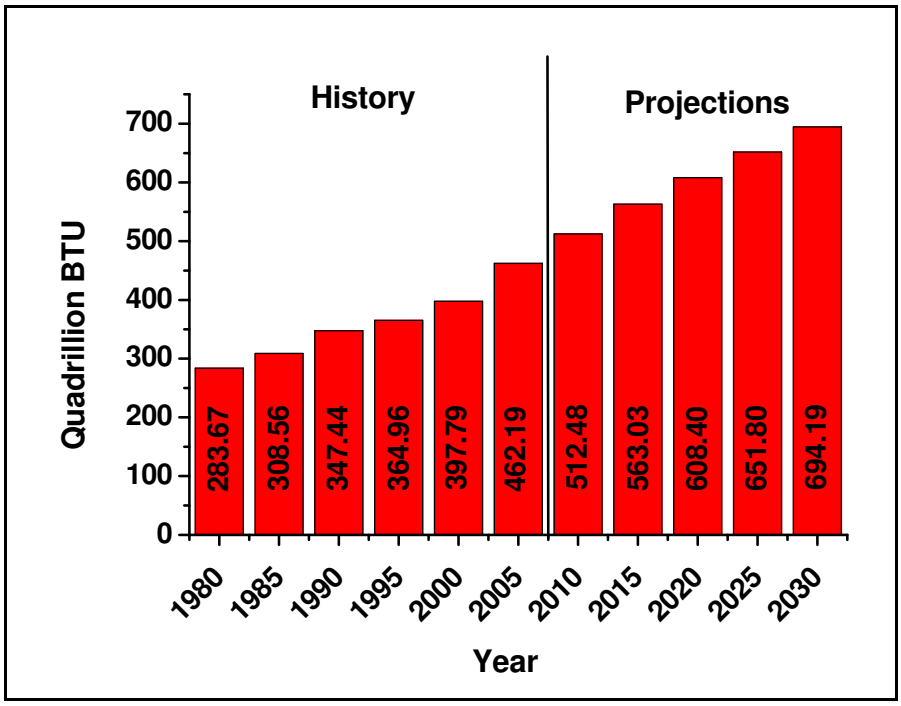

Figure 1.1: World Energy Consumption, 1980 – 2030 [1]

1.1. Photovoltaics (PV)

Photovoltaic is the term used to describe the process of converting sun light into electricity with solar cells which are constructed using semiconductor materials.

1.2. History of Photovoltaics [4 - 7]

- **1839:** Edmund Becquerel, the French experimental physicist, discovered photogalvanic effect in liquid electrolytes
- **1873:** Willoughby Smith of UK discovered photoconductivity of selenium whilst working on submarine cables.
- **1877:** William Grylls Adams and Richard Evan Day of UK discovered that the selenium produced electricity when exposed to light; the first observation of photovoltaic effect in solids.
- **1883:** Charles E. Fritts, an American inventor, made the first selenium based photovoltaic cell that converted sunlight into electricity at an efficiency of <1 %.

- **1904:** Wilhelm Hallwachs discovered that the combination of cuprous oxide and copper is photosensitive.
- **1932:** Audobert and Stora discovered the photovoltaic effect in cadmium sulfide.

- **1954:** First 6% efficient solar cells reported: Si (Bell Lab, USA) and Cu_2S/CdS (Air Force, USA).

- **1960:** Hoffman Electronics achieved 14% efficient photovoltaic cells.

- **1963:** Sharp Corporation, Japan, produces first commercial silicon PV modules.

- **1973:** University of Delaware, USA builds "Solar One" world's first solar powered residence built with Cu_2S solar modules (not c-Si modules).

- **1976:** Christopher Wronski and David Carlson at RCA Laboratories fabricate the first amorphous silicon photovoltaic cells.

- **1977:** The U.S. Department of Energy launches the Solar Energy Research Institute later was renamed the "National Renewable Energy Laboratory", in 1991 a federal facility dedicated to harnessing power from the sun. http://www.nrel.gov/

- **1980:** First thin-film solar cell >10% using Cu_2S/CdS at the University of Delaware (USA). ARCO Solar becomes the first company to produce more than 1 megawatt of photovoltaic modules in one year.

- **1985:** A big year for high-efficiency Si solar cells: Martin Green's team at University of South Wales breaks the 20% efficiency barrier for silicon solar cells under 1-sun conditions.

- **1992:** University of South Florida develops a 15.9% cadmium telluride thin-film solar cell.

- **1994:** The National Renewable Energy Laboratory develops a GaInP and GaAs solar cell with conversion efficiency > 30%. First cell to cross 30% mark.

- **1998:** NREL achieves ~ 19% efficiency $Cu(In,Ga)Se_2$ thin-film solar cell.

- **1999:** Cumulative worldwide installed photovoltaics reaches 1000 MW

- **2008**: NREL achieves ~ 19.9% efficiency $Cu(In,Ga)Se_2$ thin-film solar cell.

1.3. Potential of Solar Energy

The present total energy consumption of the world is ~400 Quads/yr (~14.1 TWyr) [8]. The energy reaching the earth's surface is ~7000 times the present global energy consumption. In Y2005 global energy consumption was 0.014% of the solar energy reaching the earth surface. For the Y2100 the projected global energy consumption is 0.051% of the total solar energy reaching the earth's surface [9]. By the end of this century mankind may possibly run out of fossil fuels. Sun's energy is abundant and clean. If 1% of the unused land area is used ~4 times more electricity could be produced as compared to the fossil fuels and nuclear power [9]. Hence technology has to be developed so as to efficiently produce and store the electricity from sun.

1.4. Goals for Today's PV Research

- Use less semiconductor material: This can be achieved by manufacturing / producing thinner cells/modules.
- Develop processes which will utilize cheaper semiconductor materials.
- Improve solar cell performance.
- Improve Production Yield: Reduce the number of cells or modules being rejected by the quality control.
- Reduce waste in semiconductor and cell fabrication.
- Increase solar cell flux on the solar cells by using concentrators without increasing cost or optical losses too much. In this way, less semiconductor material is used.
- Increase solar radiation utilization by absorbing more of the spectrum efficiently.
- Increase the manufacturing processes speed and hence the throughput.
- Simplify processing steps and reduce equipment costs.

- Improve reliability and durability of the PV Modules and systems.

1.5. Status of Photovoltaics

1.5.1. PV Market Size and Growth

World photovoltaic (PV) market installations reached a record high of 2,826 megawatts in 2007. This is an increase of 62% over the previous year. Figure 1.2 represents the market share of the regions contributing to the rise of PV. Spain recorded the highest growth of 480% and US market share increased by 57%. World's overall solar cell production reached a consolidated figure of 3436 MW in the year 2007 [10]. Figure 1.3 and Figure 1.4 represent world cumulative PV production from 1984-2007 and global cumulative PV capacity (policy driven scenario) respectively. The production of PV jumped an impressive 50% from 2521 megawatts in Y2006 to 3800 megawatts in Y2007. At the end of Y2007 the cumulative global production stood at 12,400 megawatts. PV production has been doubling every two years, making it the world's fastest-growing energy source (Figure 1.3) [11]. By the end of 2012 a global cumulative capacity of 44 GWp could be achieved. PV is clearly on the way to becoming a major global energy source (Figure 1.4) [12].

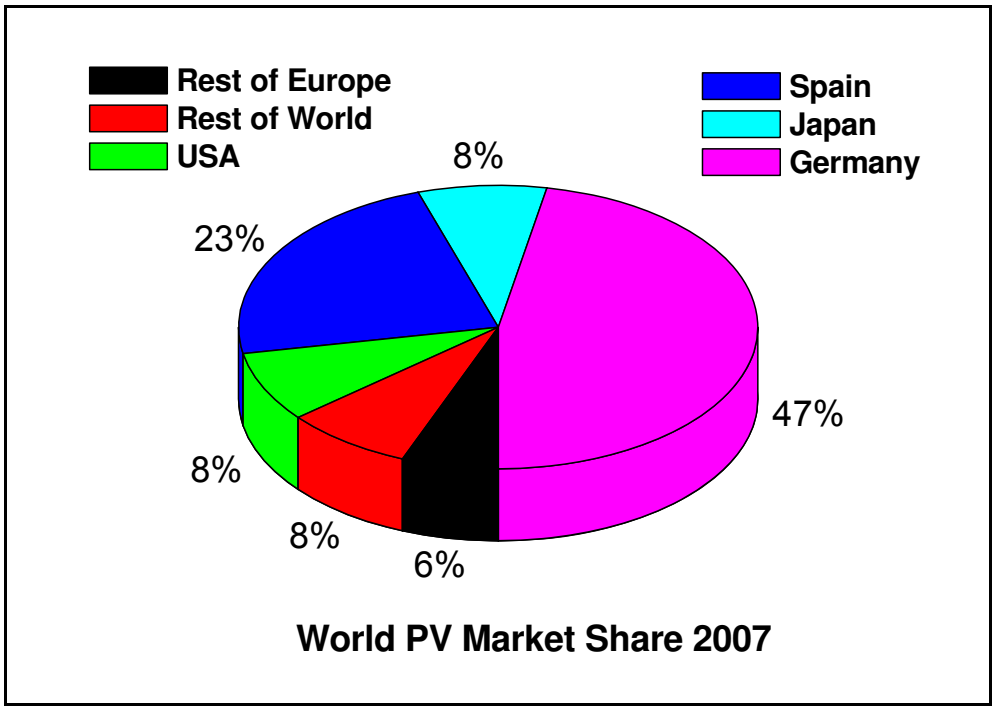

Figure 1.2: World PV Market Installation Share 2007 [10]

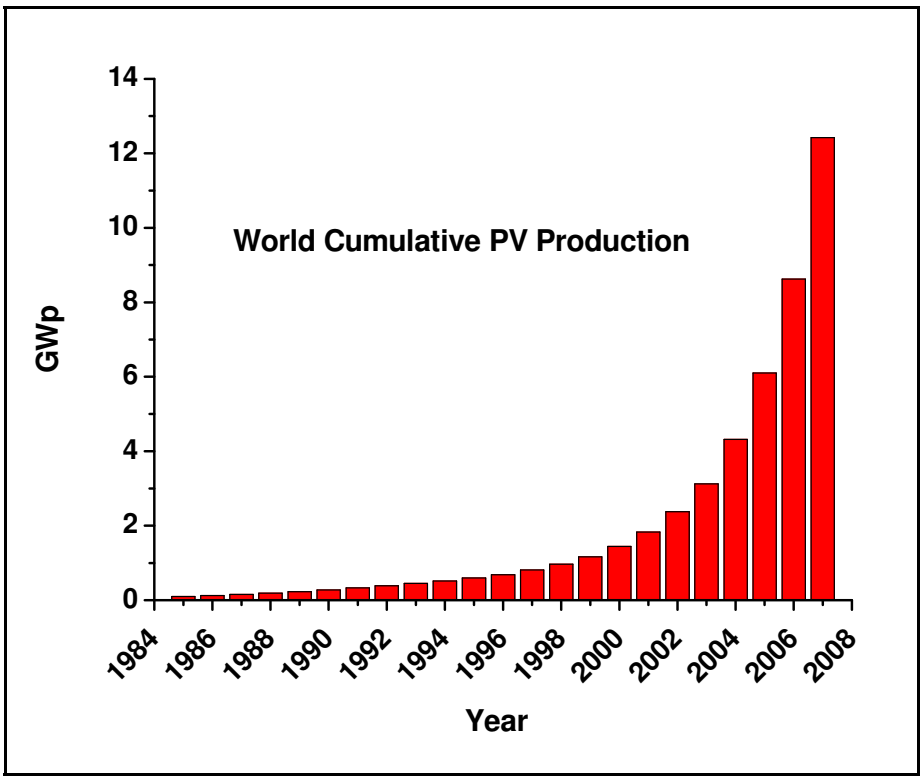

Figure 1.3: World Cumulative PV Production [11]

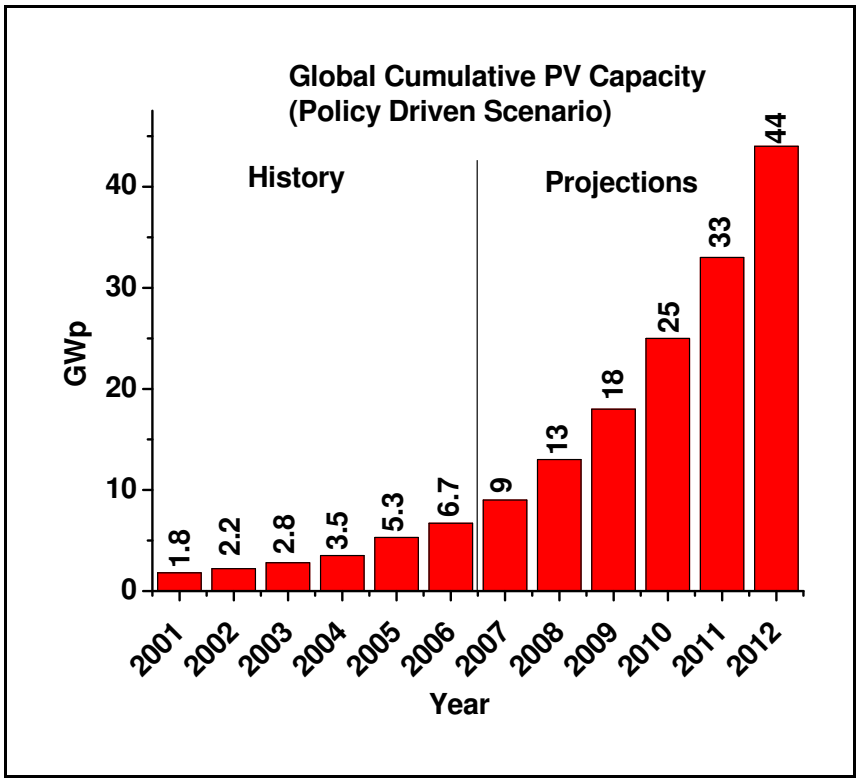

Figure 1.4: Global Cumulative PV Capacity [12]

1.5.2. Crystalline Silicon vs. Thin-films

Crystalline silicon (c-Si) solar cells are also known as the first generation solar cell technology. The present solar cell market is dominated by silicon based solar cells with the lion's share of 93% while market share of thin film modules is 7% [13]. Laboratory efficiency of 24.7% [14] has been achieved for small area crystalline silicon (c-Si) cell while the highest reported module efficiency is 22.7% (designated illumination area: 778 cm^2) [15] and 20.1% (aperture area: 16300 cm^2) [16]. The silicon solar cells industry has grown approximately 50% in the recent years. This rapid growth has created shortage of polysilicon. The spot price of solar grade silicon rose more than 300% in the last two years *($145 in 2006 to $515 in June 2008*) [17]. At present due to high spot price of polysilicon, wafer costs make up ~75% of the total cell cost [17]. High price of PV modules has been a biggest factor impeding the growth of

photovoltaic modules for terrestrial application. Silicon is an indirect bandgap semiconductor with a bandgap of 1.12 eV and an absorption coefficient $\alpha = \sim 10^2$ cm^{-1}. Silicon being an indirect bandgap semiconductor requires an additional energy provided by phonon in the form of lattice vibration along with the energy of the photon to transfer an electron from the valence band to the conduction band. Therefore silicon solar cell requires higher thickness to absorb sunlight. The thickness of silicon based solar cells for absorption of most of the solar spectrum is 100–200 μm. On the other hand several materials such as CdTe, $CuInSe_2$ ($\alpha = \sim 10^5$ cm^{-1}), a-Si:H possess direct bandgap and hence are used in thin film solar cells that have the thickness of 1–3 μm. Thus c-Si cells require ~100 times more material to absorb a given fraction of sunlight compared to thin film semiconductors. Therefore, silicon requires higher thickness to absorb sunlight. Thus c-Si cells require ~100 times more material to absorb a given fraction of sunlight compared to thin film semiconductors. Thicker semiconductor material means higher material volume and also a higher quality material because of the longer paths that the electrons excited by the photons must travel before they are delivered to the external circuit to produce useful work. Thin film solar cells can tolerate impurities thus needs less expensive purification of raw materials. The other advantage of thin film solar cells cadmium telluride (CdTe) and $CuInGaSe_2$ (CIGSe) is low thermal budget. The CIGSe thin films are prepared/manufactured at 200-600 ºC whereas the c-Si solar cells need wafers that are produced at temperatures of ~1400 ºC [4]. The thin film solar cell/modules manufacturing process can be designed such that they are deposited sequentially on moving substrates as in a continuous in line process. This minimizes handling and facilitates automation.

1.5.3. Thin-Film Solar Cells

The major concern in the photovoltaic industry is to reduce cost per peak watt below $1.00 to make the technology economically viable. The present-day c-Si solar cell technology is approaching its lower limit in terms of production costs. However, to meet the ever increasing energy demand new and cost effective solar cell technology must be developed. Thin film solar cells/modules (second generation solar cells) are being developed to reduce the cost of PV energy conversion. The three major players in the thin film market are (i) Amorphous hydrogenated Silicon (a-Si:H), (ii) Cadmium Telluride (CdTe) and (iii) Copper Indium Diselenide ($CuInSe_2$) and its alloys . Among the three, $CuInSe_2$ based solar cells have reached the highest efficiency of 19.9% [18] on small area and 13.4 ± 0.7 % [19] on modules. The highest reported efficiency for small area CdTe thin film solar cell is 16.5 ± 0.5 % [20]. In 2008, the average efficiency of CdTe modules manufactured by First Solar was 10.6% and is expected to go up to 12% by 2012 [21]. The highest reported efficiency for a-Si:H tandem (a-Si/a-Si/a-Si:Ge) module is 10.4 ± 0.5 % [22]. When exposed to sun these cells suffer a significant degradation in their power output. The mechanism of degradation is called the "*Staebler-Wronski Effect"*.

$CuInSe_2$ based solar cells are being considered to be one of the most promising thin film technology because of the following properties: radiation resistant, high absorption coefficient, long term durability. Figure 1.5 shows the present market share (Y2008) and the projected market share (Y2015) for the various thin film solar cells. As of Nov 2008 there are ~40 thin film PV companies in the US. The number of $CuInSe_2$ based companies is ~15 [23].

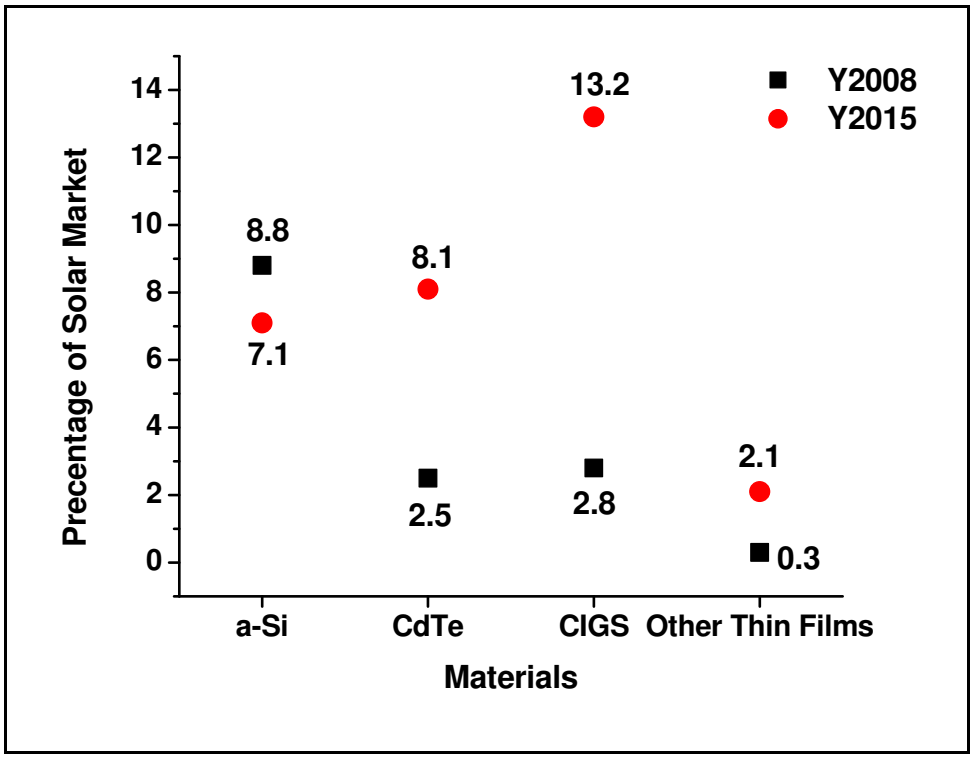

Figure 1.5: Percentage of thin film solar cell (Y2008 vs Y2015) [24]

2. PHYSICS OF SEMICONDUCTOR AND SOLAR CELLS

2.1. Semiconductor

Materials can be classified into three categories: metals, semiconductor and insulators. In metals, the conduction band and the valence band overlap, there is no bandgap and the valence band is partially filled. Since there are numerous empty levels, electrons are free to move under the influence of an electric field. i.e. In an insulator at room temperature, the valence band is completely filled with bound electrons and the conduction band is almost unoccupied. The bandgap is so large that the electrons cannot accelerate under the influence of an electric field. In semiconductors, the valence band is completely filled at 0 ºK while the bandgap is smaller than that of the insulator. The thermal energy, kT at room temperature can excite some electrons from the valence band into the conduction band. The conduction band has many empty energy states and hence the electrons are free to accelerate under the influence of an electric field. Thus, the conductivity of a semiconductor lies in between those of metals and insulators.

The semiconductors can be classified as intrinsic or extrinsic. An intrinsic semiconductor or an undoped semiconductor is pure with a very low concentration of impurities. When an intrinsic semiconductor is doped with impurities it is known as an extrinsic semiconductor. An extrinsic semiconductor can be classified as n-type and p-type. An intrinsic semiconductor doped with donor impurities that provide extra electrons is known as n-type and that doped with acceptor impurities that provide extra holes is known as p-type.

2.1.1. p-n Junction

A *p*-*n* junction is formed when a *p*-type semiconductor and an *n*-type semiconductor are electrically connected. The *p*-*n* junctions can be classified as homojunction and heterojunction.

2.1.1.1. Homojunction

Homojunction is the interface formed between a *p*-type and an *n*-type of a similar semiconductor material (Figure 2.1).

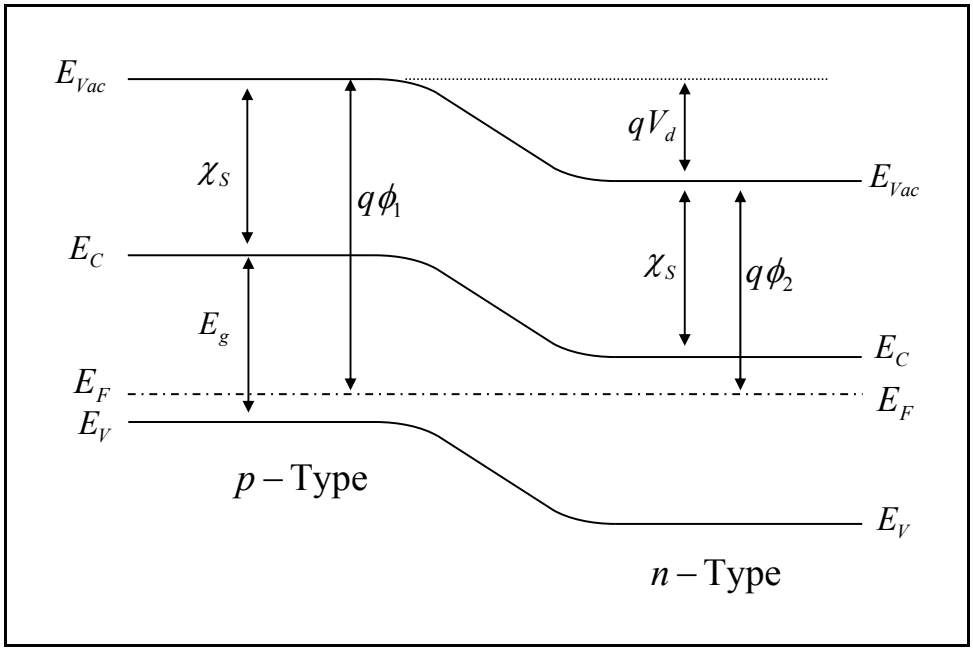

Figure 2.1: Energy band diagram of homojunction

Where, E_{vac} : Vacuum level,

E_C : Conduction band bottom edge,

E_V : Valence band top edge,

E_F : Fermi level,

E_g : Bandgap Energy,

χ_s : Electron Affinity

Φ_d : Diffusion Potential and

Φ_{wp} and Φ_{wn} : Work functions for *p* and *n* side respectively.

When a *p*-*n* junction is formed, a large carrier concentration gradient at the junction causes carrier diffusion. Holes from the *p*-region diffuse into the *n*-region and electrons from the *n*-region diffuse into the *p*-region. The diffusion is momentary and the carriers recombine. As the exchange and recombination begins, electrons leave behind immobile, positively charged donor ions in the *n*-region and the holes leave behind immobile, negatively charged acceptor ions in the *p*-region. This leads to the formation of a negative space charge in the *p*-region near the junction and a positive space charge in the *n*-region near the junction. This space charge region is void of any mobile charge carriers and hence is called the depletion region. An electric field is developed across this depletion region (Figure 2.2) which creates a potential barrier across the junction. When equilibrium is reached the opposing field becomes sufficiently large so that the hole and electron currents reduce to zero. This potential is known as built in voltage (V_B), given by [25]:

$$V_B = (kT/q)\ln\left(N_A.N_D/n_i^2\right) \tag{2.1}$$

where, N_A and N_D : Acceptor and donor concentrations respectively,

n_i : Intrinsic carrier concentration.

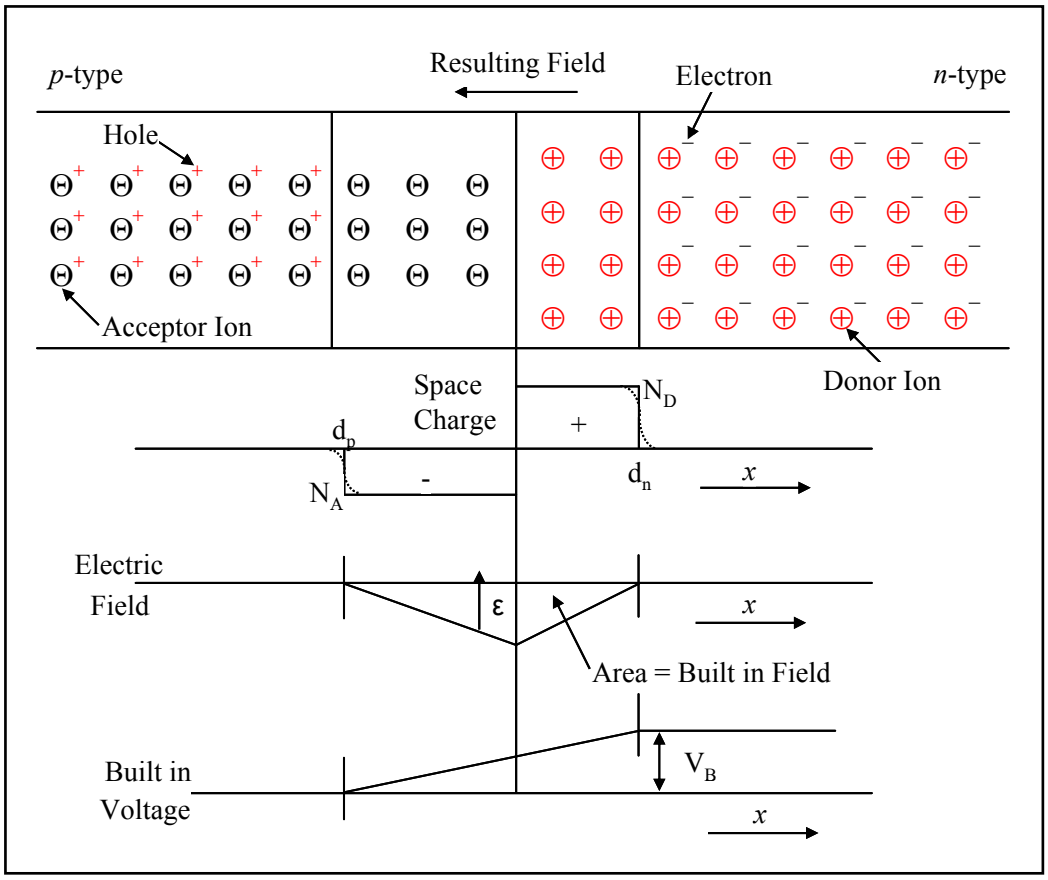

Figure 2.2: Space charge region, electric field and built in potential when *n* and *p* type semiconductor are brought in intimate contact.

At equilibrium,

Electron current density, $J_n = \mu_n . n . \partial E_F / \partial x = 0$ (2.2)

Hole current density, $J_p = \mu_p . p . \partial E_F / \partial x = 0$ (2.3)

where μ_n and μ_p : Electron and hole mobility respectively,

n and *p* : Electron and hole concentration respectively.

Impurity concentration and total voltage which is the sum of built-in voltage and applied voltage determine the width of the depletion region. At equilibrium the applied bias is zero. Hence the depletion width (W_d) [26].

$$W_d = \sqrt{\frac{2\varepsilon_s V_B (N_A + N_D)}{qN_A N_D}} \tag{2.4}$$

where, ε_s is permittivity of the material.

Under non-equilibrium condition when voltage (V_a) is applied across the p-n junction the above equation modifies as [26].

$$W_d = \sqrt{\frac{2\varepsilon_s (V_B - V_a)(N_A + N_D)}{qN_A N_D}} \tag{2.5}$$

2.1.1.2. Heterojunction

Heterojunction is the interface formed between two dissimilar semiconductor materials with different bandgaps, electron affinities and work functions. Figure 2.3 shows the example of two semiconductors and their important parameters before being joined together. The band bending which occurs after the two semiconductors are joined is shown in Figure 2.4. Discontinuity may occur at the junction between valence and conduction bands. It can be seen that a spike has appeared in the conduction band and a cliff in the valence band at the junction due to band bending. A spike in the conduction band is the result of properties specific to the material such as the electron affinity (χ) and the cliff in the valence band is a result of difference

in energy bandgap. Presence of spike and cliff limit electron current that flows from *p* to *n* region when light is incident on the solar cell.

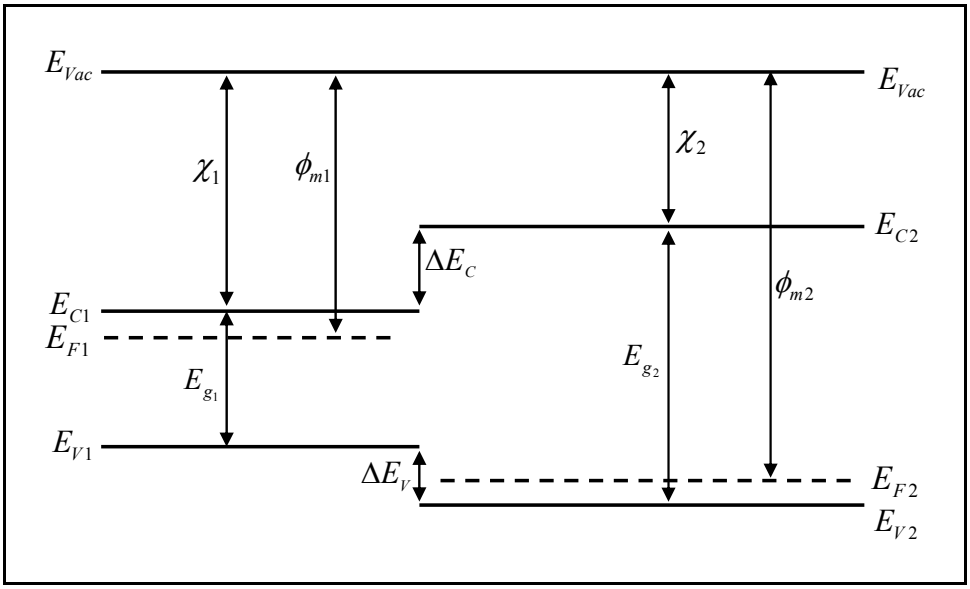

Figure 2.3: Energy band structure of isolated semiconductors

where, E_{g1} and E_{g2} : Bandgap

φ_{m1} and φ_{m2} : Work Function

χ_1 and χ_2 : Electron Affinity

ΔE_C : Conduction band offset

ΔE_V : Valence band offset

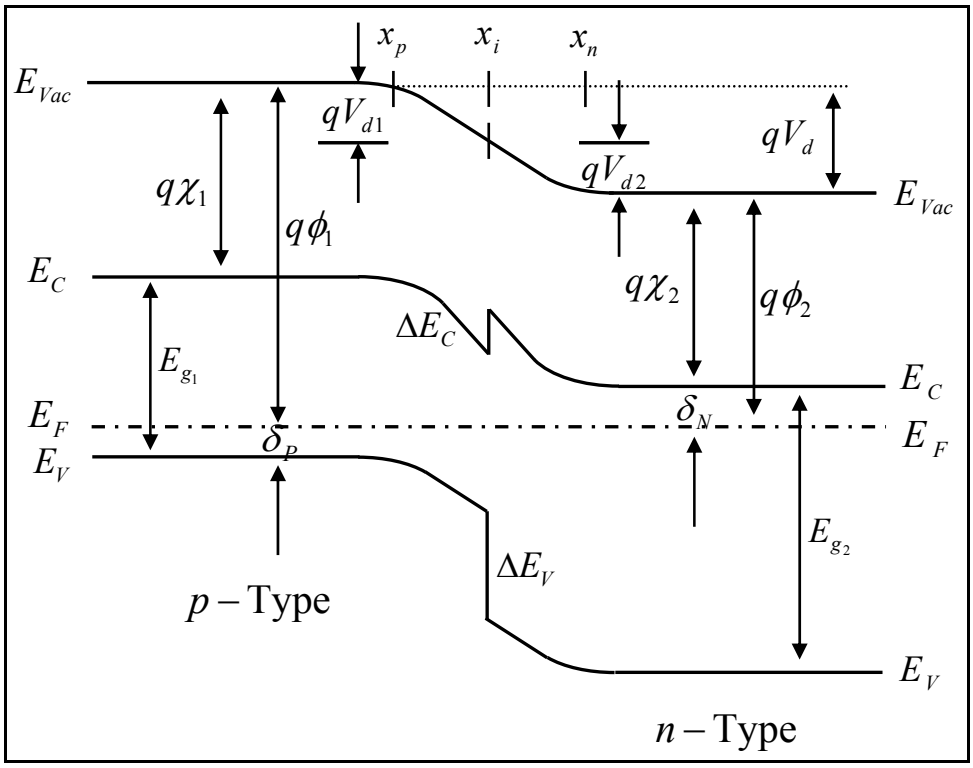

Figure 2.4: Energy band diagram of heterojunction

where, E_{g1} and E_{g2} : Bandgap

$q\varphi_1$ and $q\varphi_2$: Work Function

$q\chi_1$ and $q\chi_2$: Electron Affinity

2.2. Solar Cell

A solar cell is a device that converts sunlight into electricity. When light is incident on the semiconductor photons with energy greater than the bandgap (E_g) are absorbed and the photons with energy less than the bandgap (E_g) are transmitted. The absorbed photons contribute to the cell output.

The phenomenon of solar energy conversion involves the processes of absorption of photons, generation of carriers, diffusion of the minority carriers to the junction, collection of the separated carriers at the external contacts, and finally the utilization of the power generated. In a

solar cell the absorbed photons create electron-hole pairs on both sides of the junction. The electron-hole pairs generated within the diffusion length of the p-n junction region are separated by the built-in field at the junction. Diffusion length is the average distance a charge carrier can travel before getting recombined. The minority charge carriers then are swept across the junction by drift. The field-driven movement of the free carriers within the built in field is called drift. The amount of time the charge carriers generated away from the electric field remain active is called their lifetime. If the charge carriers diffuse to the built-in field within the lifetime it can be propelled to the opposite side. The charge carriers are the majority charge carriers once they are on the other side of the junction. These charge carriers are conducted to the contacts. This results in a photo generated current to flow through the external circuit.

2.2.1. Solar Spectrum

Solar constant is defined as the intensity of solar radiation in the free space at the average distance of earth from sun. The value of solar constant is 1353 W/m^2. Air mass is defined as the degree to which atmosphere affects the solar spectrum received by the earth surface. Air mass zero (AM0) condition describes the solar irradiance in space, where it is unaffected by the earth's atmosphere. The air mass condition (AM1) represents the sunlight at the earth's surface when the sun is at the zenith. The incident power is 1000 W/m^2. The difference between AM0 and AM1 is caused by the atmospheric attenuation, mainly due to scattering by airborne dust and aerosols, to infrared absorption in the water vapor and to ultra violet absorption in the ozone region. Generally the performance of solar cells is evaluated at AM 1.5 condition corresponding to the solar constant of 1 kW/m^2 since AM 1.5 conditions simulate amount of sunlight that the photovoltaic modules are exposed to for most of the day.

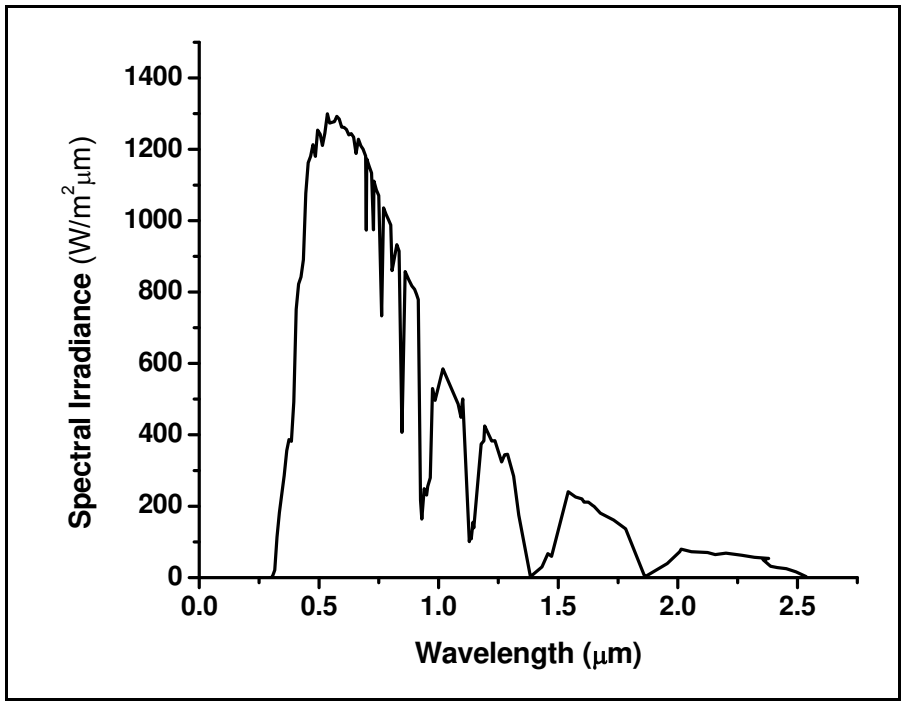

Figure 2.5: Standard AM1.5 Solar Spectrum [27]

2.2.2. Ideal Solar Cell

An ideal solar cell under illuminated conditions can be described as a diode and a current source connected in parallel (Figure 2.6). Diode represents the p-n junction of the solar cell and the current source represents the photo generated current. Under dark conditions a solar cell behaves like a diode. It follows the diode equation [26]:

$$I = I_0\left(e^{qV/k_BT} - 1\right) \tag{2.6}$$

where, I_0 : Diode Saturation Current

q : Electron Charge

V : Voltage at the terminal ends

T : Absolute Temperature

k_B : Boltzmann constant

The corresponding current-voltage equation of an ideal solar cell under illumination [26]:

$$I = I_0\left(e^{qV/k_BT} - 1\right) - I_L \tag{2.7}$$

where, I_L : Photogenerated Current

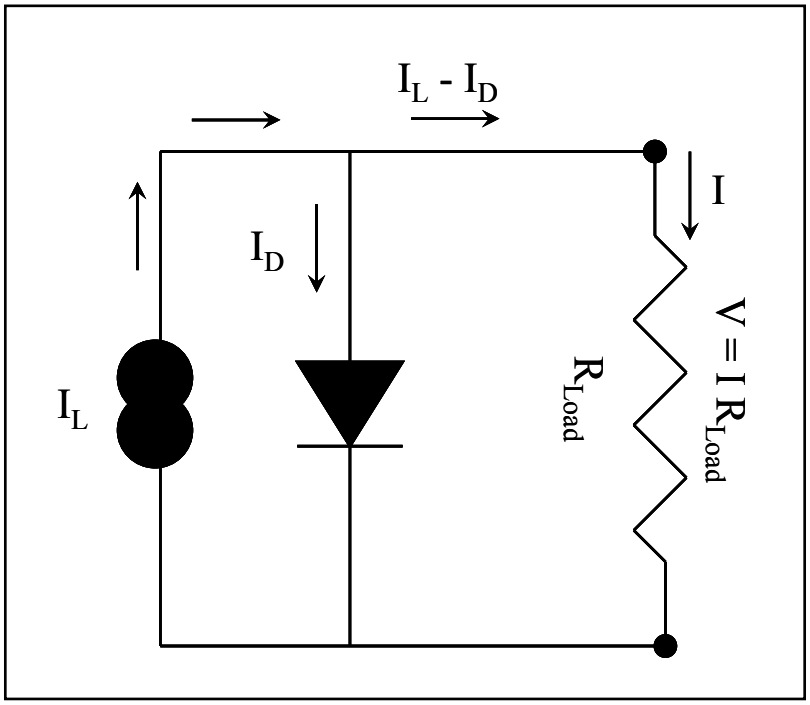

Figure 2.6: Equivalent circuit of an ideal solar cell under illumination

Under illumination the total current through the external circuit is the combination of the photogenerated current and the diode current. Under the short circuit condition the voltage, V = 0. Hence from equation 2.7, the short circuit current (I_{sc}) is equal to the photogenerated current (I_L).

$$I_{SC} = I_L \tag{2.8}$$

Open circuit voltage (V_{oc}) is obtained by setting the total current to zero in Equation 2.7 [26]

$$V_{OC} = \frac{kT}{q} \ln\left[\frac{I_L}{I_0} + 1\right] \approx \frac{kT}{q} \ln\left[\frac{I_L}{I_0}\right] \tag{2.9}$$

The ideal current-voltage characteristics of a solar cell under dark and illuminated conditions are shown in Figure 2.7

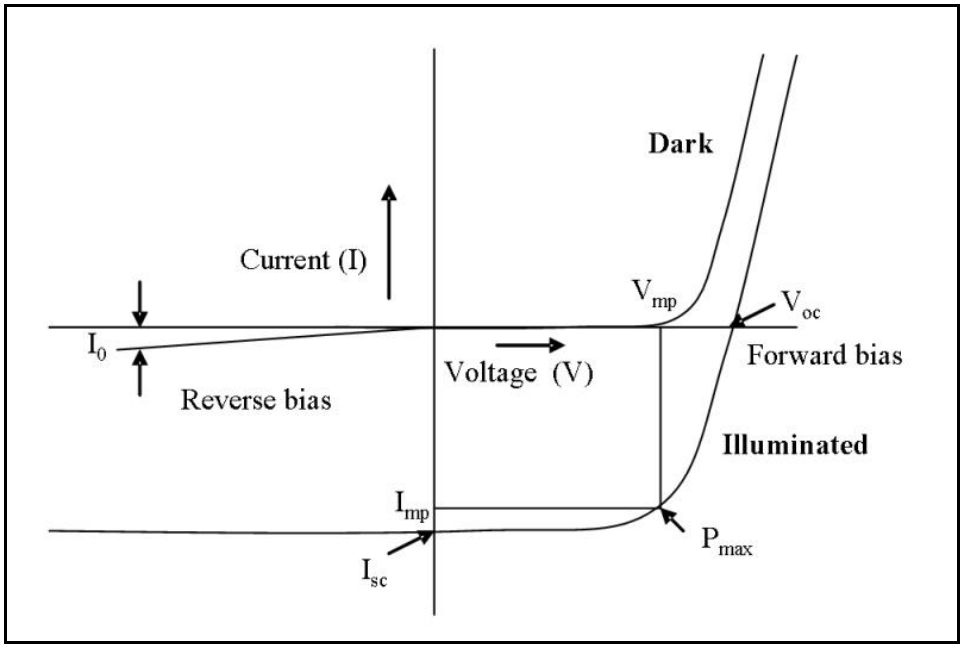

Figure 2.7: Current Voltage Curve of Solar Cell under Light and Dark Conditions

2.2.3. Solar Cell Equivalent Circuit

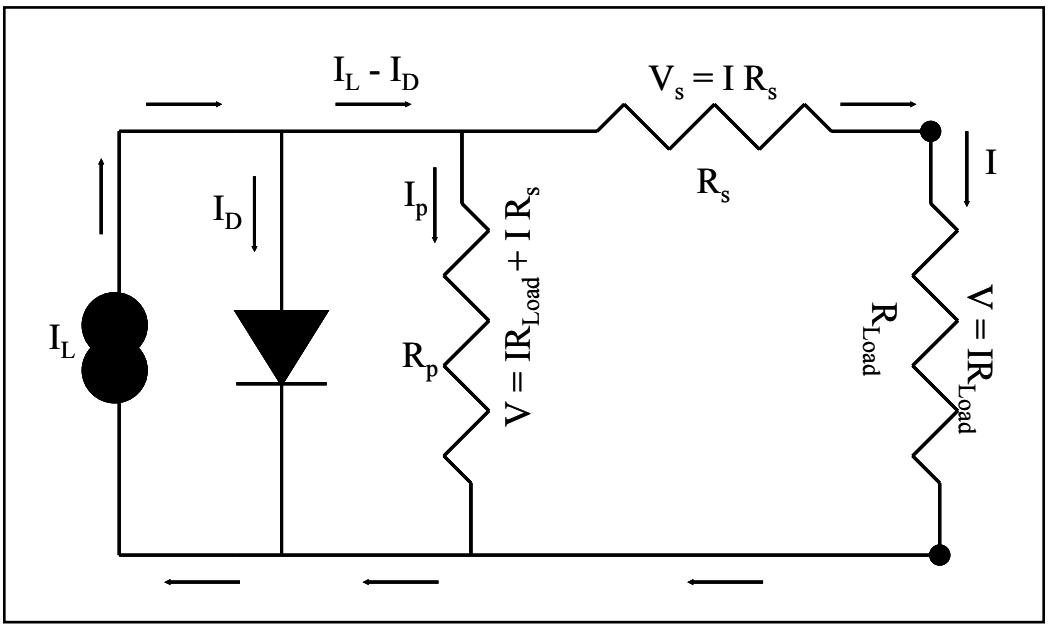

Figure 2.8: Equivalent circuit of a practical solar cell under illumination

The equivalent circuit of a practical or real solar cell is shown in Figure 2.8. The part of the circuit to the left of the two points is the cell and remaining is the load, characterized by the load resistor (R_{Load}). A real solar cell has a series resistance (R_s) and a shunt resistance (R_{sh}). Ideally the values of $R_s = 0$ and $R_{sh} = \infty$. The value of R_s and R_{sh} depend upon the properties of the solar cell. R_s of a cell can arise from the following causes: (*i*) bulk resistance of the individual layers, (*ii*) interface resistance between layers such as between absorber and back contact, and between front contact window layer and the contact fingers (*iii*) finger contact resistance. R_{sh} is due to the recombination in the absorber material and is inversely proportional to the number and impedence of shunt paths. The effect of R_s on short circuit current and R_{sh} on the open circuit voltage is shown in and Figure 2.10 respectively.

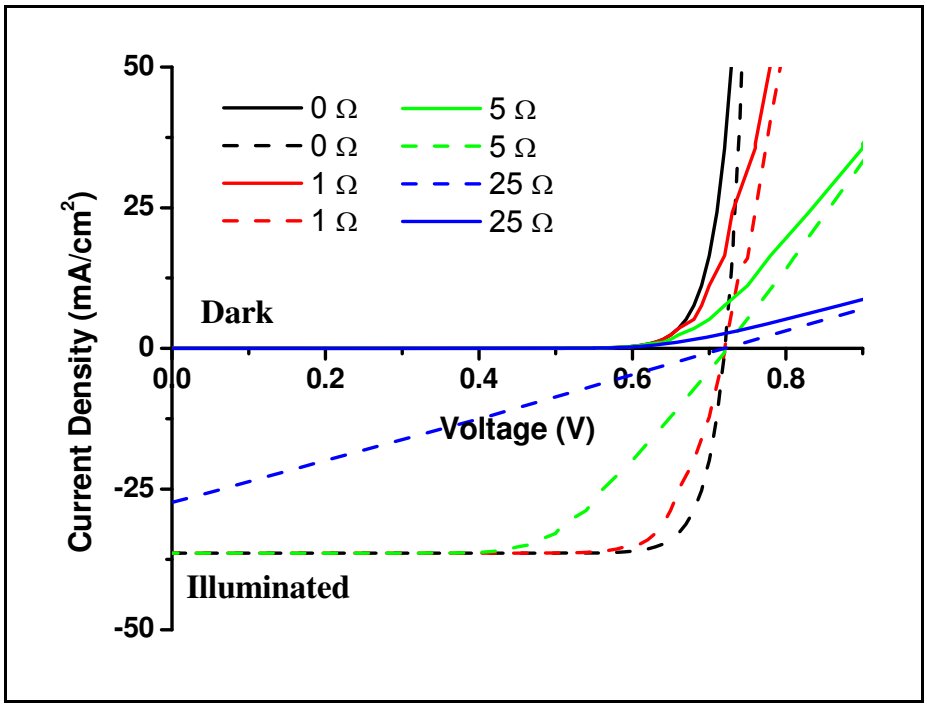

Figure 2.9: Variation of short circuit current density J_{sc} with series resistance R_s

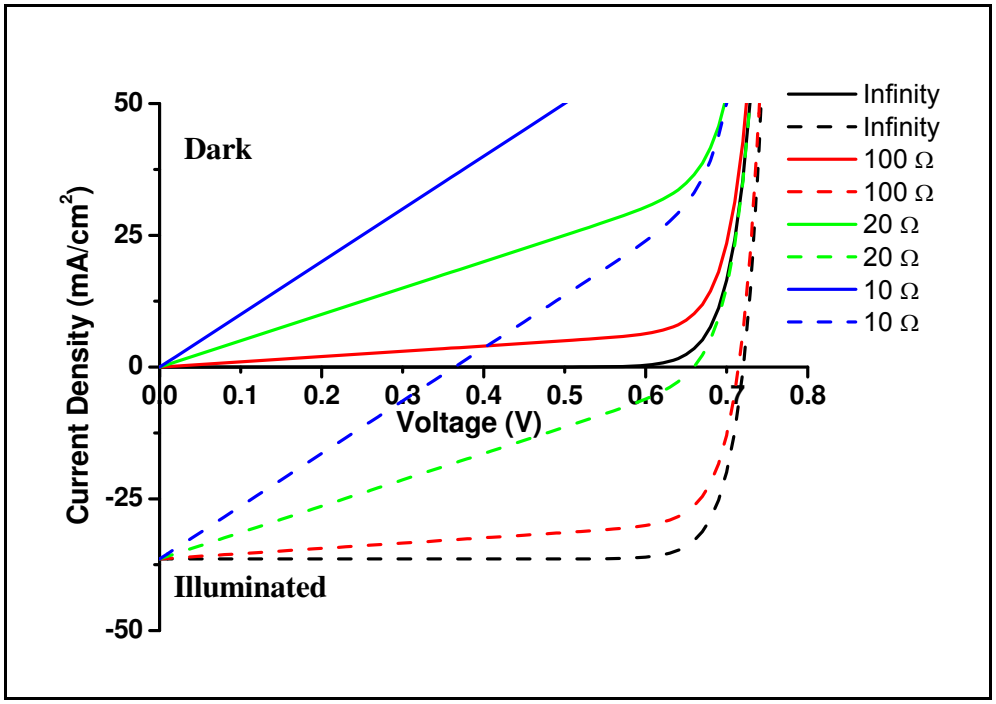

Figure 2.10: Variation of open circuit voltage V_{oc} with shunt resistance R_{sh}

Equation 2.7 does not include the effects of R_s and R_{sh}. The modified I-V equation is given by [26],

$$\ln\left[\left(I+\frac{I_L}{I_0}\right)-\frac{V-I.R_s}{I_0.R_{sh}}+1\right]=\frac{q(V-I.R_s)}{kT} \tag{2.10}$$

The power generated at V_{oc} and I_{sc} is zero. The cell generates maximum power (P_{max}) at a voltage (V_{mp}) and at current (I_{mp}). Fill factor is the measure of squareness of the I-V curve. Fill factor is defined as:

$$FF=\frac{V_m.I_m}{V_{oc}.I_{sc}}=\frac{P_{\max}}{V_{oc}.I_{sc}} \tag{2.11}$$

The conversion efficiency (η) of a solar cell is the ratio of the maximum power output (P_{max}) that can be extracted from the device to the incoming power (P_{in}):

$$\eta=\frac{P_{\max}}{P_{in}}=\frac{FF.V_{oc}.I_{sc}}{P_{in}} \tag{2.12}$$

For laboratory measurements, P_{in} = 100 W/cm^2, corresponds to the AM1.5 solar spectrum.

3. I-III-VI_2 THIN FILM SOLAR CELLS

3.1. Materials Properties

3.1.1.Band Gap Energies

One advantage of the I-III-VI_2 based thin film solar cells is that the various elements can be alloyed to form a new compound. The amount of each element in the compound can be controlled so as to achieve desired materials properties. The copper chalcopyrite system contains a wide range of bandgap energies. Figure 3.1 summarizes the lattice constants and the bandgaps of I-III-VI_2 based ternary alloys. The bandgap values range from 1.02 eV for $CuInSe_2$ (CIS) up to 2.70 eV for $CuAlS_2$, thus covering most of the visible spectrum. All the alloys have direct bandgap, thus making them suitable for thin films solar cell application.

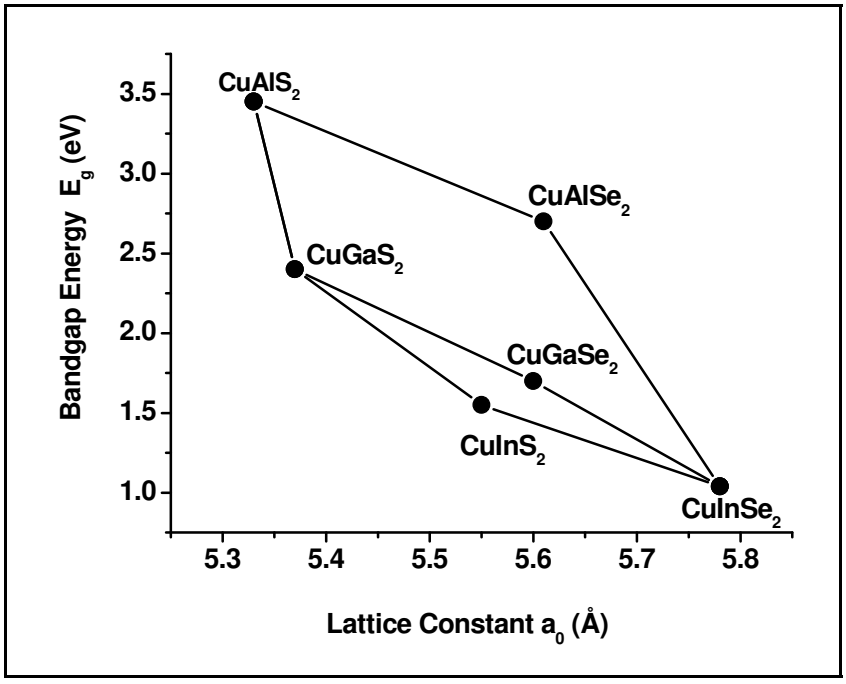

Figure 3.1: Lattice Constant Variations vs Bandgap of Copper Chalcopyrite Materials

3.1.2. Crystal Structure

$CuInSe_2$ (CIS) and its alloys have tetragonal chalcopyrite crystal structure (Figure 3.2 (b)). The tetragonal chalcopyrite structure of $CuInSe_2$ results from the cubic blend structure of ZnS (Figure 3.2 (a)). The Cu and In/Ga occupy the Zn sites alternatively. Each Cu and In/Ga have four bonds with the Se atom. In turn the Se atom has two bonds with Cu and two with In/Ga atoms. The bond strengths of the Cu-Se and In-Se or Ga-Se are in general different. Hence the ratio of the lattice constants (*c/a*) is not exactly 2. The deviation from *c/a* =2 is called as the tetragonal distortion. The value of *c/a* can vary from 2.01 for $CuInSe_2$ to 1.96 for $CuGaSe_2$.

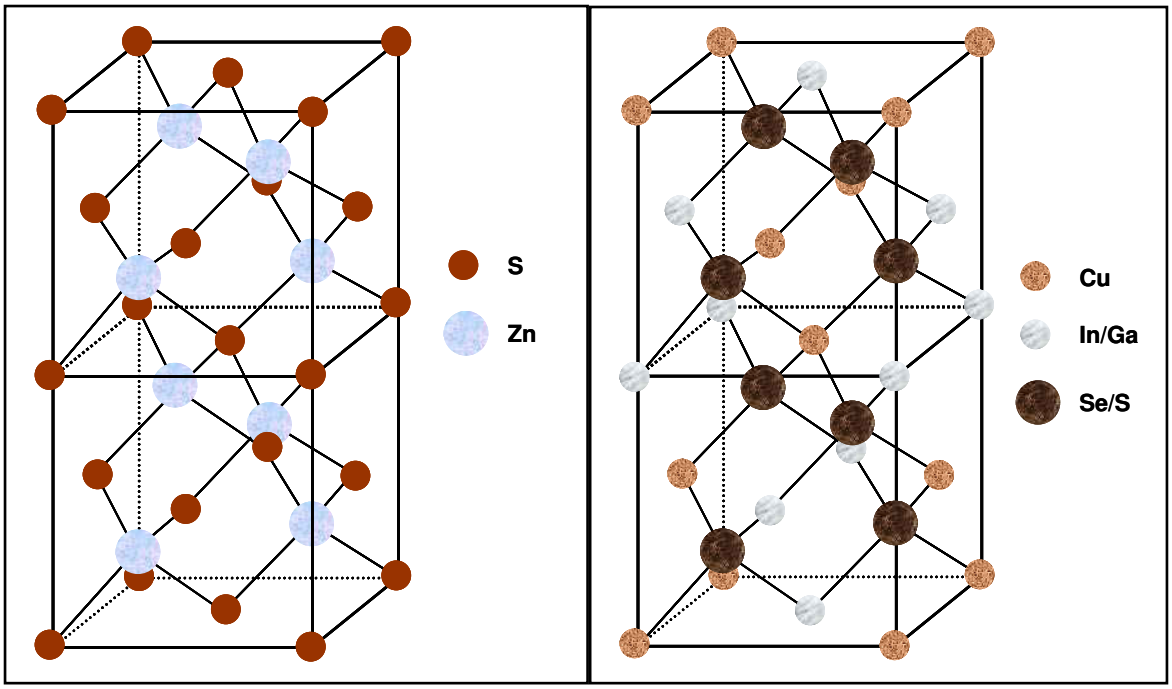

(a) (b)

Figure 3.2: Unit Cell of Chalcogenide Compounds. (a) Zinc Blende Structure of ZnS (2 Units) (b) Chalcopyrite Structure of $CuInSe_2$ Alloy [28]

3.1.3. Phase Diagram

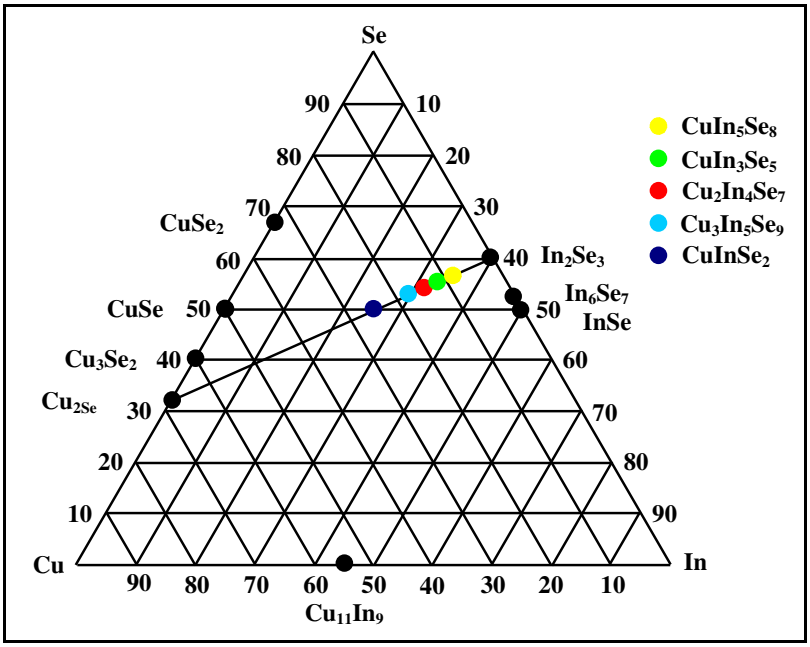

Figure 3.3: Ternary Phase Diagram of the Cu-In-Se Alloy [28]

$CuInSe_2$ alloy system has one of the most complex phase diagrams when compared with all the other thin-film solar cell materials. All the possible phases in the $CuInSe_2$ alloy system are indicated in the ternary phase at 500 ºC (Figure 3.3). $CuInSe_2$ absorber prepared under excess selenium has composition that fall on or close to the tie line between Cu_2Se and In_2Se_3. Along with the chalcopyrite $CuInSe_2$, the ordered defect compounds (ODC) viz, $Cu_3In_5Se_9$, $Cu_2In_4Se_7$, $CuIn_3Se_5$ and $CuIn_5Se_8$ also lie on the tie line. The ODC compounds have same chalcopyrite structure as $CuInSe_2$ [28]. The complex ternary diagram can be reduced to a simpler pseudo binary phase diagram (Figure 3.4) along the tie line. In the pseudo binary phase diagram, α = $CuInSe_2$, β = $CuIn_3Se_5$, γ = $CuIn_5Se_8$, and δ = high temperature phase with sphalerite structure. As seen from pseudo binary phase diagram, the α phase exists at copper concentration between 24–24.5 atomic (at.) % at room temperature. The existence of α phase is over a very narrow

composition range and does not even include the stoichiometric composition of 25 at.% Cu. Typically the copper content in the thin film absorber is 22-24 at%.

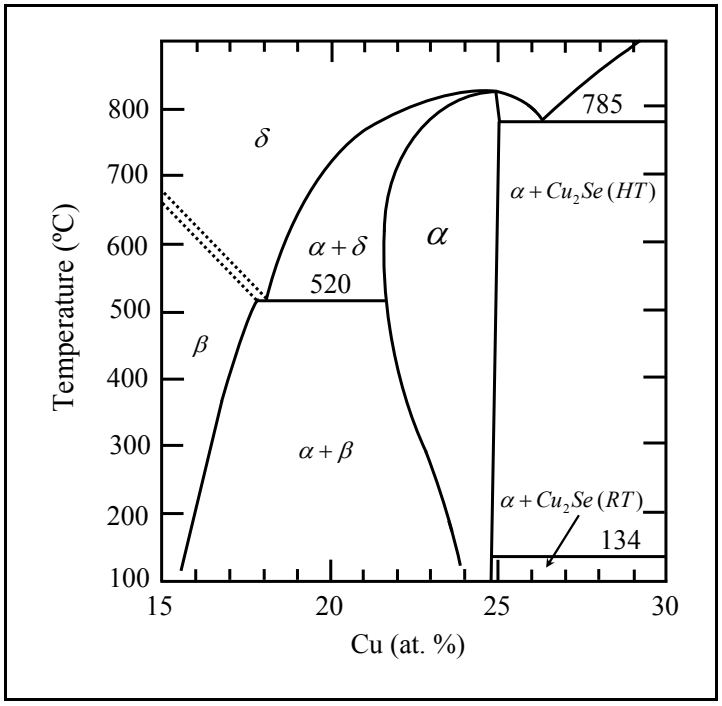

Figure 3.4: Pseudobinary In_2Se_3–Cu_2Se equilibrium phase diagram for compositions around the $CuInSe_2$ chalcopyrite phase [29].

The α or $CuInSe_2$ phase exists between 22 -24.5 at.% Cu at the growth temperature of 500 – 550 ºC. At room temperature, both $CuInSe_2$ and $CuIn_3Se_5$ phases exist at 22-24.5 at.% Cu. The β or $CuIn_3Se_5$ phase evolves due to the creation of copper vacancies (V_{Cu}) and indium on copper sites (In_{Cu}). Therefore, the phases are also termed ordered vacancy compounds. The β phase has a bandgap of 1.23 [30] -1.3 [31] eV. Higher bandgap at the junction will help increasing the open circuit voltage, V_{oc} [32]. However, some groups have reported that the β phase is weakly *n*-type [31]. The surface layer is weakly *n*-type and the bulk of the material is *p*-type, thus they form a buried *p*-*n* junction [33 - 34]. The inverted surface helps in reducing the recombination at the

interface. The thickness of the ODC layer depends upon the copper content in the film. ODC layer thickness varies inversely with copper content in the absorber [34].

Partial replacement of indium by gallium and by addition of sodium actively or passively widens the α phase thus making it possible to have single phase (α phase) region between 22-24.5 at.% Cu at room temperature [35]. It is evident from the phase diagram that the $CuInSe_2$ phase exists over a range of copper poor compositions at growth temperature of ~500 °C. If the absorber is prepared in a copper rich regime, Cu_2Se phase forms. The Cu_2Se phase is highly conductive. The presence of this phase diminishes the performance of the solar cell.

3.2. Light Absorption

High absorption coefficient is one of the properties that make $CuIn_{1-x}Ga_xSe_2$ (CIGSe) material well suited for solar cells applications. CIGSe thin film solar cells have direct bandgap whereas the crystalline silicon solar cells have indirect bandgap. Hence CIGSe absorbers would require very small (considerably or approximately 100 times lower) amount of material as compared to the crystalline silicon for the same extent of light absorption. The absorption of light by a semiconductor is given by the following optical transmission equation:

$$I_{(\lambda,x)} = I_{(\lambda,0)} e^{-\alpha\lambda x} \quad \text{.....3.1}$$

The intensity of light absorbed falls exponentially with depth x. The absorption coefficient of CIGSe absorber material is > 10^5/cm for a photon energy of $hv = E_g + 0.2\ eV$, where E_g is the bandgap of the material. The highest reported absorption coefficient is

$3.6x10^5$/cm for $CuInSe_2$ [36]. Figure 3.5 shows the optical absorption coefficient spectral dependence for various absorbers used in photovoltaic applications.

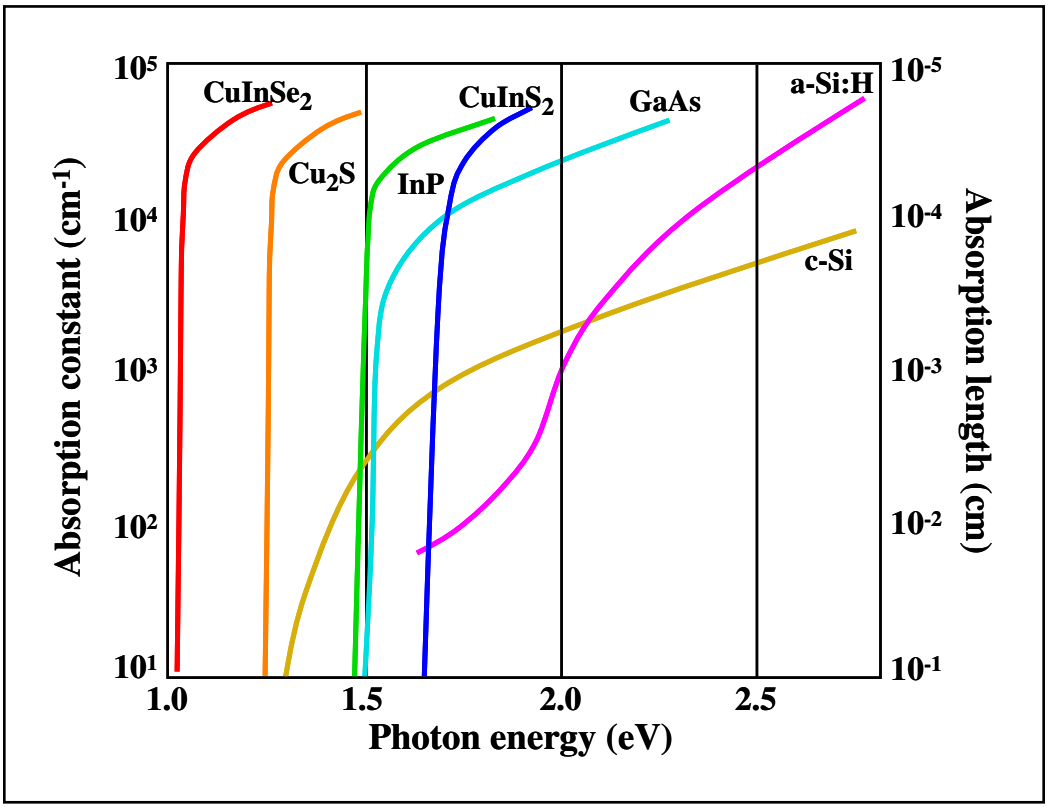

Figure 3.5: Dependence of the absorption coefficient on photon energy

3.3. Radiation Hardness

$CuInSe_2$ family of chalcopyrite compounds are known to possess high radiation hardness. The property of radiation resistance been suggested to be due to the self-repair of the radiation-induced damages rather than due to the resistance of the material to damage. The self-healing mechanism is due to the mobility of copper and also the reactions involving copper related defects (V_{Cu} and In_{Cu}) and defect complexes ($2V_{Cu}+In_{Cu}$). Thus, the electrical stability of the CIGSe thin films seems to be dynamic rather than static. The material is flexible to changes because of the inherent self-healing mechanisms.

3.4. Absorber Preparation

The I-III-VI_2 thin film solar cells have been fabricated using various techniques. The first thin film $CuInSe_2$ (CISe) solar cell was produced by the evaporation of CISe as a compound [37]. The most challenging issues in the mass production of these thin film solar cells are cost, high deposition rates with high material yield, compositional uniformity and also reproducibility. The various techniques used for the fabrication are selenization of the metallic layers [38 - 41], co-evaporation from elemental sources [42 - 45], evaporation from compound sources/flash evaporation, sputtering [46], electrodeposition [47 - 48], screen printing [49], close-spaced vapor transport [50], reactive sputtering [51], chemical bath deposition [52], laser ablation [53], spray pyrolysis [54 - 56] liquid phase epitaxy [57 - 58] and closed space sublimation [59]. Although various techniques have been used for the fabrication of $CuInSe_2$ solar cells, only the annealing of the sputtered metallic precursors in selenium precursor ambient and co-evaporation have resulted in highly efficient thin-film solar cells. Sputter/selenization (Showa Shell Sekiyu), co-evaporation (Würth Solar GmbH & Co.), sputter/sulfurization (Sulfurcell Solartechnik GmbH), sputter/RTP (Avancis), nanoink print/RTP (Nanosolar, Inc.) and sputter (Miasolé, DayStar Technologies, Inc.) techniques have been employed in the industry for high volume production.

3.4.1. Sputtering/Selenization (Two Stage Process)

Difficulties are always associated with scaling up of any deposition technology. Even though the highest efficiency on small area cell is by three stage co-evaporation of CIGSe from elemental sources [18], only Würth Solar GmbH & Co. which does use co-evaporation and Honda Soltec Co., Ltd. are the companies to scale up the technology for high volume production.

Compositional uniformity over large area, low deposition temperature and high throughput are the factors that make sputtering as the technique most suitable for large scale production.

The technique of sputtering of precursors for the $CuInSe_2$ absorber layer was pioneered by ARCO Solar. Later Shell Solar developed the process further. The two stage process was developed by ARCO Solar [60]. The two stage process consists of the deposition of the Cu-In metallic precursors on Mo coated substrate by sputtering. The metallic precursors are later annealed in diluted H_2Se ambient. H_2Se breaks down to produce selenium which reacts with the metallic precursors to form $CuInSe_2$. However, H_2Se gas is very toxic and hazardous with the time weighted average threshold limit value (TWA-TLV) of 0.05 ppm. H_2Se is usually stored in high pressure cylinders (~20 kgf/cm^2). Metalorganic selenides, such as diethyl selenide (DESe), dimethyl selenide (DMSe) and ditertialbutylselenide are being used as alternative candidates for the Se source for metal organic chemical vapor deposition (MOCVD) of ZnSe and other chalcogenides [61]. The metalorganic selenides are liquids at room temperature and are stored at atmospheric pressure in glass or stainless steel bubblers. Hence it involves less danger of wide spread leakage as compared to H_2Se. Even though the TWA-TLV of DESe or DMSe is 0.2 mg/m^3, they are regarded as safer alternatives to H_2Se in potential leakage risk. Chichibu *et al.* first demonstrated the possibility of using DESe as selenium source for the preparation of I-III-VI_2 based absorber [61]. Earlier, $CuIn_{1-x}Ga_xSe_{2-y}S_{2y}$ (CIGSeS) thin film solar cell with an efficiency of 13.73% has been fabricated at the FSEC PV Materials Laboratory using DESe as selenium source [62].

3.5. Bandgap Grading

3.5.1. Addition of Gallium

The optimum bandgap for maximum solar cell output is ~1.5 eV. However, the bandgap of $CuInSe_2$ is 1.02 eV that is well below the optimum match to the solar spectrum. The bandgap of $CuInSe_2$ can be increased by addition of gallium [63]. The increase in the bandgap due to the addition of gallium is governed by the following equation:

$$E_{g(x)} = E_{g(0)} + (E_{g(1)} - E_{g(0)})x + bx(x-1) \text{ [64]} \quad \text{.....3.2}$$

where, $E_{g(0)}$: Band gap of $CuInSe_2$ (1.02 eV)

$E_{g(1)}$: Band gap of $CuGaSe_2$ (1.68 eV)

b : Bowing parameter (0.15 – 0.24 eV for $CuInGaSe_2$)

x : Gallium concentration

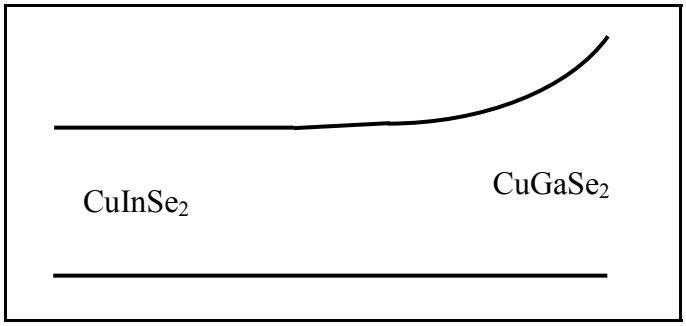

Figure 3.6: Band bending due to gallium back diffusion

In a two-stage process the Cu-Ga-In metallic precursors are deposited either by sputtering or evaporation. The next step involves the annealing of the metallic precursors in the selenium ambient, known as the selenization process. During the selenization process gallium diffuses to the back Mo interface and indium diffuses to the surface. This leads to the formation of $CuGaSe_2$

phase at the CIGSe/Mo interface and $CuInSe_2$ phase at the surface. The formation of $CuInSe_2$ at the surface and $CuGaSe_2$ at the interface is due to the difference in the reaction rates of the two phases. Selenization of Cu-In precursors require less time and temperature to form $CuInSe_2$ phase as compared to the formation of $CuGaSe_2$ phase from Cu-Ga precursor [65]. The overall reaction time for the formation of $CuInSe_2$ is $1/6^{th}$ times the formation of $CuGaSe_2$ [66]. In the CIGSe crystal structure copper occupies one of the two cation sites and the gallium or indium occupies the remaining one. Due to the higher reaction rate indium atoms move to the surface and form $CuInSe_2$. There are very few sites available at the surface for gallium. Hence the gallium atoms move to the back to form $CuGaSe_2$. $CuGaSe_2$ is a wider 1.68 eV bandgap semiconductor. Thus the $CuGaSe_2$ formation at the back helps to raise the conduction band minima near the Mo/CIGSe interface [67]. This creates a back surface field that helps in reflecting the electrons to the junction and increases the open circuit voltage [68].

The formation energy for a Ga_{Cu} defect is higher than that of In_{Cu}. This destabilizes the formation of defect complexes, the two copper vacancies in combination with indium on copper antisite ($2V_{Cu}+In_{Cu}$) thereby reducing the tendency for the formation of ODC [69] and thus enhances the α-phase ($CuInSe_2$).

3.5.2. Sulfurization Process

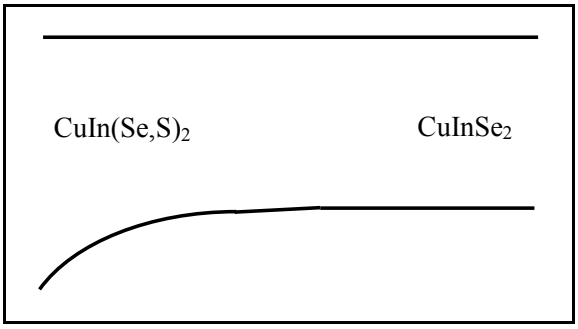

Figure 3.7: Band bending due to sulfur at the junction

As described above the addition of Ga to $CuInSe_2$ thin films to increase the bandgap and hence the open circuit voltage is not achieved for films prepared by two-stage process.

$CuInGaS_2$ (CIGS2) is a wide bandgap semiconductor with a bandgap of 1.55 eV. The bandgap of CIGS2 is higher than that of $CuInGaSe_2$ ($CIGSe_2$). Sulfurization of $CIGSe_2$ absorber layer is a bandgap engineering technique. Bandgap grading can be achieved by the addition of sulfur to $CIGSe_2$. However, the grading depends on the time, temperature and also the sulfur content. The increase in the bandgap due to the addition of sulfur is governed by the following equation:

$$E_g = 0.95 + 0.8x - 0.17x(1-x) + 0.7y - 0.05y(1-y)\ [70] \quad \text{.....3.3}$$

Sulfurization of $CuInGaSe_2$ leads to the formation of CIGSeS or CISeS at the surface. This helps in increasing the bandgap of the absorber at the interface by shifting the valence band maxima to lower energies. In the two-stage process the favorable grains grow large at the cost of the unfavorable grains. Large numbers of small grains are present at the molybdenum/CIGSe interface. If the sulfurization process is carried out for a longer duration, sulfur due to its higher diffusivity will diffuse to the back and form CIGSeS or CGSeS, leading to the lowering of the valence band. At high temperature, higher amount of sulfur can react with molybdenum to form thicker MoS_2 layer consequently leading to higher resistivity that increases the series resistance of the cell and thus reduces the fill factor. Hence it is necessary to optimize the sulfurization process to minimize the diffusion of sulfur to the back.

During the sulfurization process, sulfur may replace selenium or occupy the already existing selenium vacancies (V_{Se}). This helps in reducing the compensating donors and also passivates the surface [71].

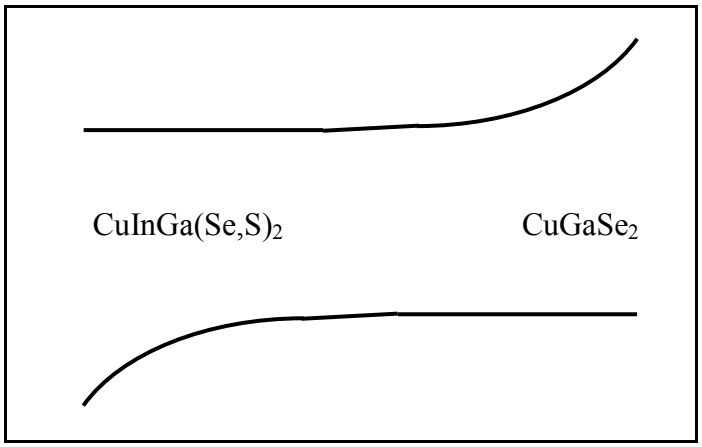

Figure 3.8: Band gap gradient due to gallium and sulfur

3.6. Incorporation of Sodium

In early research, CIGSe absorbers prepared on sodalime glass were found to give highly efficient solar cells as compared with the cells on borosilicate glass. This was attributed to the effects of sodium on the electrical and structural properties. This phenomenon was discovered in the year 1993 [72]. Sodium can be incorporated into CIGSe absorber layers during various stages of film growth using various sodium compounds. Sodium diffuses from the sodalime glass (SLG) substrate into CIGSe film during growth. Sodium can also be supplied in the from a thin sodium containing precursor layer deposited prior to CIGSe absorber growth.

The “standard” method to incorporate Na into CIGSe absorber layers is to use a sodalime glass substrate without an alkali barrier layer between the substrate and the Mo back contact layer, where the Na diffuses into the absorber during growth. World-record efficiency cells have been fabricated by using this technique. The typical sodium concentrations found in such CIGSe layers are of the order of 0.1 at% [73]. Sodium diffusion from the SLG is a passive sodium incorporation technique that depends on the properties of the SLG and also the properties of the

Mo back contact. The diffusion of sodium by the passive incorporation technique is non-uniform and also is not well-controlled.

The non-uniform out diffusion of sodium from the SLG substrate can be avoided by using an alkali barrier. The typical diffusion barriers employed are Si_3N_4 [74], SiO_2, Al_2O_3 [75] etc. Na containing precursor film is usually deposited prior to the precursor deposition on the Mo back contact layer. Na containing compounds used are NaF [75], Na_2Se [76], Na_2S [77] or Na_xO [78].

Sodium has also been incorporated into the film after the precursor deposition but before the selenization/sulfurization process. However, this method of sodium incorporation adds another step in the process and may not be suitable for large volume production.

3.6.1. Effects of Na Incorporation

Usually, sodium is detrimental to semiconductor devices. However, the presence of Na during growth of the CIGSe absorber layer is beneficial for the device performance. Actual mechanisms that aid in improving the overall efficiency of the device are not yet understood. There are various hypotheses that have been formulated by various groups. Some of them have been discussed in the following: Even though there is a general agreement on the beneficial effects of sodium, there is no unanimity on the some of the details of the effect of sodium on the CIGSe absorber. It has been observed that the presence of sodium during the absorber growth smoothens the surface [75, 79]. Another group has observed an increase in grain size [79 - 80], however, there is also evidence of decrease in grain size in literature pertaining to effect of sodium on CIGSe absorber [81]. Sodium incorporation increases the carrier concentration thus leading to the increase in the *p*-type conductivity [82-86]. The increase in the *p*-type

conductivity is attributed to suppression of indium on copper antisite (In_{Cu}) donor type defects which act as majority carrier traps [87]. Sodium also reduces the compensating donors by filling selenium vacancies (V_{Se}), thus increasing the *p*-type conductivity. Air annealing of CIGSe absorber has improved the solar cell performance [88]. Sodium also enhances the influence of O_2 on the $CuInSe_2$ thin film absorber. Oxygen passivates the selenium vacancies (V_{Se}) present at the grain boundaries and surface of the Cu-chalcopyrite thin films [87, 89, 90]. This enhances the *p*-type conductivity.

Increase in crystallinity and (112) orientation have also been reported in the films prepared in the presence of sodium [79, 82, 83]. $NaInSe_2$ forms during absorber preparation, this directs the $CuInSe_2$ film to the (112) preferred orientation [87]. Sodium ions diffuse to the surface of the absorber along the grain boundaries and subsequently react with selenium to form sodium polyselenide (Na_2Se_x) compound where x = 1-6, $\neq$ 5. Na_2Se_x compounds act as a selenium source during the absorber growth. Na_2Se_x compounds retard the growth of the CIGSe phase and thus aid in improved incorporation of selenium into the absorber film. If the partial pressure of the selenium is low then Na_2Se, a very stable compound is formed. The release of selenium from Na_2Se is unlikely thus leading to poor absorber growth [91].

The isolated point defects, copper vacancy (V_{Cu}), are shallow acceptors that contribute to their very efficient ability of doping of $CuInSe_2$ p-type. The most thermodynamically favorable defect complex which prevents the degenerate doping in In-rich material is ($2V_{Cu} + In_{Cu}$). Isolated In_{Cu} would be a deep donor, but the ($2V_{Cu} + In_{Cu}$) defect complex is electrically neutral. The existence of the ordered vacancy compounds may be explained as periodically repeating ($2V_{Cu}+ In_{Cu}$) units. Sodium has a tendency to reduce detrimental point defects. It tends to occupy the possible copper sites in the lattice thus reducing the formation of ($2V_{Cu}+ In_{Cu}$) defect pair

thereby reducing the formation of ordered defect compounds (ODC) and thus, increases the α($CuInSe_2$) phase [35]. Sodium incorporation into Cu-poor film results in higher charge carrier mobility. Sodium also influences the formation of the beneficial $MoSe_2$ layer between Mo and CIGSe [92]. The overall effect of Na incorporation during the growth of the film is an increase in the efficiency by enhancement of fill factor and open circuit voltage.

Overdose of sodium eliminates the copper vacancies (V_{Cu}) thus reduces the carrier concentration [87]. Thin in turn has significant effect on the electronic properties. Excessive amounts of sodium can also result in structural defects.

3.7. Formation of Interfacial Layer at Mo/Absorber Interface.

A thin interfacial layer is formed at the molybdenum and absorber interface during absorber preparation. The interfacial layer can be $MoSe_2$ and $Mo(S_xSe_{1-x})_2$ depending on the process. Both the compounds have hexagonal lattice structure. The lattice constants of $MoSe_2$ are a_0 = 3.288 Å and c_0 = 12.92 Å. The $MoSe_2$ layer is formed at temperatures >350 ºC [93]. The material is stable at 67 at.% selenium between 0 ºC – 1200 ºC and. The heat of formation of $MoSe_2$ is -242.2± 3.3 kJ/mol at 298.15 °K and p = 101.325 kPa [94]. The bandgap of $MoSe_2$ is 1.3 – 1.4 eV and is inherently highly p-type in nature.

The formation of this layer depends on several parameters. Studies have shown that the formation of the interfacial layer affects the performance of the solar cell. The Mo/CIGSe contact, without the $MoSe_2$ layer formation, results in a schottky type of contact that causes recombination losses at the back contact. Formation of a thin $MoSe_2$ layer is essential to facilitate a quasi-ohmic electrical contact across the CIGSe–Mo interface. This quasi-ohmic contact results in reduced recombination losses and thus improves cell efficiency [95]. The $MoSe_2$ layer also improves the adhesion of the absorber layer to the molybdenum back contact [96].

The thickness and crystallographic orientation of the $MoSe_2$ layer determine the adhesion and electrical properties of the CIGSe–Mo interface. The conductivity of $MoSe_2$ layers is anisotropic hence the orientation of the layers can have a direct effect on the transport properties at the interface. Conductivity through the parallel $MoSe_2$ layer is about two times higher than the $MoSe_2$ layers oriented perpendicular to the molybdenum substrate [97].

3.8. Junction and Device Formation

3.8.1. Buffer Layer Deposition

Cadmium sulfide (CdS) is a direct bandgap *n*-type semiconductor with a bandgap of ~2.42 eV. The lattice mismatch between the CdS and CIGSe is very small. In the early stages of the development of CIGSe thin film solar cell the junction was formed by depositing CdS layer of thickness approximately 1-3 μm by sputtering [100] or evaporation [101]. The temperature of the substrate during the evaporation process was maintained between room temperature and ~200 ºC. Bilayer of CdS, consisting of a thicker low resistivity layer doped with In [102] or Ga [80] and a thinner high resistivity layer were deposited by evaporation or chemical bath deposition (CBD).

Thin CdS layer deposited by CBD is to date the preferred heterojunction partner layer for $CuInGaSe_2$ thin films solar cells. The desired thickness of CdS layer is ~50 nm. Due to a bandgap of 2.4 eV CdS layer absorbs light and decreases the short circuit current especially in the case of thicker CdS layers. Usually, the thickness of the CdS layer grown by CBD is very thin and hence this reduces the absorption of light. If the CdS layer is too thin or does not exist, recombination in the space charge region of the absorber layer increases. This result in the reduction of open circuit voltage, fill factor and spectral response. In chemical bath deposition,

the growth of CdS layer occurs either by the reaction between the constituent ions or by clustering of colloidal particles [103]. CdS layer protects the junction against mechanical and chemical damages due to the subsequent deposition of ZnO layer.

The advantages of CdS layer by CBD are described in the following:

1. CdS layer deposited by CBD provides complete coverage of the uneven absorber layer surface as compared to deposition by evaporation at very low thickness.
2. The Cd^{+} may also diffuse into the Cu poor surface layer of the absorber layer and occupy the Cu sites. This helps in reducing the acceptor defect density and thus causing a consequent type inversion. This type inversion might result in a buried homojunction. The diffusion of Cd^{+} into the CIGSe layers also depends on the orientation of the CIGSe layer. (220/204) oriented CIGSe layers allow more Cd^{+} diffusion into the CIGSe layer.
3. During the CBD process ammonia removes the native oxides. The absorber surface is thus cleaned which enables the epitaxial growth of CdS layer.
4. Sodium present at the CIGSe/CdS interface may affect the junction properties. CdS deposition by CBD may wash away the traces of sodium present on the absorber surface.

The disadvantages of CdS layer are described in the following:

1. CdS deposition by CBD is a wet process. In an in-line module fabrication plant CBD does not comply with vacuum deposition steps.

2. CBD process produce large amount of hazardous waste and also the material yield is very low.
3. The bandgap of CdS restricts the photons from the blue region to reach the absorber.

Due to the above mentioned disadvantages researchers are investigating different options to replace CdS as the heterojunction partner. However, it is difficult to find a replacement with similar properties due to the beneficial chemistry of the CBD process and favorable properties of CBD CdS layer as a heterojunction partner.

The deposition of CdS by CBD is carried out using the following three constituents:

1. Cadmium precursor: $CdSO_4$ [104], $CdCl_2$ [105], CdI_2 [106], or $Cd(CH_3COO)_2$ [75]
2. Sulfur precursor : Thiourea ($SC(NH_2)_2$)
3. Complexing agent : NH_4OH

The complexing agent, NH_4OH slows down the reaction and also avoids the formation of $Cd(OH)_2$ [106]. The concentration of thiourea is higher than that of the metal precursor. The CdS deposition is carried out at 60 – 90 ºC where thiourea hydrolyzes and decomposes to release S^{2-} ions. The CdS formation reaction proceeds as follows:

$$Cd(NH3)_4^{2+} + SC(NH_2)_2 + 2OH^- \rightarrow CdS + H_2NCN + 4NH_3 + 2H_2O$$

3.8.2. Transparent Contacts

The early generation $CuInGaSe_2$ based thin film solar cell used CdS doped with In [102] or Ga [80] as front contact layers in addition to the CdS buffer layer. The bandgap of these layer

was ~2.42 eV. The entire short wavelength light (<520 nm) was absorbed by the thick CdS layer resulting in reduction of the total photocurrent generated. Deposition of CdS layer by CBD allowed the layer to be very thin. This reduced the absorption of short wavelength light. This also enabled to use front contact layer with higher bandgap so as to transport the photocurrent efficiently.

The front contact layer in the CIGSe based thin film solar cell is very important. The front contact materials should meet following two main criteria:

1. High (>85%) transparency so as to let most of the light pass through.
2. Low Resistivity ($<10^{-3}$ Ω-cm) so as to be able to transport all the photogenerated current to the front contact without significant resistive losses.

Three materials could satisfy the above criteria: ZnO, ITO and SnO_2. The deposition of SnO_2 is carried out at 350-750 °C. After the deposition of CdS layer CIGSe devices cannot withstand temperatures > 200 to 250 °C. ZnO and ITO were the remaining choices. The cost of ZnO is much lower compared to ITO. Hence ZnO is being used as the front contact layer.

The present day devices use oxide bilayers consisting

(i) ~50 nm thick highly resistive layer and

(ii) 200 – 500 nm thick highly conductive layer.

Together with CdS, the highly resistive undoped ZnO (*i*:ZnO) layer protects the device from electrical losses due to the inhomogenities present in the absorber. Moreover, the *i*:ZnO layer prevents the diffusion of aluminum from the highly conductive ZnO:Al layer into absorber layers. *i*:ZnO layer also protects the interface layer from sputter damage induced during the

deposition of the ZnO:Al layer which typically requires harsh conditions. The thickness of the *i*:ZnO layer is also critical from the device performance point of view. If the thickness of the *i*:ZnO below the optimum thickness then it may lead to the increase in the leakage currents. If the layer is too thick it will decrease the current density due to an increase in the series resistance. i:ZnO layer greatly influences the open circuit voltage, V_{oc} [107].

Doped zinc oxide films have several attractive properties such as high conductivity, high (3.3 eV) bandgap making it highly transparent in the visible region and has high reflectance for infrared radiation. The low electrical resistivity of the transparent conductive oxide films is due to intrinsic defects, i.e. oxygen vacancies (V_O) and zinc interstitials (Zn_i) which act as shallow n-type donors [108-109]. Low resistivity films can be achieved by introducing charge carriers into ZnO by extrinsic doping with group III elements such as aluminum [110], boron [110] or gallium [111]. Aluminum belongs to group III elements and Zinc belongs to the group II elements. When ZnO is doped with Al, Al atoms replace Zn atoms and act as donors. The amount of aluminum doping in ZnO can vary from 0.1 wt. % – 2 wt. % [112]. The properties of the highly conductive layers vary with the amount of doping and also the process gases.

Various techniques have used to deposit the doped ZnO layer, viz., DC and RF magnetron sputtering [113], reactive DC sputtering [114], chemical vapor deposition [115], atomic layer epitaxy [116] MOCVD [117], laser ablation [118], and sol-gel techniques [119]. However, higher deposition rates (up to 12 μm/min), very good thickness uniformity and high density of the films, relatively cheap deposition method and scalability to large areas makes RF magnetron sputtering technique as the preferred process for the deposition of the ZnO:Al front contact.

4. EXPERIMENTAL TECHNIQUE

The experimental techniques used in the preparation of complete or partial CIGSe or complete CIGSeS thin films solar cells for this thesis are described in the following sections. Materials characterization and cell analyses techniques used are also described briefly at the end of the chapter.

4.1. Device Fabrication

4.1.1. Substrate and Substrate Cleaning

Low cost sodalime glass (1-3 mm thick) was used as the substrate for this research. The sodalime glass substrate was cleaned using the following steps: 1% LiquiNox® soap solution was prepared in deionized water. The substrates were immersed in the soap solution when the temperature of the soap solution was ~90 ºC and was continuously stirred for 3 hours. The substrate was rinsed thoroughly with running water and also in a tank containing deionized water. Finally the substrates were dried using a N_2 gas jet.

4.1.2. Deposition of Alkali Barrier Layer

A thin alkali barrier layer was deposited on the sodalime glass prior to the deposition of the molybdenum back contact so as to minimize the diffusion of sodium from the sodalime glass during the absorber preparation. Various alkali barrier layers have been used such as silicon nitride, silicon dioxide, aluminum oxide. However, the performance of silicon nitride as an alkali barrier was better when compared to the other barriers [74]. Hence silicon nitride was used as the alkali barrier layer for this research. Silicon nitride was deposited on sodalime glass by reactive

radio frequency (RF) magnetron sputtering process using a pure silicon target. Pure silicon target was used because it is cheaper (about one third in cost) and considerably robust as compared to the expensive and brittle silicon nitride ceramic targets. The partial pressure of argon and nitrogen gas mixtures, RF sputtering power and substrate movement duration per unit distance were systematically varied to obtain the desired film thickness of an optimized silicon nitride layer.

The cleaned substrates were mounted in the vacuum chamber and were maintained overnight in high vacuum. A combination of mechanical, turbo molecular pump and cryopump was used to establish a base pressure of ~$2x10^{-6}$ torr. The base pressure was measured using Bayard Alpert type ionization gauge. Ultrahigh purity argon and nitrogen gas were introduced into the chamber. The pressures of the gases were controlled using mass flow controllers and measured using convectron gauges. The chamber gate valve was throttled to maintain the total pressure at $1.6x10^{-3}$ Torr of Ar:N_2::$8x10^{-4}$:$8x10^{-4}$ during the deposition. Depositions were carried out from a silicon target of dimensions 30 cm x 10 cm. The substrates were moved linearly along 10 cm width of the target with the help of a LabVIEW© controlled stepper motor. The sputtering process was performed under various power and substrate movement duration per unit distance to deposit films with a nominal thickness of ~750 – 1000 Å.

4.1.3.Molybdenum Back Contact Deposition

Molybdenum is one of the most suitable materials used as back contact for $CuInSe_2$ (CISe), $CuIn_{1-x}Ga_xSe_2$ (CIGSe), $CuIn_{1-x}Ga_xSe_{2-y}S_y$ (CIGSeS) and $CuInGaS_2$ (CIGS2), thin-film solar cells. Several metals such as Pt, Au, Al, Ni, Ag, Cu, W, Mo, Cr, Ta, Nb, V, Ti, Mn have been investigated as back-contact material for CISe based thin-film solar cells. Pt, Au, Ni, and

Mo all form fairly reproducible, low-resistance contacts to the CISe absorber layer. Au and Pt show significant diffusion into the CISe layer when annealed at elevated temperatures [120]. Mo and Ni contacts seem to improve with high-temperature treatment [121]. Ti, V, Cr and Mn were found to react with selenium during the CIGSe absorber growth. Ta and Nb demonstrated improved performance with the graded bandgap absorbers. Mo and W demonstrated comparable device performance [122]. Moreover, for polycrystalline CISe based thin-film solar cells, the metallic back contact forms the substrate upon which the absorber layer is formed. Molybdenum is the most widely used back contact material in I-III-VI_2 solar cells because of its relative stability at the processing temperatures, resistance to alloying with Cu and In, and its low contact resistance to the absorber layer [123].

The properties of molybdenum films depend strongly on the target–substrate distance and the argon pressure during deposition. The sputtering gas pressure determines the properties, viz. adhesion and resistivity of the back contact layer. Molybdenum layer deposited at lower pressures have a smooth surface and this results in very low resistivity. Films deposited at lower pressures often suffer from adhesion problem due to compressive stresses. However, molybdenum layer deposited at higher pressures show higher resistivity and better adhesion. The molybdenum layer deposited at high pressures has poor resistivity due to the rough surface. Hence, this results in the growth of rougher absorber layers. However, they adhere to the glass much better.

Molybdenum back contact was deposited by DC magnetron sputtering in a vacuum chamber with base pressure of ~2 x 10^{-6} Torr using a combination of a mechanical, turbo and a cryopump (1500 liters/sec). Depositions were carried out from a molybdenum target of dimensions 30 cm x 10 cm. The substrates were moved linearly along 10 cm width of the target

with the help of a LabVIEW© controlled stepper motor. The thickness variation was in the range of ± 3% along the 30 cm length of the target [124]. A total of four layers, viz., two compressive and two tensile were deposited. The first and the third layer were deposited with high argon pressure so as to achieve tensile films. The second and the fourth layer were deposited with low argon pressure and high power. These layers were compressive in nature. The total thickness of the resulting molybdenum back contact layer was ~0.9 μm.

4.1.4. Sodium Precursor Deposition

As mentioned earlier (Section 3.6) various compounds can be used as sodium precursors. Among the available sodium precursors, NaF is stable in air, non-hygroscopic and evaporates stoichiometrically. Hence in this research, NaF was used as the sodium precursor. After the deposition of molybdenum back contact the substrates were allowed to cool down for ~2 hours in the sputtering chamber. The substrates were immediately moved to the evaporation chamber for the NaF deposition. A combination of mechanical and diffusion pump was used to maintain high vacuum. The advantages of diffusion pump are low maintenance cost, low running cost, high pumping speed and reliability. The major disadvantage of diffusion pumps is the tendency to backstream oil vapors into the vacuum chamber. A liquid nitrogen trap was used to minimize backstreaming of the oil vapors. The NaF layer was deposited by the thermal evaporation process. The thickness of the NaF layer was varied from 40 Å to 120 Å. The distance between the substrate and the boat was ~7 inches. The power was adjusted to maintain the rate of deposition at ~1 Å per second. The total thickness and the deposition rate was measured with "*Inficon XTC/2*" thin-film deposition controller. After the deposition, the gate valve to the diffusion pump was closed and the substrate was allowed to cool for ~2 hours.

4.1.5. Deposition of Metallic Precursors

Two-stage process was used for the preparation of the absorber layer. The first step consisted of the deposition of the CuGa-In metallic precursors. The molybdenum coated substrates and/or the substrates coated with silicon nitride/molybdenum/NaF were mounted in the sputtering chamber and kept overnight in high vacuum. The metallic precursors were deposited by DC magnetron sputtering. The melting point of gallium is 29.76 ºC. Therefore, it is difficult to prepare a pure gallium target and subsequently to sputter from it. Hence an alloy target of Cu-Ga (78 at.% Cu and 22 at.% Ga) was used. The indium precursor was deposited from 99.999% indium target. The layers were deposited in a stacking sequence. The precursor deposition was started with CuGa as the first layer and ended with either CuGa or a very thin indium layer. The substrates were moved linearly along the width of the targets and the duration for which the substrate was stationary at every incremental step was optimized to achieve the desired thickness. The size of the targets was similar as mentioned before. The deposition of CuGa was carried out at a sputtering power of 350 W and argon pressure of 1.5 mTorr and the indium was deposited at sputtering power of 230 W and argon pressure of 0.7 mTorr. The deposition parameters were optimized so as to obtain a copper-poor absorber.

4.1.6. Absorber Preparation

A large conventional furnace with a capability of selenization/sulfurization of one hundred 4” by 4” pieces was utilized for the absorber preparation. The furnace uses a gold mirror for insulation. The gold mirror insulations assists in fast heat up and cool down times. The mirror helps to maintain a uniform temperature throughout the length of the furnace. A quartz tube is coaxially placed inside the gold coated tube. The quartz tube is used to keep the mirror clean

from any deposits. The heating element, a coil like structure fits in between the quartz tube and the gold mirror furnace. Each end of the gold mirror furnace is held in place by ceramic ends that are mounted on the base. A metal flange is used to seal the open end of the quartz tube during the process.

The entire elemental stack was homogenized and the required amount of an organometallic selenium precursor was introduced in the furnace. The selenization process was carried out in pure H_2 ambient or in the forming gas of N_2 and H_2 ambient. The selenization process was carried out in the temperature range of 450 ºC – 550 ºC for 30-60 minutes. After the selenization process all the process gases were exhausted and filled with H_2S to carry out the sulfurization process. The sulfurization process was carried out in N_2 ambient at 515 ºC – 550 ºC with 5-12 minutes dwell period. The process gases were evacuated and the chamber was filled with N_2 for cool down.

4.1.7. Heterojunction Partner Deposition by Chemical Bath Deposition

Chemical bath deposition (CBD) was used in this research for the deposition of the cadmium sulfide (CdS) heterojunction partner layer. The CdS layer deposition was carried out in an alkaline aqueous solution with pH >9. The main ingredients used in the CBD process were: ammonium hydroxide (NH_4OH), cadmium sulfate ($CdSO_4$) and thiourea ($SC(NH_2)_2$).

The aqueous solution of all the ingredients with required amounts were prepared separately. The absorber sample was taken out of the furnace and transferred into the dilute KCN solution to etch $Cu_2(Se,S)$ phase, if any. All the samples were cleaned thoroughly in two beakers of deionized water so as to remove the traces of KCN solution. Finally the samples were cleaned with a deionized water jet. The thiourea solution was filtered so as to remove any particulates

that may act as nucleation sites. Deionized water, along with solutions of NH_4OH, $CdSO_4$, and $SC(NH_2)_2$ were mixed and the sample was immediately transferred into the solution prepared for the deposition. The samples were placed with the film surface facing the wall of the beaker so as avoid the turbulence. The temperature of the water bath was maintained at 65 ºC. The beaker was placed in the water bath and stirring was initiated with a magnetic stirrer. After 10-12 mins both the outer bath and the CdS solution attained ~60 ºC. The samples were taken out of CdS solution when the color of the samples was bluish purple. The samples were cleaned with deionized water so as to remove any particulates from the surface. Later the samples were thoroughly dried using a nitrogen gas jet.

4.1.8. Transparent Conducting Oxide (TCO) Layer Deposition

i:ZnO and ZnO:Al TCO bilayers were deposited using RF magnetron sputtering. The 99.995% purity ZnO:Al target contained 2 wt% Al_2O_3. Special care was taken to always maintain the deposition chamber in vacuum so as avoid the contamination of the sputter targets. After the deposition of the CdS layer the samples were mounted into the vacuum chamber for TCO deposition. For every deposition, a clean glass sample was also mounted along with the samples to serve as the test sample for transparency and sheet resistance measurements. The optical transmission spectroscopy of the bilayer ZnO film was measured using "*Shimadzu UV-2401PC*" spectrophotometer.

A combination of mechanical pump, turbo molecular pump and cryopump (800 liters/sec) was used to establish a base pressure of ~$2x10^{-6}$ torr. The samples were maintained overnight in the vacuum chamber. This process also aids in degassing the chamber walls and thus to reduce the water vapor content from the chamber. The targets were presputtered for ~15 minutes so as to

remove any undesired contaminants from their surface. A thin layer of ~50 nm *i*:Zno was deposited with the following parameters: RF power of 200 W and Ar pressure of 1.5 mTorr. ZnO:Al layer of ~500 nm was deposited at RF power of 425 W and argon pressure of 1.5 mTorr. ZnO:Al film with a sheet resistance of 30-60 Ω/□ and transparency of ~90% was routinely deposited using this process. After the deposition, the samples were allowed to cool for 1-2 hours before they were removed from the chamber for front contact finger deposition.

4.1.9. Contact Grid Lines

The chromium/silver front contact fingers were deposited through the metal mask using vacuum evaporation technique. The thicknesses of the contact fingers were previously optimized. First, ~500 Å thick chromium was deposited followed by the deposition of ~1.25 μm thick silver. The average deposition rate for chromium was ~2 Å per second. The power was adjusted so as to maintain the rate of deposition for silver at ~20 – 25 Å per second. The total thickness and the rate of deposition were measured by "*Inficon XTC/2*" thin-film deposition monitor and controller. Chromium was deposited first because it provides good adhesion to ZnO and it also prevents the diffusion of silver in to the ZnO:Al layer. The metal masks have been designed such that 9 cells could be deposited on a 1"x2" area substrate. The area of each cell was ~0.45 cm^2. Figure 4.1 shows the design of the front contact fingers with dimensions based on the NREL design. The current produced by the solar cell is directly proportional to the cell area exposed to light i.e. the active area. Hence it is necessary to design the grid with minimum shadowing. Another criterion for the design of the contact grid is the ability to collect electrons efficiently. The 2-D image shows that the two criterions have been considered in the design of the front contact fingers. The grid lines provide the effective collection of elections and the small

dot, designated ***P*** in the Figure 4.1 provides the point contact where the micro manipulator probe is placed during the I-V characteristics measurements. Figure 4.2 shows the complete cross section of the CIGSeS thin film solar cells.

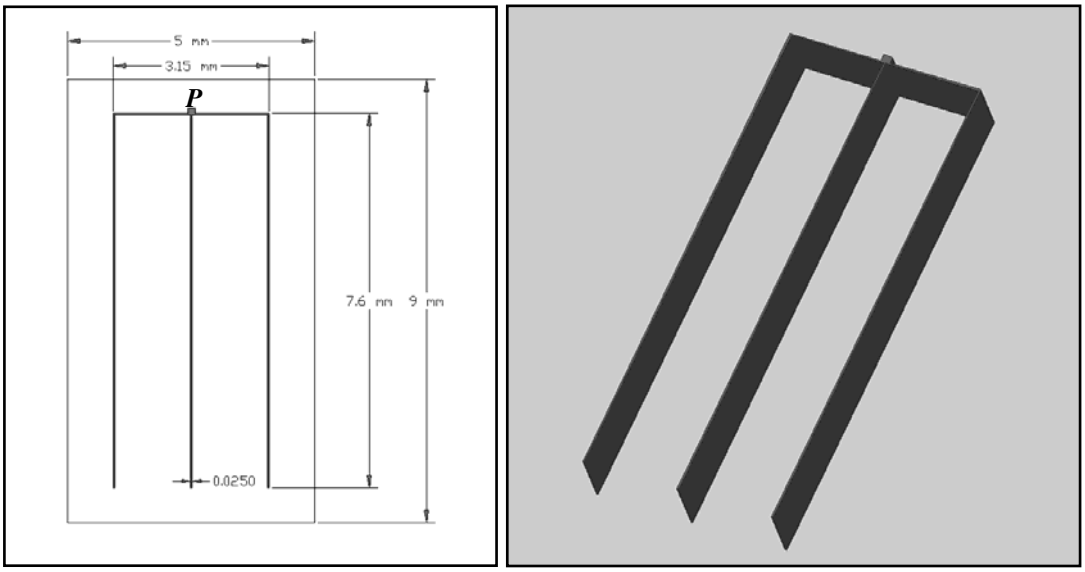

Figure 4.1: 2-D and 3-D image of the front contact fingers (All dimensions mentioned are an approximate values)

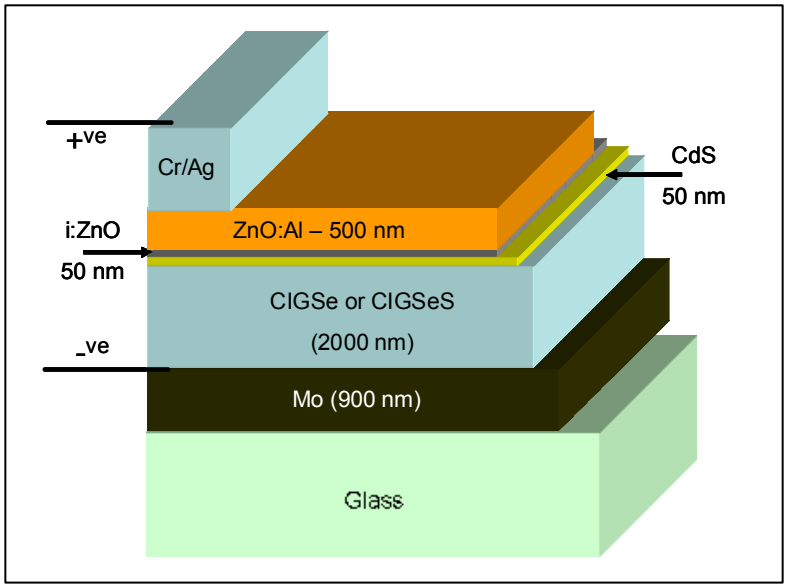

Figure 4.2: CIGSeS Thin Film Solar Cell Structure

4.2. Characterization

4.2.1. Material Characterization

Various characterizations techniques were used to study the materials properties and cell characteristics. The sheet resistance of the absorber layer was measured for approximate assessment of conductivity. Thicknesses of the films were measured with a ***Dektak3*** profilometer. Optical microscopy was carried out at the FSEC PV Materials Lab and scanning electron microscopy (SEM) was carried out to at Materials Characterization Facility (MCF) of the UCF Advanced Materials Processing and Analysis Center (AMPAC) to study the surface morphology of the films. SEM was also used to study the cross sectional grain growth. ***JEOL 6400F*** was used for SEM analyses. Chemical composition of the bulk of the film was analyzed by electron probe micro analysis (EPMA) and energy dispersive X-ray spectroscopy (EDS). The EPMA data provided in this research is an average of data points from 10 locations. ***JEOL 6400F*** was used for EDS analyses at MCF and EPMA analyses was carried out at the National Renewable Energy Laboratory (NREL). The X-ray diffraction (XRD) patterns were obtained in a ***Rigaku D/MAX*** XRD with 40 kV copper X-ray tube to analyze the crystallographic structures and phases. The lattice parameters, preferred orientation and the composition of the absorber films were derived using the XRD data.

Composition-depth profile of the film was analyzed by Auger electron spectroscopy (AES). ***Physical Electronics 600 AES/SAM*** was used for Auger electron spectroscopy at MCF. AES uses an electron beam to excite the sample, and then measures the energies of emitted Auger and other secondary electrons. An ion gun attached in the system allows obtaining elemental depth profiles from the thin-film absorber layer. The elemental counts were later converted to atomic percentage and were plotted versus depth.

Transmission electron microscopy (TEM) analysis was performed at MCF using a ***FEI Technai F30*** TEM operated at 300 keV. The specimen for TEM analysis was prepared by FEI 200 TEM focused ion beam instrument (FIB). The ***200 TEM FIB*** removes material by sputtering using gallium ions at lateral resolution of approximately 50 nm. The absorber films appear to be porous due to the damages occurring during sample preparation. However, this is an artifact and does not reflect the true nature of the films. EDS and electron energy loss spectroscopy (EELS) were employed in the transmission electron microscope to study the elemental distribution in the ***FEI Technai F30*** TEM.

Electron Backscattered Diffraction (EBSD) technique, recently introduced to analyze thin-film solar cells was used to index diffraction patterns for each pixel on the image, provide maps of the orientation of crystalline phases, misorientation between grains, texture, grain distribution, deformation, and strain. EBSD analysis was carried out at NREL.

4.2.2. PV Characterization

4.2.2.1. Current-Voltage Characteristics

The current-voltage (I-V) characteristics of all the completed cells were measured using an in-house designed and built I-V setup. I-V measurements were carried out both under illumination and in the dark. I-V measurement under illumination is carried out to obtain the relevant photovoltaic parameters: open circuit voltage, Voc, short circuit current density, J_{sc}, series resistance, R_s, shunt resistance, R_p, fill factor (FF) and efficiency, η. Dark I-V analysis was carried out to obtain values of the fundamental parameters of the solar cell such as: reverse saturation current density J_0 and diode factor, A. PV Cells with good characteristics were sent to NREL for authentication.

4.2.2.2. Quantum Efficiency Measurements

Quantum efficiency (QE) is ratio of the number of carriers generated by the solar cell to the number of photons of a given energy incident on the solar cell.

$$QE_{(\lambda)} = \frac{N_{CarriersGenerated}}{N_{IncidentPhotons}}$$

QE relates to the response of a solar cell to the various wavelengths in the spectrum. QE is given as a function of either wavelength or energy. The QE measurements were carried out at NREL.

5. RESULTS AND DISCUSSIONS

5.1. Effects of Sodium on the Absorber

The presence of sodium during the $CuInGaSe_2$ (CIGSe) absorber growth provides many beneficial effects such as grain growth, orientation, increase in p-type conductivity. However, contrasting result such as decrease in grain size have also been published (Section 3.6.1). It is not known whether different recipes or growth parameters may be contributing or be responsible for the inconsistencies in the results. CIGSe or $CuIn_{1-x}Ga_xSe_{2-y}S_y$ (CIGSeS) layers grown by 2 stage process were investigated in order to clarify the effects of sodium on their microstructural properties.

CIGSeS is a very complex compound. Initially, the effects of sodium were studied on CIGSe thin films deposited on molybdenum coated sodalime glass substrates. In this case, the sodalime glass substrates were without an alkali barrier. Alkali barrier minimizes the diffusion of sodium from the sodalime glass. The out-diffusion of sodium from the sodalime glass into the absorber during the growth also depends on the properties of molybdenum. The extent of sodium out diffusion is uneven and cannot be controlled during the growth. For this experiment all the substrates were chosen from a single 1'x1' piece of molybdenum coated sodalime glass. It was assumed that the extent of out-diffusion of sodium from the sodalime glass into the absorber was approximately the same for all the samples in this series. In order to compare the effects of sodium, various amounts of sodium fluoride, viz., 0, 40Å and 80 Å were deposited (Section 4.1.4) on the CuGa-In precursors as described in section 4.1.5. The following deposition parameters were maintained constant for all the samples in this series: CuGa - 350 Watt sputtering power at Ar pressure of 1.5 x 10^{-3} Torr and In - sputtering power 230 Watt at Ar

pressure of 7 x 10^{-4} Torr. The substrate movement duration per unit distance used for this experiment were based on the electron probe microscopy analysis (EPMA) data (Table 5.1) of earlier samples in which that the Cu/In+Ga ratio was found to be Cu/(In+Ga) = 0.859. The CIGSe absorber layers were prepared by selenization of the CuGa-In precursors. Organometallic compound, diethyl selenide (DESe) was used as the selenium precursor. The selenization was carried out at 475 ºC for 45 minutes.

Table: 5.1: EPMA (@20 kV) of CIGSe absorber samples

Cu	In	Ga	Se	Cu/In+Ga
23.85	24.07	3.68	48.38	0.859

A diffractometer with standard θ-2θ geometry was used for the X-ray diffraction analyses. The XRD patterns (Figure 5.1) reveal all the major chalcopyrite reflections. There was no evidence of the formation of binary phases. This suggests that a stable chalcopyrite structure was formed in all the cases. The intensities of all the CIGSe or CIGSeS reflections were determined by integrating the areas below the peaks. The ratio of the each intensity with respect to the total area of intensities of all the peaks was calculated. The integrated intensities of the XRD data of a randomly prepared (usually a powder) sample are usually considered to estimate the degree of preferred orientation. The JCPDS data is from a randomly prepared sample. Hence the JCPDS data was used for the comparison to calculate the degree of preferred orientation. The estimates of the degrees of preferred orientation for all the peaks are provided below. As can be seen the error in the calculations become large when the peaks such as 211 and 336 are very weak. Therefore, only the most intense peaks (112, 220/204 and 116/312) are considered in these estimates. The degrees of preferred orientation for the three peaks with highest intensity are

provided in Table 5.1. A slight increase in the degrees of preferred orientation is observed with an increase in the thickness of sodium fluoride for (112) peak. Consequently, there is a decrease in the degrees of preferred orientation for (220/204) and (312/116) peaks with an increase in the amount of sodium. Thus, indicating that sodium addition is having an influence on the degree of preferred orientation of CIGSe. Refer to APPENDIX A: Degree of Preferred Orientation Calculation for the detailed calculations of the degree of preferred orientation.

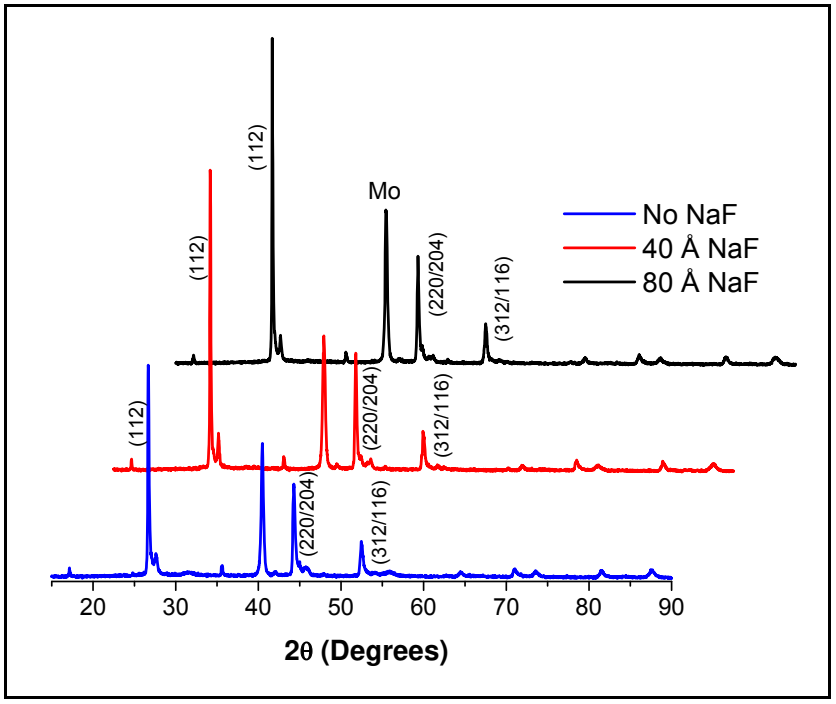

Figure 5.1: XRD spectra of CIGSe films with various NaF thicknesses.

Table 5.1: Degrees of preferred orientation for CIGSe thin film grown with different NaF thicknesses.

Orientation	No NaF	40 Å	80 Å
112	0.958	1.032	1.041
220/204	0.649	0.635	0.599
312/116	0.970	0.898	0.857

The lattice parameters (Table 5.2) were calculated for all the samples using the XRD data. Refer to APPENDIX B: Lattice Parameter Calculations for the detailed calculations of the lattice parameters. The lattice parameters were compared with the theoretical values. The lattice parameter (a_0) closely matches with $CuIn_{0.9}Ga_{0.1}Se_2$. The composition obtained from XRD is a rough estimate of the compound.

Table 5.2: Lattice Parameters and Composition of the CIGSe film.

NaF	Lattice Parameters	
	a_0	**c_0**
No	5.786	11.540
40 Å	5.787	11.565
80 Å	5.781	11.531

The positions of copper, indium and gallium are fixed in the lattice. However, when gallium is added it occupies/replaces the indium and similarly sulfur replaces or occupies selenium vacancies. The lattice constants for $CuInSe_2$ is $a_0 = 5.78$, $c_0 = 11.62$ and that of $CuGaSe_2$ is $a_0 = 5.614$ and $c_0 = 11.022$. The 2θ value for the 112 peak for $CuInSe_2$ and $CuGaSe_2$ are at 26.66º and 27.69º respectively. The 2θ value for the 112 peak shifts to 26.96º for $CuIn_{0.7}Ga_{0.3}Se_2$. In the samples prepared by the 2-stage process gallium diffuse to back and the XRD pattern does not reflect the fraction of gallium. Comparing the measured XRD data with the theoretical values a rough estimate of the composition can be found. EPMA can provide the exact composition of the film.

Figure 5.2: Optical images (@ 50x) for CIGSe samples with A) No NaF, B) 40 Å NaF and C) 80 Å NaF

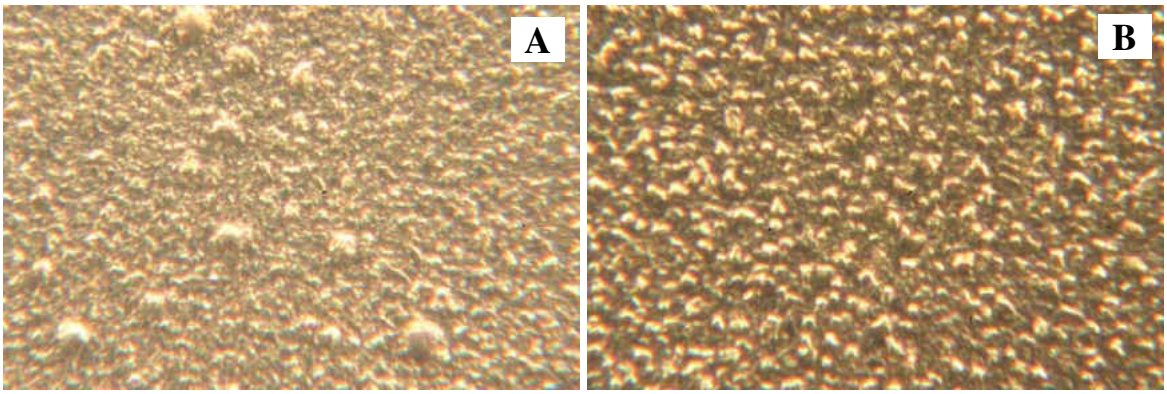

Figure 5.3: Optical image (@ 500x) for CIGSe sample with A) No NaF and B) 40 Å NaF

Figure 5.2 shows the optical microscopy images of the CIGSe samples with A) No NaF, B) 40 Å NaF and C) 80 Å NaF. The film with no NaF appears to be uniform. However, some rods or needle like features are observed. These features could not be removed by etching. The presence of these features affects the solar cell performance. Sometimes the films with No NaF also exhibited grains with the shape of a cauliflower (Figure 5.3A). The rod and needle like feature disappear in the films with 40 Å and 80 Å (Figure 5.2 B, C & Figure 5.3B) because the presence of sodium during the absorber growth enhances mobility of species present in the film

and thus eliminates such features. The film with 40 Å (Figure 5.2B) appears to be rougher as compared to the film with 80 Å NaF which is very smooth and uniform (Figure 5.2B C). Thus the addition of with 40 Å NaF begins to eliminate the features, however, the enhancement in the mobility of atoms is yet insufficient and addition of 80 Å NaF is essential to make the film featureless and smooth.

Figure 5.4, Figure 5.5 and Figure 5.6 show the scanning electron microscopy images of the CIGSe thin film surface with no NaF, 40 Å NaF and 80 Å NaF respectively. As can be seen from Figure 5.3 the sample with no NaF has disorderly grain growth resulting in smaller grains with corresponding higher grain boundary density as well as hillocks and craters. Sodium is known to have high mobility and to act as a flux that imparts the higher mobility to the adatoms on the sample. Higher mobility of atoms results in improved grain growth. This can be observed in Figure 5.4 for absorber film with 40 Å NaF where the grain growth is more orderly as compared to absorber film with no NaF. The sample with 40 Å NaF is more compact, smoother with fewer hillocks, almost no craters and uneven grain growth (Figure 5.5). For the sample with 80 Å NaF the grains are comparatively larger and well faceted and have grown in a compact manner. The surface also appears to be smoother (Figure 5.6). The absorber film with 80 Å NaF results in highly ordered grain growth as compared to the absorber film with 40 Å NaF. The mobility of the adatoms is directly proportional to the concentration of species with higher mobility. There is a progressive increase of grain size with the amount of sodium precursor. Grain boundaries are crystal imperfections and the most potential recombination centers. Absorbers with large grains are the most desired since they indicate good crystal quality.

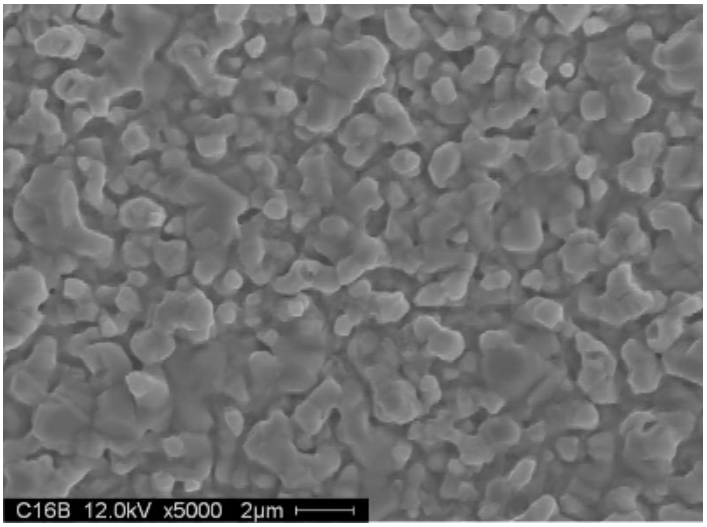

Figure 5.4: SEM image of CIGSe surface grown on sodalime glass substrate without NaF.

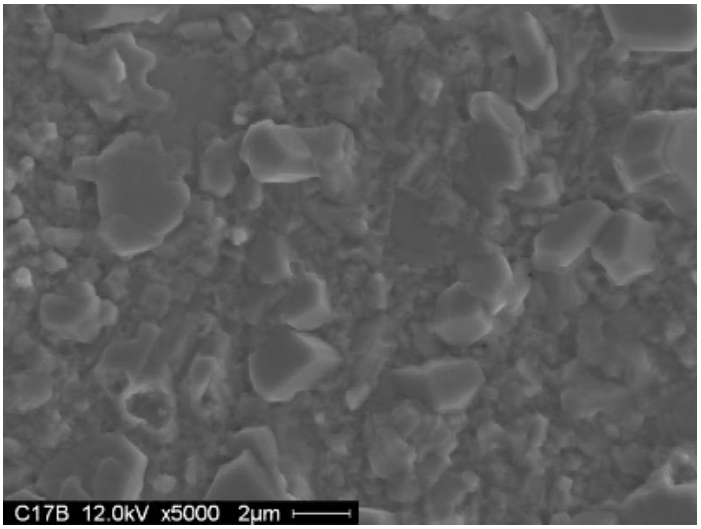

Figure 5.5: SEM image of CIGSe surface grown on sodalime glass substrate with 40 Å NaF.

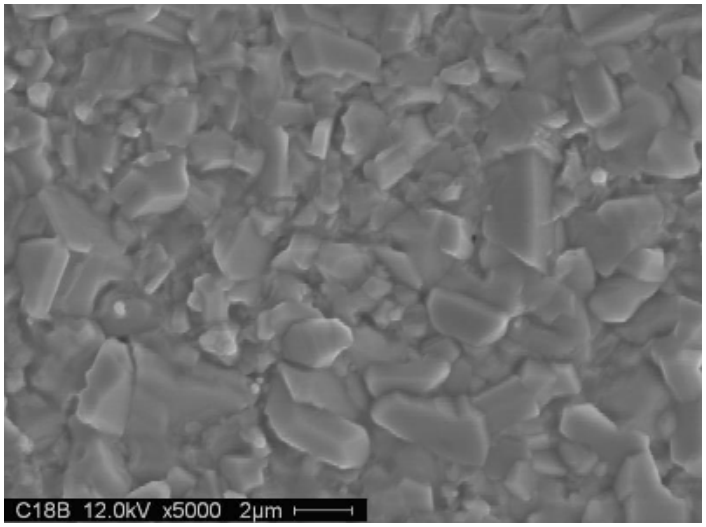

Figure 5.6: SEM image of CIGSe surface grown on sodalime glass/Mo substrate 80 Å NaF.

A progressive increase of grain size with increase in sodium precursor was observed in the above figures. Structural differences between the CIGSe layers grown with no or various thicknesses of sodium precursor was investigated by cross sectional SEM. Figure 5.7, Figure 5.8, and Figure 5.9 show the cross sectional SEM image of the CIGSe thin film with no NaF, 40 Å NaF and 80 Å NaF respectively. As seen from Figure 5.7 the grains show disorderly growth and hence a very rough surface for the sample with no sodium precursor. Samples with 40 Å NaF (Figure 5.8) and 80 Å NaF (Figure 5.9) reflect the impressions from the surface SEM images i.e., the grains are compact. The grains also appear to be comparatively large and columnar for sample with 40 Å NaF and 80 Å NaF. The sample with 80 Å NaF appears to be smoother when compared to the sample with 40 Å NaF. The grains appear to be porous at the Mo/CIGSe interface. The grains at the Mo/CIGSe interface material may have been displaced during the sample preparation. Hence, leading to a porous interface.

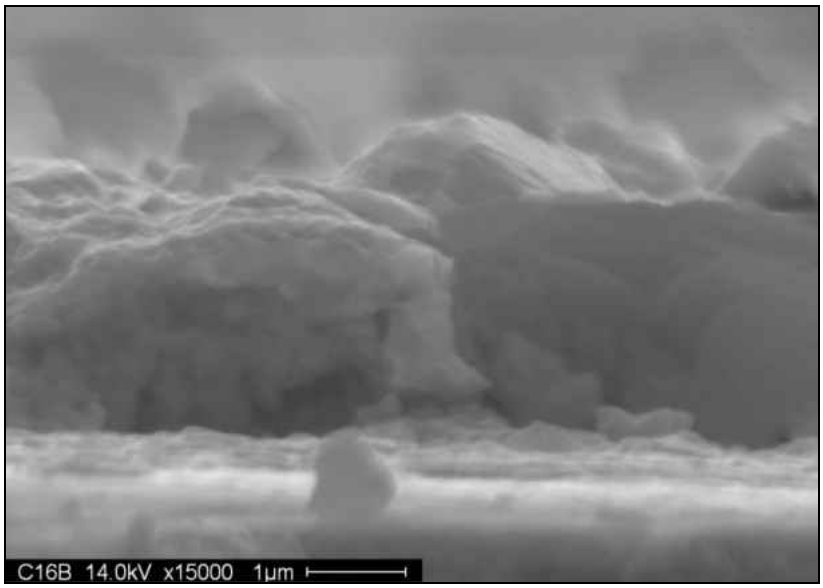

Figure 5.7: Cross sectional SEM image of CIGSe layer grown without NaF.

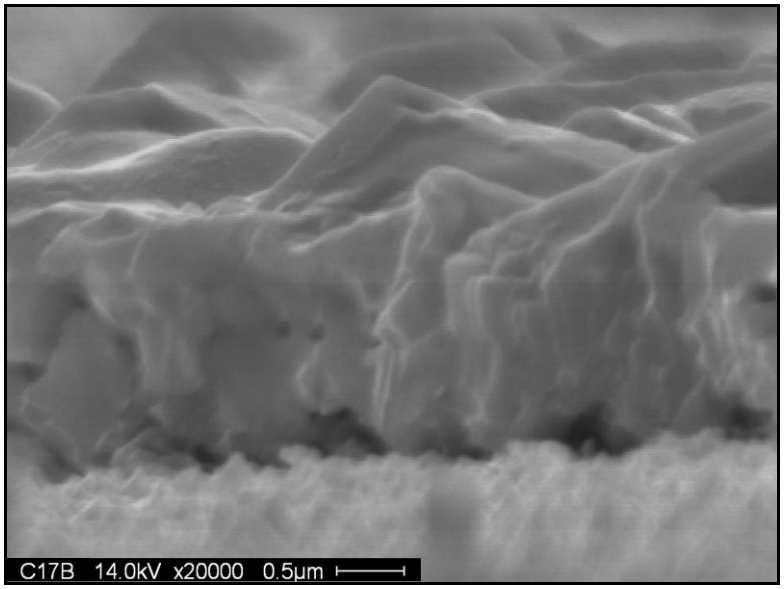

Figure 5.8: Cross sectional SEM image of CIGSe layer grown with 40 Å NaF.

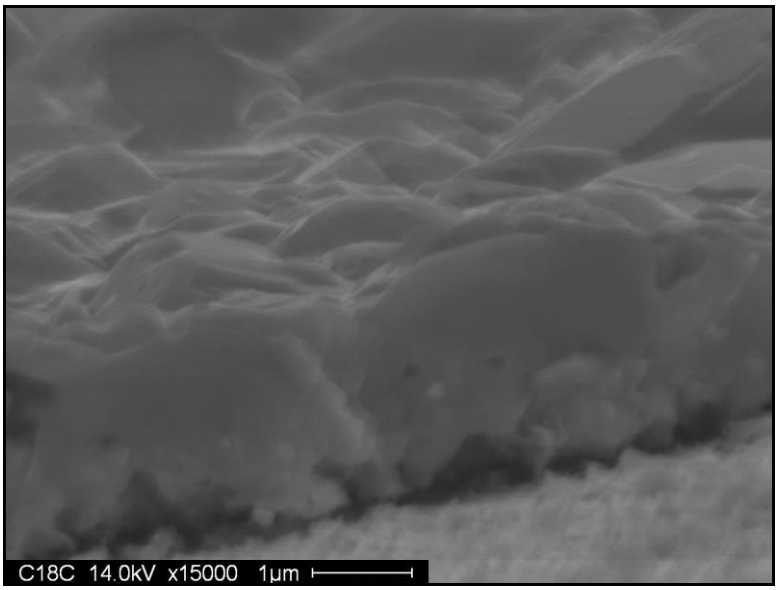

Figure 5.9: Cross sectional SEM image of CIGSe layer with 80 Å NaF.

Figure 5.10, Figure 5.11and Figure 5.12 shows the atomic force microscopy images of the CIGSe absorber without NaF, 40 Å NaF and 80 Å NaF respectively. The grains in the film with no NaF do not appear to be distinct and also has rougher surface with many pits. The surface roughness value measured from AFM is 310 nm. The film with 40 Å NaF appears to be comparatively crystalline and the grains appear to be distinct and large. The film appears to be porous. The porosity appears only on the surface and not in the bulk. The roughness of this sample measured from AFM is 210 nm. The film with 80 Å NaF appears to be highly crystalline with large and distinct grains. The 3-D image was taken exactly around the pit visible in the 2-D image of the same sample. This makes the film to look rougher than the film with 40 Å NaF. However 2-D image shows that the film is uniform with a very small pit. The roughness of the film is 160 nm. It can be concluded that a change in the microstructure of film is clearly visible with the presence of sodium during the absorber growth.

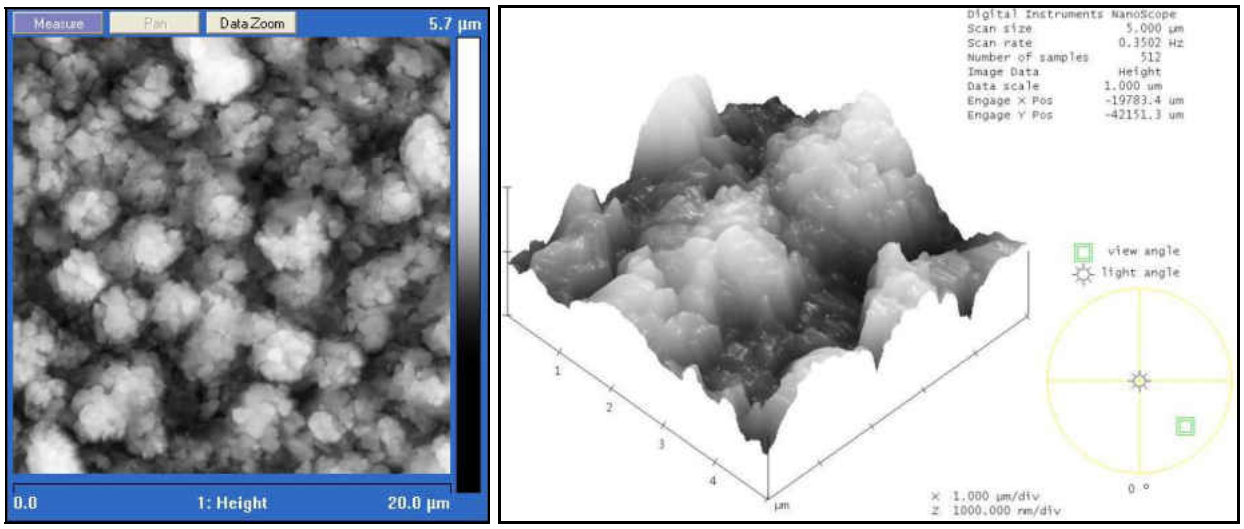

Figure 5.10: AFM image of CIGSe thin film with no NaF

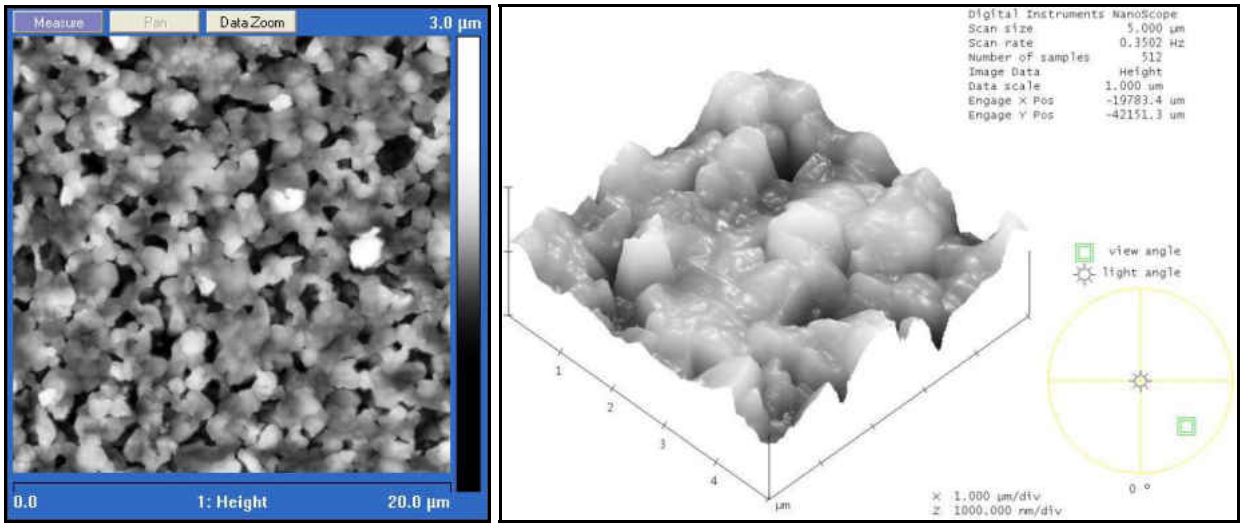

Figure 5.11: AFM image of CIGSe thin film with 40 Å NaF

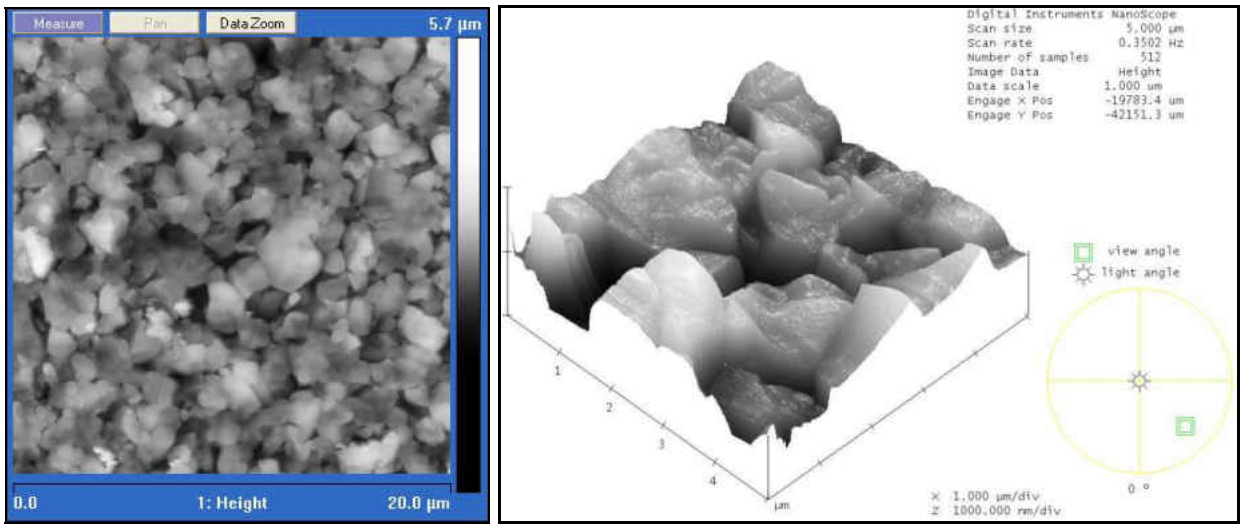

Figure 5.12: AFM image of CIGSe thin film with 80 Å NaF

5.2. Effects of Sodium on the CIGSeS Absorber

The effect of sodium on the grain growth, surface roughness and the orientation was clearly observed for CIGSe samples. Hence, further experiments were carried out to study the effect of sodium on CIGSeS thin films. In order to compare the effects of sodium, various amounts of sodium fluoride, viz., 40Å, 80 Å and 120 Å were deposited (Section 4.1.4) on molybdenum coated sodalime glass substrates. Silicon nitride barrier layer was deposited on the sodalime glass to minimize the out diffusion of sodium form the sodalime glass substrate. Therefore, the extent of sodium out-diffusion from the sodalime glass substrate is minimal. Based on the results from earlier experiments, samples without any NaF were not considered for this set. The CuGa-In precursors were deposited as described in Section 4.1.5. The following deposition parameters were kept constant for this set of experiments: CuGa - 350 Watt power at Ar pressure of 1.5 x 10^{-3} Torr and In - 230 Watt at Ar pressure of 7 x 10^{-4} Torr. The CIGSeS absorber layers were prepared by selenization/sulfurization of the CuGa-In precursors. Organometallic compound, diethyl selenide (DESe) was used as the selenium precursor. The

selenization process was carried out 515 ºC for 50 minutes. Sulfurization was carried out at the same temperature for 11 minutes.

Electron probe micro-analysis (EPMA) was carried out for the samples with 40 Å, 80 Å and 120 Å NaF. It was intended to grow the film in a copper poor regime. EPMA data confirms the films are copper poor (Table 5.3). The EPMA data shows that the Cu/(In+Ga) ratio for all films was in the range 0.76-0.77 and the Ga/(Ga+In) was 0.11-0.12. The value of S/(S+Se) ranges from 0.04 to 0.09. The values of the ratio are below the desired values.

Table 5.3: EPMA (@ 20 kV) of CIGSeS thin film with various amount of NaF.

NaF	Cu	In	Ga	Se	S	Cu/(In+Ga)	Ga/(Ga+In)	S/(S+Se)
40	21.87	25.25	3.36	45.12	4.40	0.76	0.12	0.09
80	22.05	25.53	3.08	46.36	2.98	0.77	0.11	0.06
120	21.86	25.66	3.13	47.57	1.77	0.76	0.11	0.04

A diffractometer with standard θ-2θ geometry was used for the X-ray diffraction analyses. The XRD patterns (Figure 5.13) reveal the major chalcopyrite reflections with no evidence of binary phase formation. The degree of preferred orientation was calculated using the technique mentioned earlier. The degrees of preferred orientation for the two peaks with highest intensity are given (Table 5.4). An increase in the degrees of preferred orientation is observed with an increase in the thickness of sodium fluoride for (112). Refer to APPENDIX A: Degree of Preferred Orientation Calculation for the detailed calculations of the degree of preferred orientation.

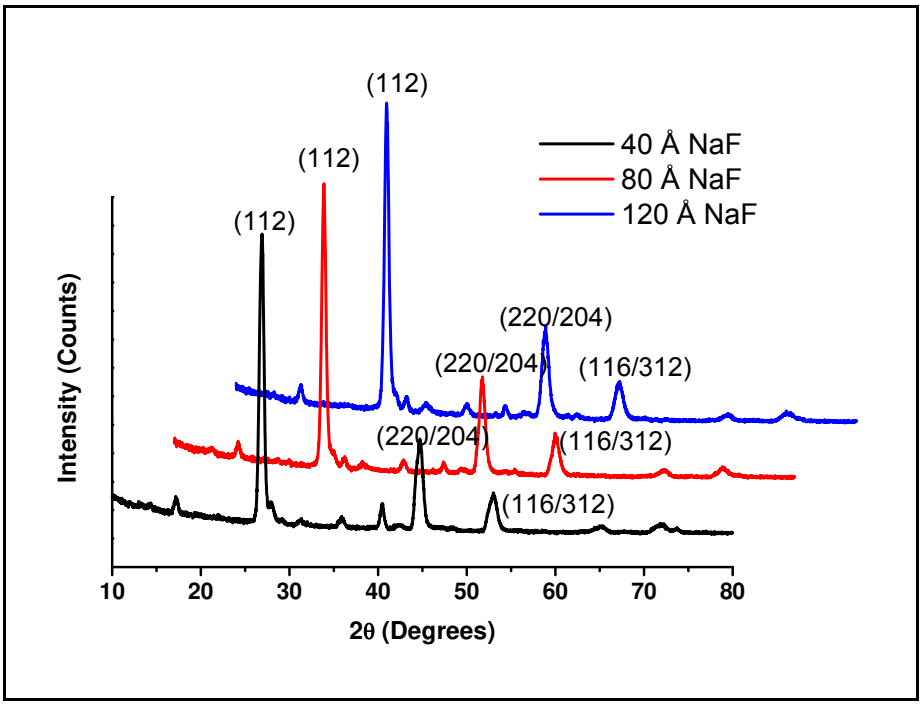

Figure 5.13: XRD spectra of CIGSeS thin films with various NaF thicknesses.

Table 5.4: Degrees of preferred orientation for CIGSeS thin film grown with different NaF thicknesses.

Orientation	40 Å	80 Å	120 Å
112	1.071	1.083	1.102
220/204	0.155	0.162	0.158

Figure 5.14, Figure 5.15 and Figure 5.16 show the scanning electron microscopy images of the CIGSeS thin film surface with 40 Å NaF, 80 Å NaF and 120 Å NaF respectively. The sample with 40 Å NaF exhibits disordered grain structure. The grain sizes were measured using the Mean Lineal Intercept Method (Heyn). The average grain size for the sample without NaF was ~0.5 μm (Figure 5.14). The sample also exhibits rough surface. The sample with 80 Å and 120 Å NaF show significant structural difference as compared to the other sample i.e., the grains

appear to be comparatively larger and exhibit significant faceting (Figure 5.15 and Figure 5.16). The surface also appears to be smoother with no large number of craters. The average grain size for the sample with 80 Å NaF are ~0.9 μm and for the sample with 120 Å NaF the size of the grains are ~1.2 μm. The films are densely packed and some porosity is visible only on the surface. A progressive increase of grain size with sodium precursor can also be observed for CIGSeS samples.

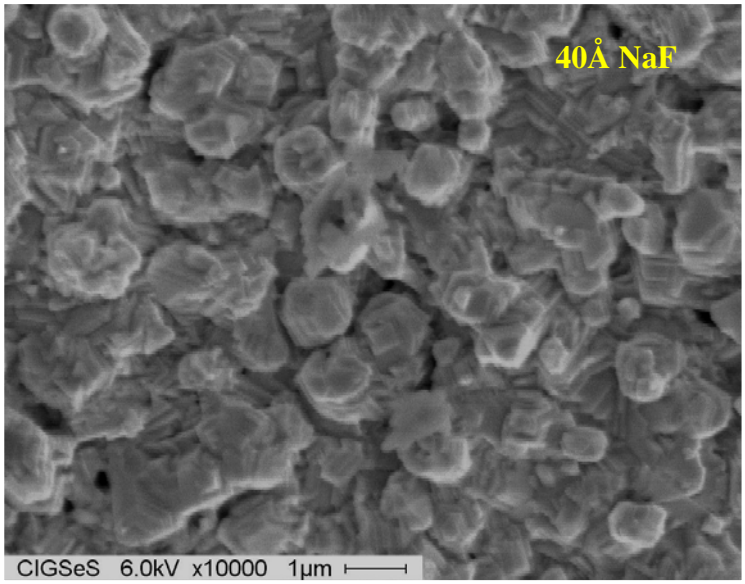

Figure 5.14: SEM of CIGSeS thin film surface grown on sodalime glass with 40 Å NaF.

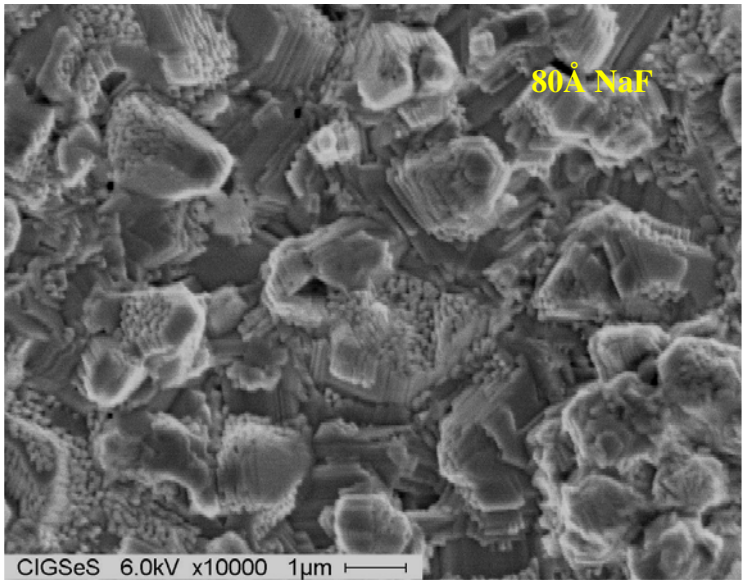

Figure 5.15: SEM image of CIGSeS surface grown on sodalime glass with 80 Å NaF.

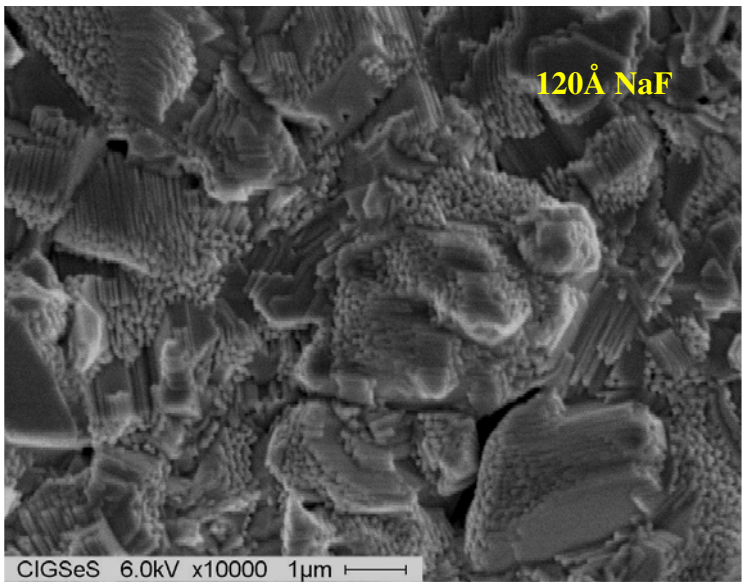

Figure 5.16: SEM of CIGSeS thin film surface grown on sodalime glass with 120 Å NaF.

Figure 5.17, Figure 5.18 and Figure 5.19 show the cross sectional SEM images of the CIGSeS thin films with 40 Å NaF, 80 Å NaF and 120 Å NaF respectively. The grains appear to be non-distinct and disorganized for the sample with 40 Å NaF. However, the films with 80 Å

NaF and 120 Å NaF exhibit large grains extending from the surface to the back. Some amount of porosity is observed in the images. This may be due to the loss of material during the sample preparation for cross sectional analyses.

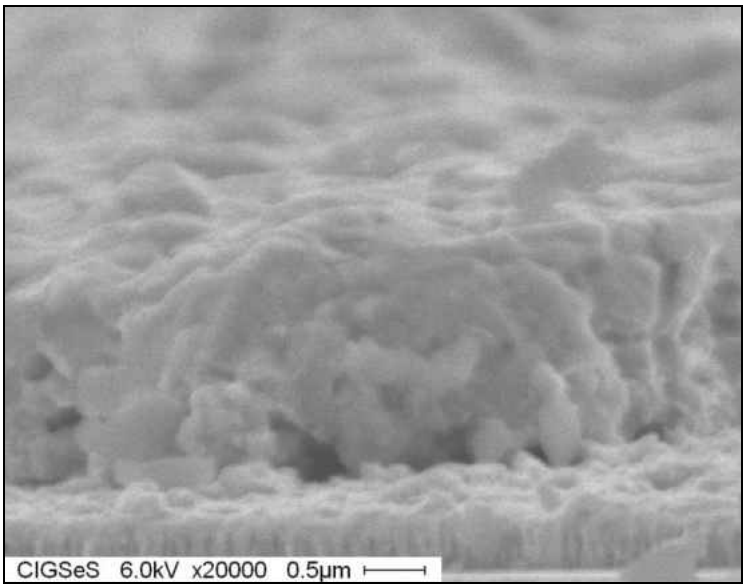

Figure 5.17: Cross sectional SEM image of CIGSeS thin film with 40 Å NaF

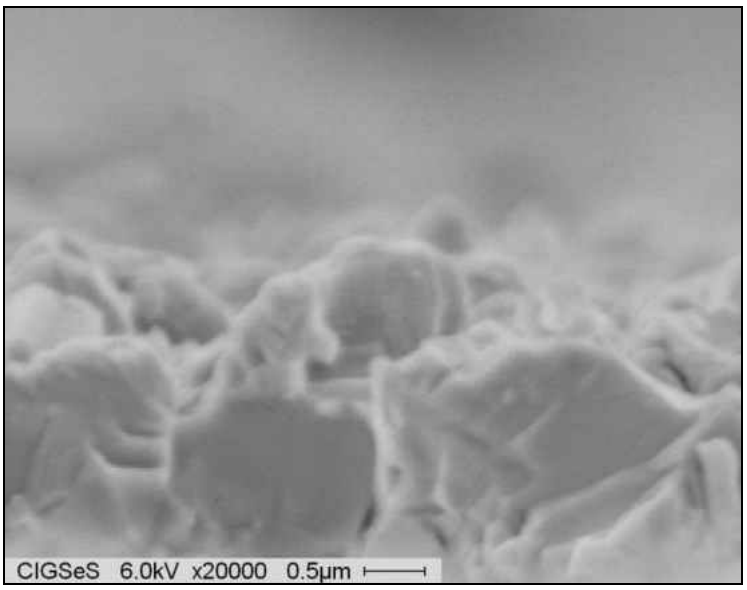

Figure 5.18: Cross sectional SEM image of CIGSeS thin film with 80 Å NaF

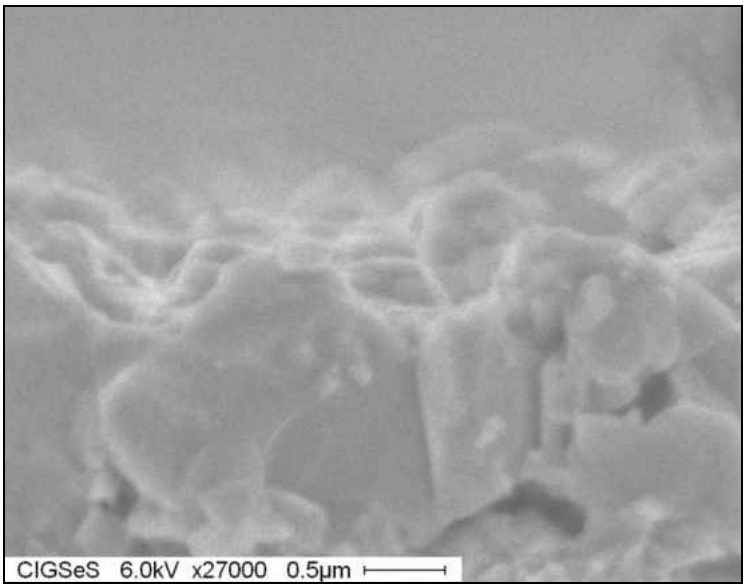

Figure 5.19: Cross sectional SEM image of CIGSeS thin film with 120 Å NaF

Atomic force microscopy analysis was carried out on the CIGSeS sample with 120 Å NaF (Figure 5.20). The roughness value of the sample measured from AFM analyses was 142 nm. The sample appears to be highly compact. The film also reflects high degree of crystallinity and faceting. This was also observed earlier in the SEM images.

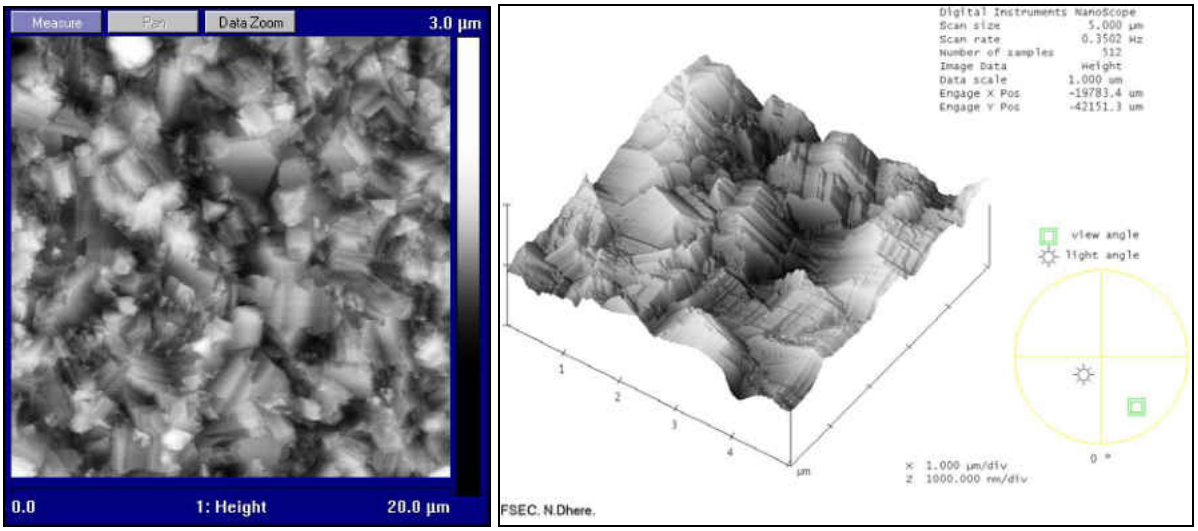

Figure 5.20: AFM image of CIGSeS thin film with 120 Å NaF

The EPMA data shows that amount of Cu, Ga and In present in all the film is almost equal. However, the amount of selenium increased and that of sulfur in the film reduced with an increase in the sodium fluoride quantity. The variation in the amount of sulfur may be attributed to the following: 1) better incorporation of selenium into the film and/or 2) variations in the grain size. Braunger et al reported that sodium acts as a selenium source by forming sodium polyselenide (Na_2Se_x) during the absorber growth [91]. This compound assists in better incorporation of selenium into the absorber and thus eliminates or reduces the selenium vacancies. As seen from the EPMA data the result is consistent with the model suggested by Braunger.

The microstructure of the film is formed during the selenization process and there is no change during the sulfurization process. According to Nakada *et. al*., the sulfur content is higher in the CIGSe absorber with smaller grains as compared to the absorber with larger grains. The SEM images indicate that the presence of sodium during the absorber preparation assists in growth of the grains and that later influence the incorporation of sulfur into the CIGSe absorber.

Observations:

The effects of sodium on the morphology and structure of CIGSe and CIGSeS were studied. The degree of (112) orientation for all the samples of CIGSe and CIGSeS except one CIGSe sample with no NaF was greater than one indicating that (112) orientation for all the samples. The value of lower than one for the CIGSe sample with no NaF can be due to the lower process temperature of 475 °C. Moreover, it can be observed that in all the samples the degree of (112) orientation shows progressive increase with amount of incorporated sodium. The presence of sodium during the absorber preparation leads to the increase in the grain size for both CIGSe

and CIGSeS thin films. The AFM analyses confirmed that the surface roughness of the films decreased with increase in the amount of sodium. The surface roughness value for sample with no NaF was 310 nm and for the sample with 80 Å NaF was 160nm. The amount of sulfur in the CIGSeS thin film decreased with increase in the amount of sodium. This may be due to better selenium incorporation into the film and thus better grain growth.

5.3. CIGSeS Thin Film Solar Cells Using DESe as Selenium Precursor

As mentioned earlier H_2Se gas is used as the selenium precursor for the preparation/manufacture of CIGSe or CIGSeS thin films. However, the risk of potential wide spread leak of highly toxic H_2Se gas from pressurized cylinders lead to the use of other alternative selenium precursors (Section 3.4.1). Diethyl selenide (DESe) was used to prepare small area CIGSeS absorber.

5.3.1. Optimization of Precursors Deposition Parameters

In the earlier research at the PV Mat Lab, CIGSe or CIGSeS thin film absorbers were prepared with a thickness of 2.7 μm. A set of experiments carried out to study the effects of sodium on the structure and morphology of CIGSe and CIGSeS absorber layers has been described in Section 5.1 and 5.2 respectively. The CIGSe and CIGSeS thin films absorbers were prepared with various amount of NaF and some samples were also prepared without NaF. In the initial set of experiments Cu-Ga and In precursors were only selenized at 475 ºC for 45 minutes using DESe as selenium source. Presence of sodium during absorber growth influenced the structure and morphology of the film. The surface roughness of the films reduced with increase

in the amount of sodium. An increase in the grain size as well as the degree of orientation for (112) was observed with increase in the sodium content.

The next set of experiments in the development of highly efficient CIGSeS thin film solar cells was aimed at reducing the thickness and refining the selenization and sulfurization processes. It was decided to reduce the thickness of the CIGSeS absorber layer to 1.8 – 2.0 μm because of the significant increase in the price of pure Indium in recent years. In this set of experiments, the metallic precursors, Cu-Ga and In were sputter deposited on molybdenum coated sodalime glass substrates for optimizing the process parameters. For all the experiments, the substrate movement time per unit distance was kept constant during Cu-Ga depositions. For the deposition of indium, different indium concentrations were obtained by varying the substrate movement times always reaching the desired total thickness. CIGSe absorber preparation in a copper rich regime leads to the formation of the Cu_2Se phase. The Cu_2Se phase is highly conductive. The presence of this phase diminishes the performance of the solar cell.

In the following set of experiments, one of the substrate was deposited with 40 Å NaF and the other three did not have any sodium addition. The effect of sodium on the absorber was not an important factor in this set experiment. The main aim was to optimize the selenization and sulfurization process parameters. Selenization experiments were carried out on four CuGa-In metallic precursors with various indium contents in the temperature range of 500 ºC – 515 ºC for a time period of 45 - 48 minutes using DESe as selenium precursor. The absorbers were also sulfurized for 12 minutes at the same temperature. The electron probe microanalyses (EPMA) of the absorber samples were carried out using e-beam accelerating voltage of 10 kV and 20 kV. The EPMA results with 20 kV e-beam energy are provided in Table 5.5. The Cu/In+Ga ratio for the Cu-poor film was approximately 0.86 and 0.90 and for the two Cu-rich samples was 1.02 and

1.07. The S/S+Se ratio for the Cu-poor samples was 0.23 and 0.54 and for the two Cu-rich samples the S/S+Se ratio was 0.17 and 0.22 The results indicate that the parameters used for the preparation of samples N3 and C8 were adequate to produce Cu-poor absorbers required for preparing devices.

Table 5.5: Composition of CIGSeS thin film absorbers from EPMA (@ 20 kV).

Sample Id	NaF (Å)	Selenization		Cu	In	Ga	Se	S	Cu/In+Ga	S/S+Se
		Temp	Time							
N4	40	500	45	25.96	20.54	4.85	37.69	10.96	1.02	0.23
N3	-	500	45	23.79	21.05	5.41	41.14	8.59	0.9	0.17
C7	-	515	48	26.55	20.1	4.74	22.2	26.38	1.07	0.54
C8	-	515	48	23.77	24.55	3.02	38.19	10.98	0.86	0.22

5.3.2. CIGSeS thin film solar cell with reduced thickness Deposition Parameters

The next set of experiments was designed to fabricate highly efficient CIGSeS thin film solar cells. CuGa-In precursors were deposited on molybdenum coated sodalime glass. 40 Å and 80 Å NaF were deposited by thermal evaporation on two molybdenum coated substrates layer prior to the deposition of the precursors. Both the samples were selenized at 515 ºC for 50 minutes and then sulfurized at the same temperature for 11 minutes. Similar selenization and sulfurization time and temperature were used for the fabrication of 13.73% CIGSeS thin films solar cell [62]. EPMA and SEM analyses were carried out to analyze the composition and morphology of the absorber film respectively. The elemental concentration of the absorber layer measured by EPMA (@ 20 kV) is given in Table 5.6. The Cu/In+Ga ratio of the absorber was

0.78 and 0.76. The S/S+Se ratio for the films with 40 and 80 Å NaF was 0.09 and 0.04 respectively. Cells were completed with the deposition of CdS heterojunction partner layer by chemical bath deposition, *i*:ZnO/ZnO:Al window layer were deposited by radio frequency magnetron sputtering and the Cr/Ag front contacts were deposited by thermal evaporation (Refer sections 4.1.7, 4.1.8 and 4.1.9). The thickness of the samples measured by Dektak profilometer was ~2 μm.

Table 5.6: Composition of CIGSeS thin film solar cells

Sample Id	NaF	Selenization		Atomic %					Cu/(In+Ga)	S/S+Se
		Temp	Time	Cu	In	Ga	Se	S		
B3	80	515	50	22.13	24.86	3.38	47.35	2.08	0.78	0.04
B5	40	515	50	21.87	25.25	3.36	45.12	4.4	0.76	0.09

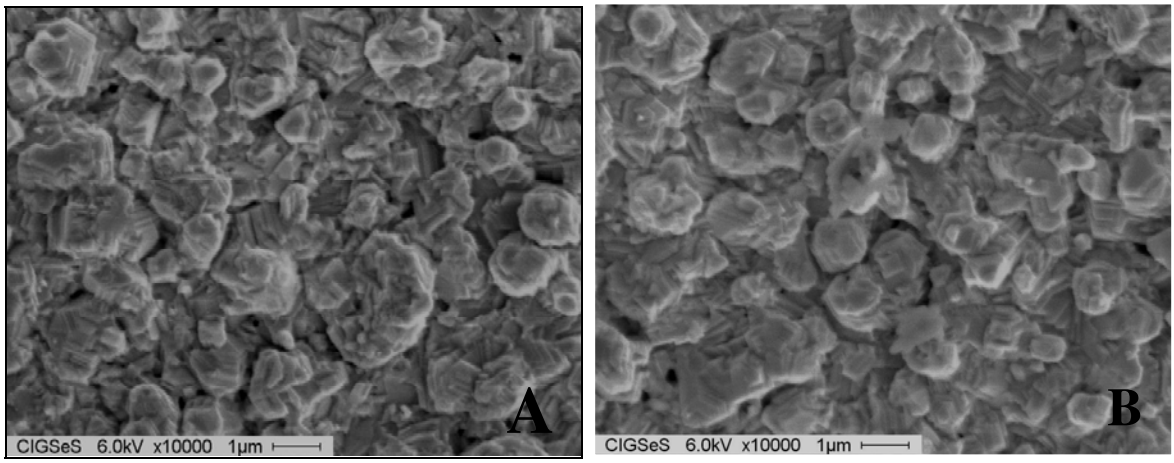

Figure 5.21: SEM image CIGSeS thin film absorber A) 80 Å NaF and B) 40 Å NaF

The SEM image of CIGSeS with 40 and 80 Å NaF (Figure 5.21) indicates the presence of highly crystalline, faceted surface and fairly free of pits. Sample with 80 Å NaF (Figure 5.21A) shows slightly large grains as compared to the sample with 40 Å NaF (Figure 5.21B). Table 5.7 show the current voltage characteristics for both of the CIGSeS thin film solar cell measured at PV Materials Lab at the Florida Solar Energy Center. The thickness of the absorber was reduced to ~2 μm. However, as mentioned earlier, the DESe partial pressure as well as the selenization time and temperature used for this set of experiments were same as used in preparation of highly efficient 2.7 μm thick CIGSeS thin film solar cells. As the available bulk material to be selenized was lower, it is possible that the amount of selenium provided as well as the selenization time and temperature could be more than optimum. This can damage the molybdenum back contact due to excessive reaction with selenium. It is speculated that this could be the reason for higher series resistance. After the CdS process it was observed that the solution contained yellow particulates which also had adhered to the surface of the film. Use of deionized water jet or ultrasonic cleaning did not remove the particulates. This was due to the some of the un-dissolved thiourea particles which may have served as nucleation sites. These particulates could lead to higher interfacial recombination and thus lower shunt resistance. The lower fill factor is because of the higher series resistance and lower shunt resistance resulting in lower efficiency. However, if the PV characteristics were measured at NREL then the efficiency of the solar cell would have increased to ~7.5% and ~6.5 % for samples with 80 Å and 40 Å NaF respectively.

Table 5.7: I-V Characteristics data for CIGSeS thin films solar cell

Parameters	80 Å NaF	40 Å NaF
Area (cm^2)	0.44	0.44
Open Circuit Voltage (V_{oc}) (mV)	450	450

Short Circuit Current Density (J_{sc}) (mA/cm^2)	31.62	27.24
Fill Factor (FF) (%)	38.33	37.93
Efficiency (η) (%)	5.45	4.64
Series Resistance (Ω-cm^2)	19.41	22.06
Shunt Resistance (Ω-cm^2)	414.24	397

Diethyl selenide was being used as the selenium precursors in the research and development of CIGSeS thin film solar cells. The last ampule of DESe was used and there was no availability of DESe at a reasonable price. The purity of the DESe used for the last set of experiments was less than the earlier. This might also be another reason for the reduction in the efficiency of the cell. The DESe available in the market was approximately $3000 per 25 grams. The price had increased approximately 10 times. An alternative material was investigated.

5.4. Development of Silicon Nitride Alkali Barrier and Molybdenum back contact.

A thin layer of silicon nitride is used as an alkali barrier in the $CuInSe_2$ based thin film solar cells. Efforts were made to develop silicon nitride alkali barrier layer. As mentioned earlier, reactive RF magnetron sputtering was used for the deposition of silicon nitride layer. The desired thickness of silicon nitride layer was 750 – 1000 Å. In the first set of experiments for the deposition of silicon nitride, the sputtering power was set to 225 Watt and the total pressure ($Ar+N_2$) was set at 1.6 mtorr. The substrate was moved linearly along the width of the target. Experiments were carried out with the substrates movement duration per unit distance being 150 sec and 300 Sec. The film appeared to be transparent as expected. However, the thicknesses of the film were below the detection limit of the thickness profilometer.

The substrates movement duration per unit distance for the next deposition was increased to 600 sec while the power was maintained at 225 Watt. However, even for this set the thickness was below the detection limit of the thickness profilometer. Hence, for the next set the sputtering power was increased to 425 W with the remaining parameters being constant. The film was transparent and the thickness of the film was ~1500 Å. The targeted alkali barrier thickness was 750-1000 Å. A thickness of ~750 Å was obtained in the next set of experiments reducing the substrates movement duration per unit distance to 300 sec while keeping the same sputtering power of 425 watt and the total pressure in the chamber of 1.6 mTorr.

Table 5.8: Deposition parameters for Silicon Nitride deposition

Power (Watt)	Time/Inch (sec)	Pressure (mTorr)	Thickness (Å)
225	150	1.6	NA
225	300	1.6	NA
225	600	1.6	NA
425	600	1.6	~1500
425	300	1.6	~750

Figure 5.22 shows the XRD spectra for the molybdenum layer with 110, 200 and 211 preferred orientations. The lattice parameter of the molybdenum was 3.14 Å. The value of lattice parameter closely matches with that of a random sample data (JCPDS Data). Transmission electron microscopy (TEM) analysis was carried out to study the silicon nitride – molybdenum layer deposited on sodalime glass. The samples were prepared using focused ion beam. Figure 5.23 shows the TEM image of silicon nitride and the 4 layer molybdenum. The first and the third

layer were tensile where as the second and the fourth layers were compressive in nature. The tensile layers are comparatively rougher and provide good adhesion to the glass whereas the compressive layers are smooth. Presence of smooth layer on the top is required for the growth of a smoother absorber. Alternate tensile and compressive molybdenum layers were deposited so as to nullify the net residual stress. The thicknesses of the molybdenum and silicon nitride layers as measured in the TEM were ~0.9 μm and ~750 Å. The sheet resistance measured at various locations of the sputtered molybdenum films was ~0.6 Ω/□.

EDS has a very low sensitivity for detection of lighter elements below the atomic number 11. However, the sensitivity also depends upon the instrument, operating conditions and mainly on the detectors window. Nitrogen has an atomic number 7 thus making it difficult to be detected by EDS. Hence, electron emission loss spectroscopy (EELS) was used to detect the presence of nitrogen in the silicon nitride. The bright strip (Figure 5.24) represents the nitrogen mapping from EELS.

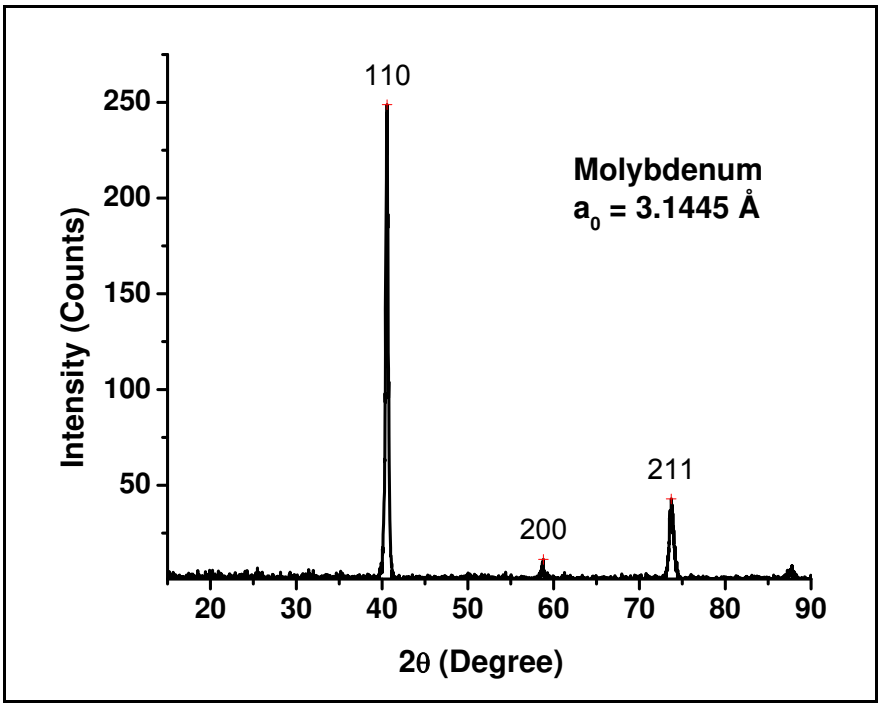

Figure 5.22: XRD spectra of 4-layer molybdenum.

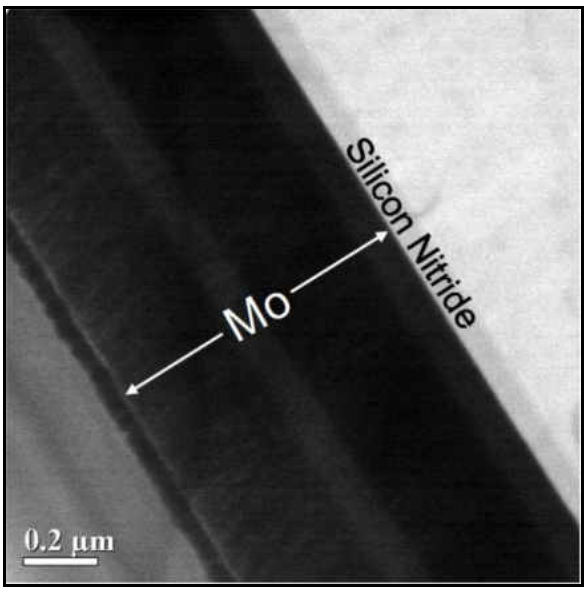

Figure 5.23: Bright field TEM image of silicon nitride - molybdenum layer on Soda lime glass

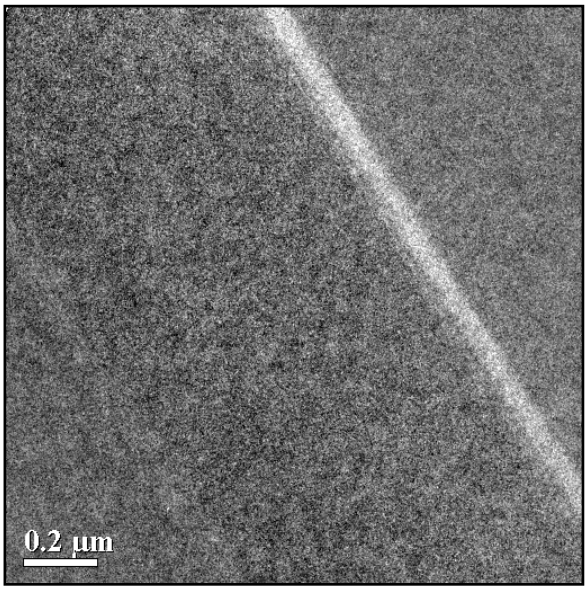

Figure 5.24: EELS mapping for nitrogen from the silicon nitride layer

5.5. Development of CIGSe thin film solar cells using DMSe as selenium precursor.

5.5.1. Selection of new selenium precursor

During the earlier part of the research DESe was used as the selenium source. However, it became essential to use an alternative selenium source for the CIGSe or CIGSeS absorber preparation because of sudden non-availability and substantial increase in price. Diethyl Diselenide ($DESe_2$) and Dimethyl Selenide (DMSe) were the choices of available other organometallic compounds. The vapor pressure of DMSe 308 mm Hg at room temperature is in the acceptable range. On the other hand, the vapor pressure of $DESe_2$ of 0.489 mm Hg at room temperature is too low for use in the present set-up. Hence, DMSe was selected as the new selenium precursor. DMSe has a boiling point of 58 ºC. The purity of DMSe being used was 99.99%. This is an order of magnitude lower than that of the DESe.

5.5.2. Selenization using DMSe as selenium precursor.

The diorganyl selenides dissociate at 450-600 °C with formation of elemental selenium, hydrogen selenide, carbon selenide and a mixture of hydrocarbons [125]. The experiments using DESe as the selenium source were carried out in the range of 475 - 515 °C with various dwells. In the initial experiments using DMSe as selenium precursor attempts were made to optimize the temperature for the preparation of CIGSe films. Hence, experiments were carried out at the high selenization temperature of 550 ºC with a long dwell of 60 minutes to study the effect complete dissociation of DMSe.

Silicon nitride alkali barrier layer and molybdenum back contact were deposited on the sodalime glass substrate. CuGa-In precursors were deposited by DC magnetron sputtering using the earlier deposition timings. Higher than required amount of DMSe for the formation of

stoichiometric CIGSe phase was introduced into the chamber during the absorber preparation. The excess amount of selenium is required to compensate for the loss of selenium due to out diffusion of selenium from the film. Sheet resistance was measured immediately after the sample was taken out of the furnace. This step gives a rough estimate about the sample being Cu-rich or Cu-poor. The sheet resistance of the film was 50 Ω/□. The sheet resistance indicated that the film was Cu-rich. EDS (@ 17 kV) and SEM were carried out to understand the chemical composition and the morphology of the film. EDS analyses (Table 5.9) shows that the CIGSe absorber is Cu-rich with the Cu/In+Ga ratio = 1.17. It is also evident from the EDS data that the amount of selenium in the film is adequate. As mentioned earlier, gallium diffuses to the Mo/CIGS interface during the high temperature absorber preparation process. Gallium signal as analyzed by EDS was below the detectable limit suggesting that gallium had diffused towards the back contact. Figure 5.26 shows the optical micrograph of the Cu-rich CIGSe absorber. It can be seen that the grains are large indicating a typical Cu-rich film. SEM image shows that the average grain size is ~0.7 μm measured by Heyns intercept method (Figure 5.27). The grains are large, well-faceted and compactly packed. This is a general trend in Cu-rich CIGSe thin films due to the formation of Cu_2Se phase. A few whiskers can also be observed in the SEM image suggesting that the film is Cu-rich.

Table 5.9: Chemical composition of Cu-rich CIGSe thin film absorber

Absorber	Atomic Percentage (@17 kV)			
	Cu	In	Se	Cu/(In+Ga)
$CuInGaSe_2$	27.32	22.31	50.37	1.17

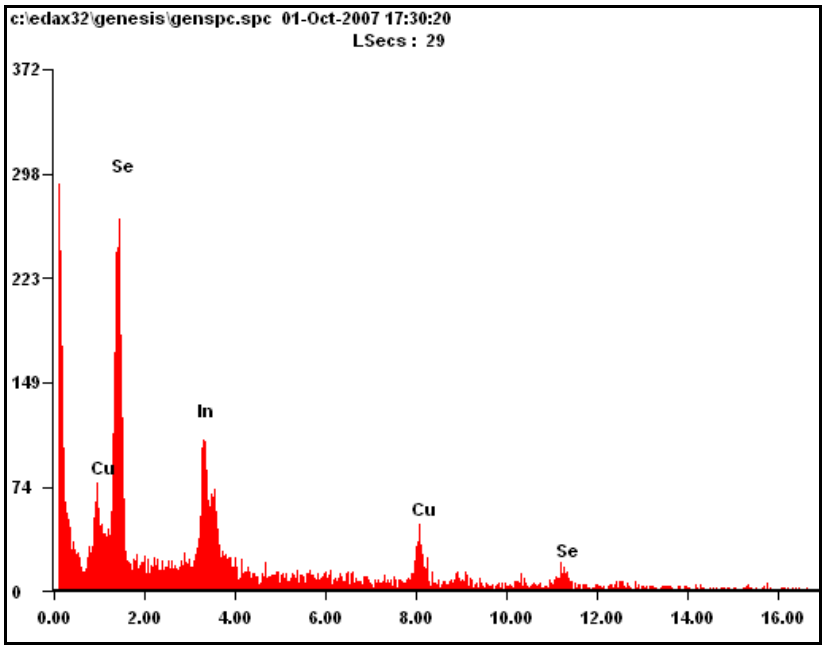

Figure 5.25: EDS of Cu-rich CIGSe thin film absorber

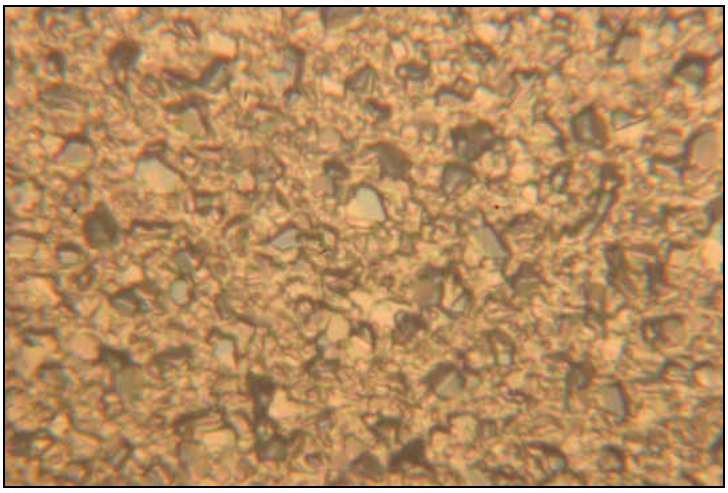

Figure 5.26: Optical micrograph of Cu-rich CIGSe absorber

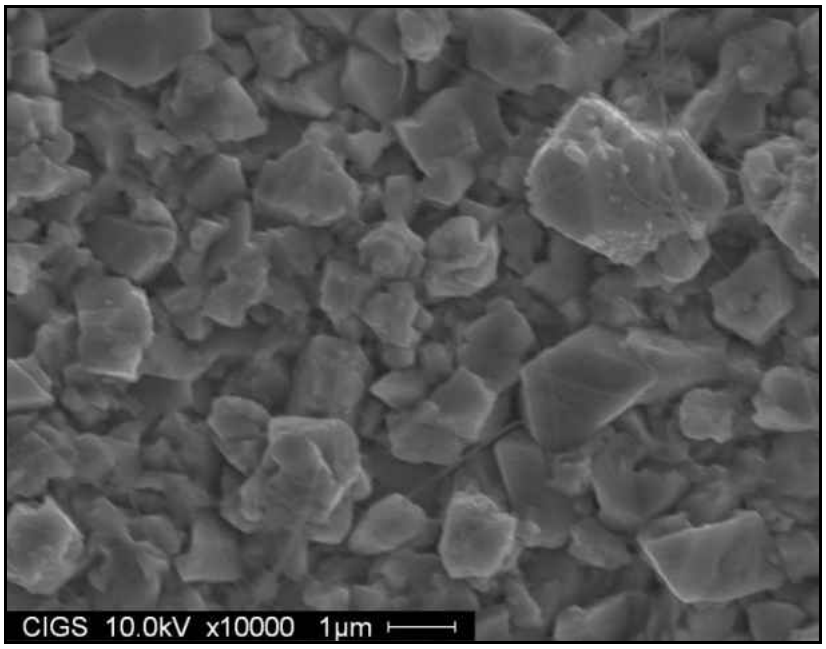

Figure 5.27: SEM image of Cu-rich CIGSe thin film absorber.

5.5.3. CIGSe thin film solar cell using DMSe as selenium source.

The CIGSe absorber from the previous experiment turned out to be Cu-rich. New precursor depositions parameters were calculated so as to obtain Cu-poor absorber. The amount of indium in the film plays an important role in the final thickness of the absorber. The thickness of the CIGSe absorber prepared in the earlier process was 2 - 2.1 µm. Hence, in the next set of experiments the Cu-Ga deposition timing was reduced while the In deposition timing was kept constant so as to achieve Cu-poor absorber. Silicon nitride alkali barrier layer and molybdenum back contact were deposited on the sodalime glass substrate. 80 Å of NaF was deposited prior to the precursor deposition. CuGa-In precursors were deposited by DC magnetron sputtering using the earlier deposition parameters. Selenization process was carried out for 60 minutes at 550 ºC.

After the selenization process the sample appeared to be light grey in color. No black soot was seen on the absorber. The sheet resistance of the sample was 40-50 kΩ/□. Optical

micrograph (Figure 5.33) showed that the film surface is uniform. The samples were etched using 10% KCN for 3 minutes with continuous agitation prior to the deposition of *n*-type, CdS layer using the chemical bath deposition technique (Section 4.1.7).

It was observed that the CdS reaction occurred faster to produce homogeneous solution resulting in the deposition of particulates on the film. It should be noted that the thiourea solution used during the CdS deposition was not filtered leading to the presence of undissolved thiourea particles in the solution. These undissolved thiourea particles may have served as nucleation sites causing homogeneous nucleation of CdS on the absorber. Deionized water jet or ultrasonic cleaning did not remove the particulates.

Hence, it was decided to filter the thiourea solution before being used for the CdS deposition. It was observed that now the time required for the formation of a typical blue colored film (indicating ~50 nm thick) was comparatively higher. A clean blue colored uniform film was observed on the surface (Figure 5.28). Figure 5.29 shows the TEM image of the CIGSe thin film solar cell. The presence of a uniform CdS layer can be confirmed from the TEM image. The film appears to be porous. The porosity in the film is an artifact of the sample preparation using focus ion beam.

Figure 5.28: CdS Deposited CIGSe Absorber

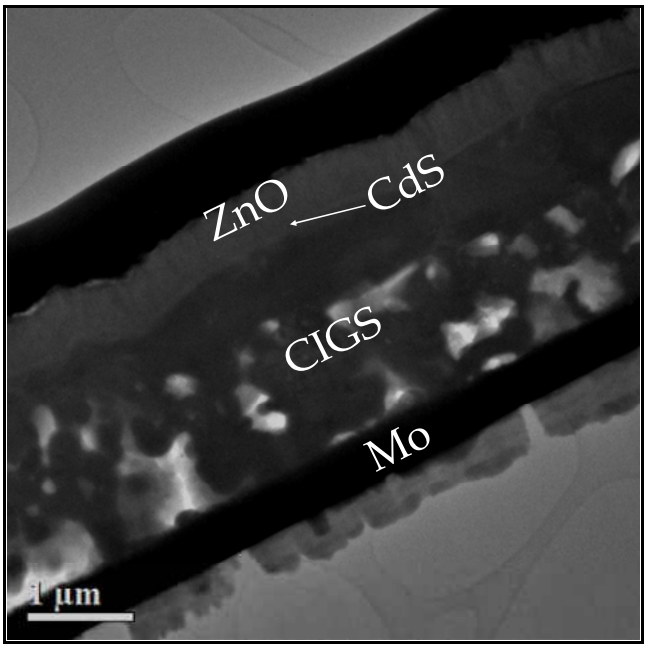

Figure 5.29: TEM of CIGSe thin film solar cell. Uniform CdS layer can be observed.

The CIGSe thin films were competed by the deposition of i:Zno/Zno:Al window layer by RF magnetron sputtering and the front contacts by thermal evaporation. Sheet resistance and transmittance measurements were carried out on a series of series of ZnO window layers. The thickness of the TCO layer was found to be 900 – 950 nm and the transparency was < 85%. The sheet resistance was 10- 20 Ω/□. The desirable sheet resistance of the TCO layer is as low a possible. The front contact grid area is small hence the sheet resistance can be 50-60 Ω/□. The substrate movement time per unit distance was reduced by half while keeping the remaining parameters same. The targets were presputtered for ~15 minutes so as to remove any undesired contaminants from the surface of the target. The TCO thickness was reduced to ~500 nm and the transparency was >90 % for the visible light. The sheet resistance of the film was 40-50 Ω/□. Figure 5.30 shows the transparency plots for the ZnO window layers with two different ZnO thicknesses. As expected the transparency of the thinner film was higher.

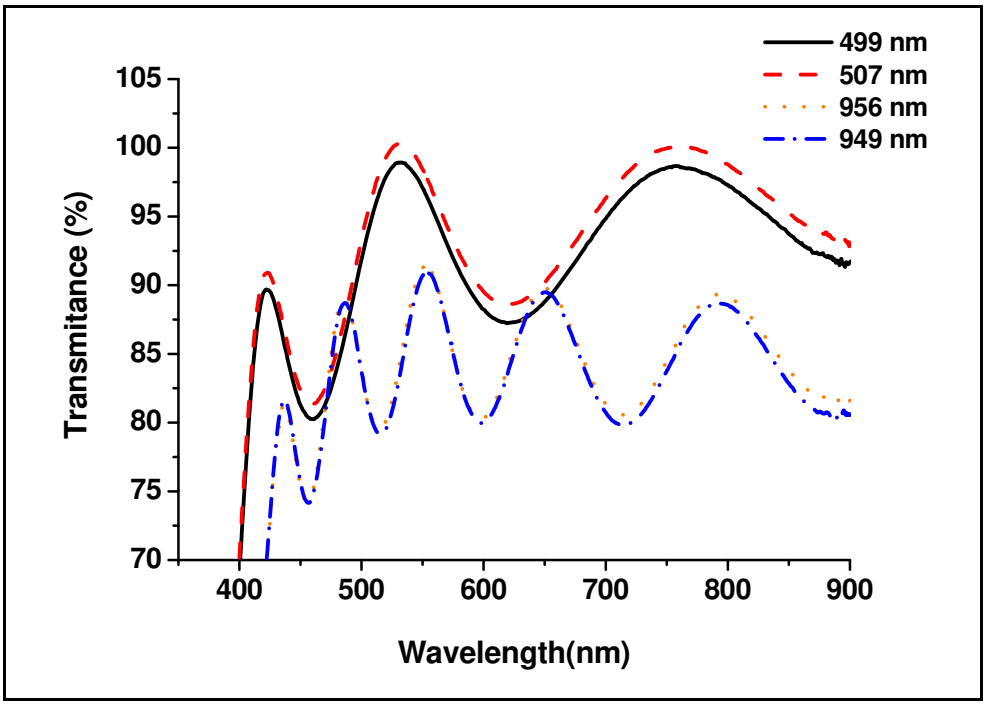

Figure 5.30: ZnO Transparency Plots

Chemical composition of the film from the EDS data (Table 5.10) measured at 18 kV shows that the film is copper poor and with ~50 at% Se. The Cu/(In+Ga) ratio was 0.877.

Table 5.10: Elemental analyses of CIGSe thin film.

Analyses	Atomic Percentage				Cu/In+Ga
Sample ID: C38	Cu	In	Ga	Se	
EDS (@18 kV)	23.62	23.40	3.54	49.44	0.877

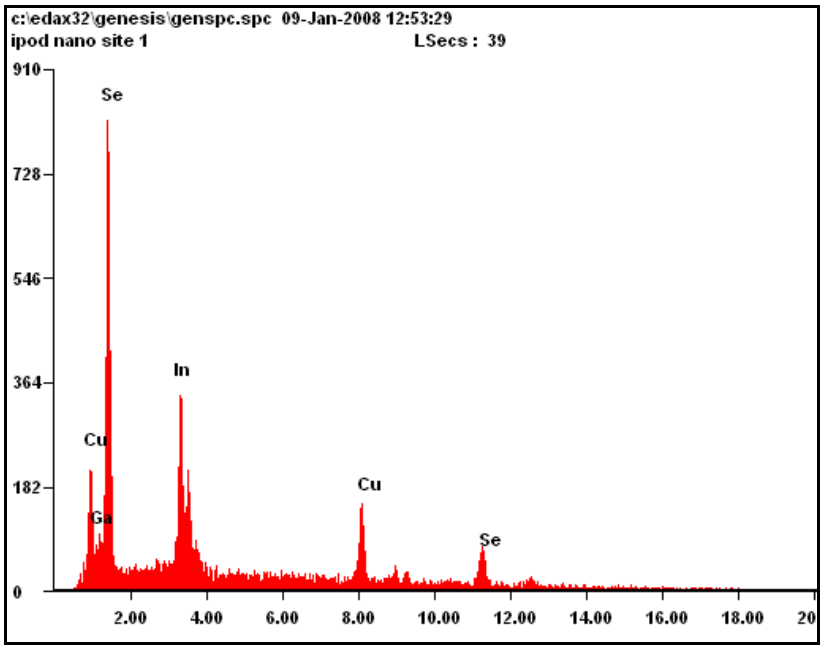

Figure 5.31: EDS spectra of CIGSe Thin Film

The XRD pattern for the CIGSe thin film provided in the Figure 5.32 shows (101), (112), (103), (211), (105), (220/204), (312/116), and other reflections of highly crystalline chalcopyrite CIGSe and also reflections from molybdenum. The strongest reflection was from (112) plane at $2\theta = 26.66°$. The *d*-spacings for (220) and (204), (116) and (312), (008) and (400) of CIGSe are very close. Hence for each peak both of the reflections have been indicated in the XRD spectra. The lattice parameters calculated using the XRD data were $a_0 = 5.786$ Å and $c_0 = 11.596$ Å. The *d*-spacings of the planes calculated from XRD data of the film closely match with those of a $CuInSe_2$ phase. The molybdenum reflection was observed at $2\theta = 40.46°$. Even though the EDS data indicated Ga content to be 3.54 at % , XRD data shows that most probably the gallium has segregated near the Mo-back contact and composition of the bulk of the film was nearer to $CuIn_{0.9}Ga_{0.1}Se_2$ phase.

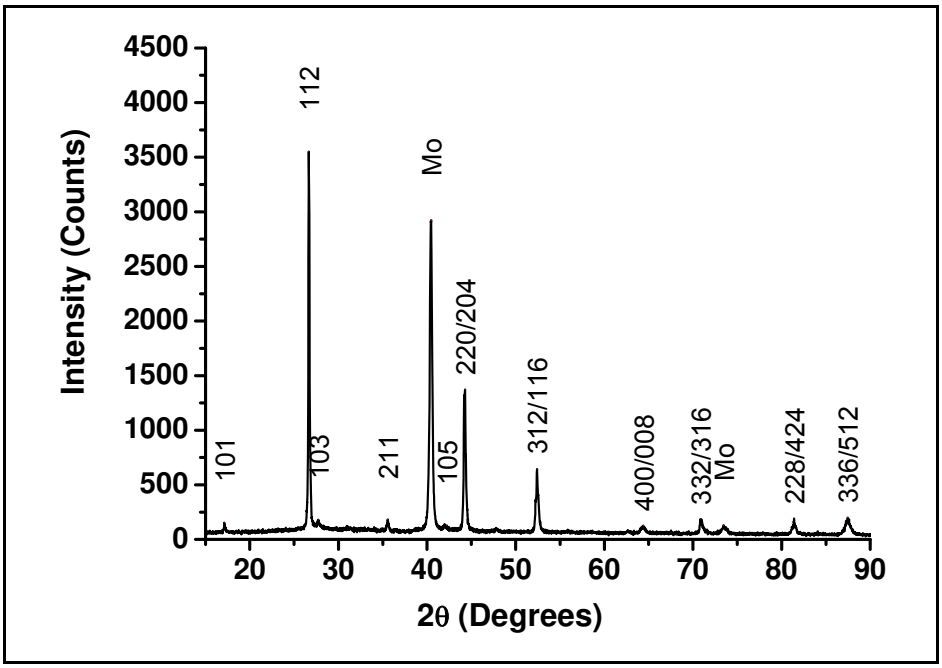

Figure 5.32: XRD spectra of CIGSe thin film

Figure 5.33 shows the optical micrographs of the CIGSe thin film absorber at x50 and x500. The film appears to be uniform from the micrograph (x50). As can been seen from the micrograph (x500) the grains appear to be uneven. Figure 5.34 shows the SEM image of the CIGSe thin films absorber. The image reveals that the grains are compactly packed, and uneven in size. The average grain size measured by the Heyns intercept method was ~0.35 micron.

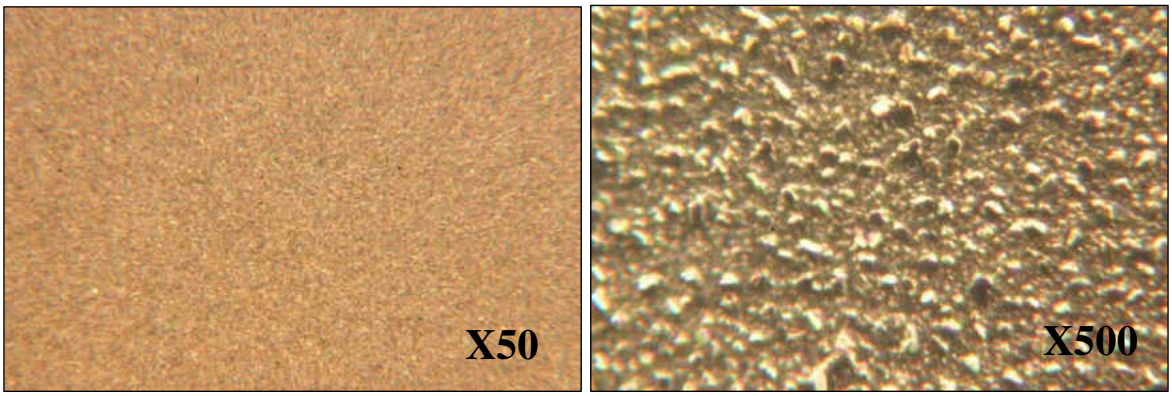

Figure 5.33: Optical Micrographs of CIGSe thin film

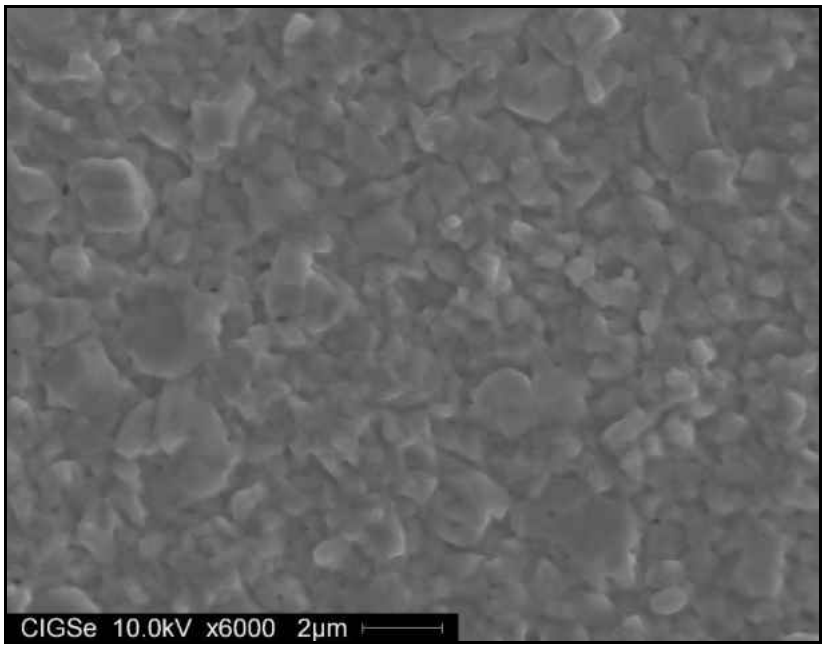

Figure 5.34: SEM of CIGSe thin film absorber.

Figure 5.35 shows the TEM image of the CIGSe thin film solar cell. A thick uniform $MoSe_2$ layer can be seen at the Mo/CIGSe interface. EDS line scans were carried out at the Mo/CIGSe interface during TEM analyses. Figure 5.36 shows the count ratio of selenium for both K and L with a compositional ratio of 2:1 (region within the two vertical lines). This suggests the formation of a $MoSe_2$ layer complementing the TEM micrographs. However, the XRD spectra did not reflect the presence of the $MoSe_2$ formation. The thickness of the $MoSe_2$ layer is ~0.1 μm. A thick $MoSe_2$ layer affects the solar cell performance due to an increase in the series resistance. This suggests that the time and temperature to prepare CIGSe absorber is probably higher than optimum.

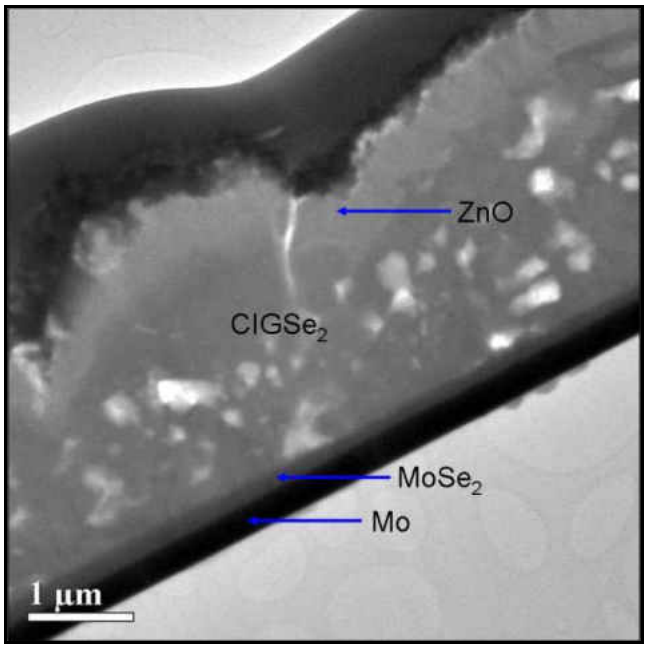

Figure 5.35: TEM of CIGSe thin film with a thick $MoSe_2$ layer.

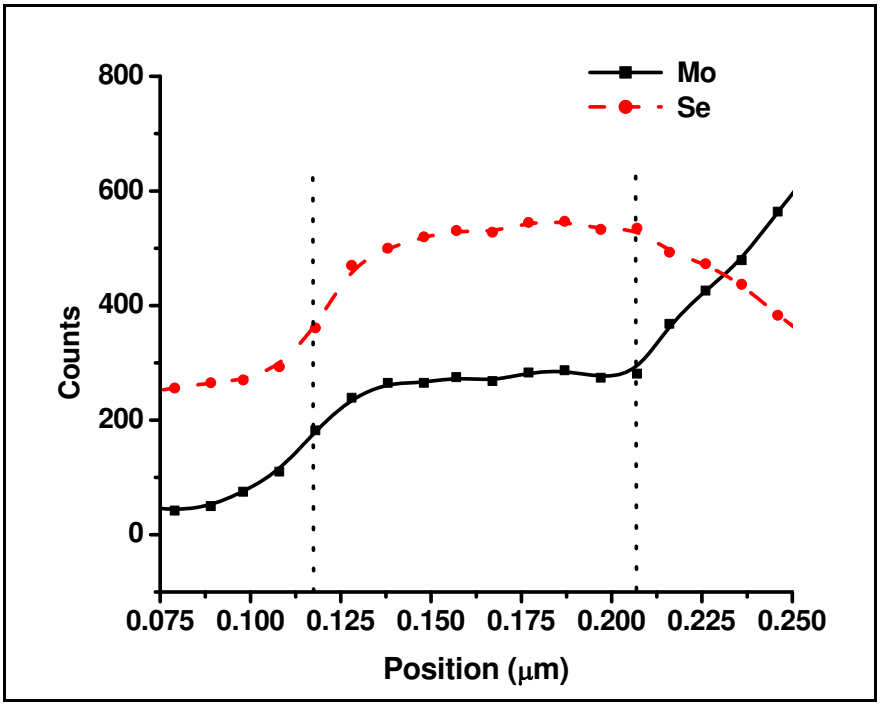

Figure 5.36: Mo/CIGSe interface line scan obtained by EDS. Count ratio of Mo and Se for K+L

i:ZnO and the transparent conducting oxide, ZnO:Al of an optimum thickness were deposited on the CdS layer. Finally chromium-silver front contacts were deposited. Current-Voltage (I-V) measurements were carried out at FSEC. Few selected samples were sent to National Renewable Energy Laboratories (NREL) for I-V and quantum efficiency (QE) certification. The I-V and QE curves provide valuable information about the solar cell and the potential areas of improvement.

Initially the PV cell parameters measured at NREL were~10–25% better as compared to the FSEC measured data. Hence, attempts were made to modify the I-V set-up to improve the measurement accuracy. Samples were prepared and measured using the new I-V set-up. Process parameters were also changed so as to improve the efficiency of the cell. However, the performance of the cells did not improve much. One of the cells with a moderately improved efficiency was sent to NREL for I-V measurements. Figure 5.37 shows the I-V curve of the CIGSe/CdS thin film solar cell measured at NREL. The CIGSe/CdS solar cell fabricated using selenization technique using DMSe has an efficiency of 6.52%. The I-V measurements carried out at FSEC had shown an efficiency of 3.5 %. Hence, unfortunately the resultant set-up did not improve rather the performance was further reduced due to instrumental errors. Table 5.11 gives all the device parameters for the CIGSe/CdS solar cell. The short circuit current density value of 31.97 mA/cm^2 is comparable with highly efficient with CIGSe solar cells. However, the fill factor and the open circuit voltage values are lower. TEM image and EDS line scan showed the formation of 0.1 μm $MoSe_2$ layer that might lead to a higher series resistance and consequently lower fill factor. Nickel has better lattice matching with ZnO. Hence, the FF can be further improved by using Nickel-Aluminum as front contact fingers instead of chromium-silver.

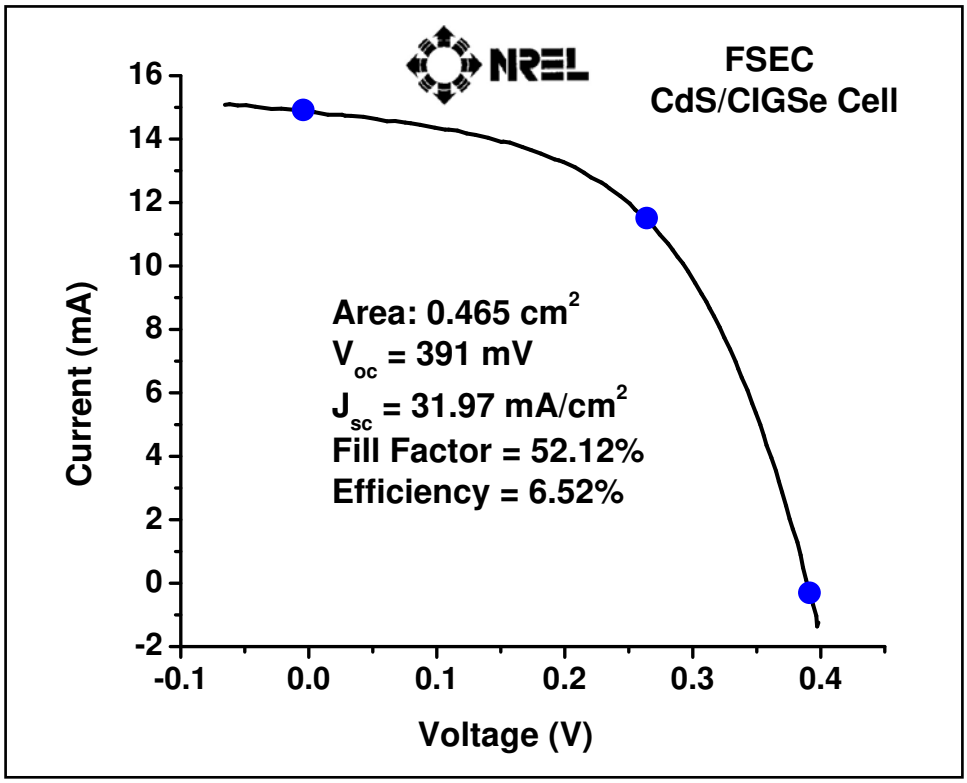

Figure 5.37: Current – Voltage characteristics of CIGSe thin film solar cell

Table 5.11: CIGSe Solar Cell Parameters

Area	0.465 cm^2
Open Circuit Voltage (V_{oc})	391 mV
Short Circuit Current (I_{sc})	14.853 mA
Short Circuit Current Density (J_{sc})	31.972 mA/cm^2
Peak Voltage (V_{max})	267 mV
Peak Current (I_{max})	11.335 mA
Fill Factor (FF)	52.12 %
Efficiency (η)	6.52 %

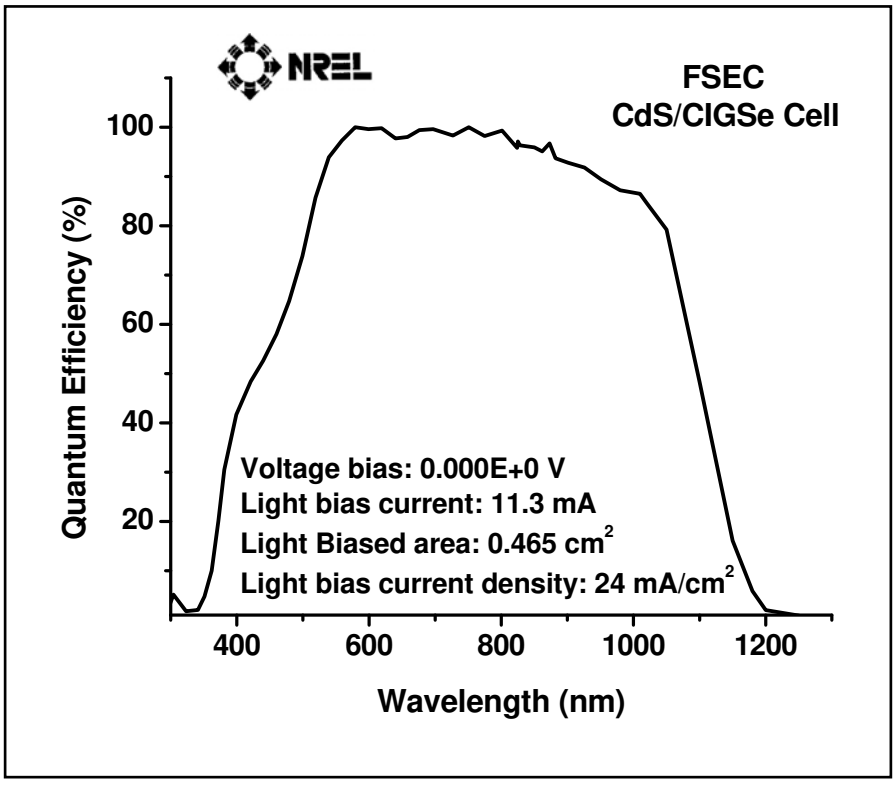

Figure 5.38: Quantum efficiency characteristics of CIGSe thin film solar cell

Figure 5.38 shows the QE curve of the CIGSe thin film solar cell measured at NREL. Reasonably flat response was observed in the wavelength range of 500 – 850 nm. The expected loses in the blue photon region due to the higher bandgap CdS layer is seen in the QE curve. Moreover, the response at higher wavelengths suggests some recombination loses near Mo-CIGSe interface.

5.6. Development of CIGSeS Thin Film Solar Cells

Fabrication of CIGSe thin film solar cells using organometallic compound, DMSe was successfully demonstrated. As discussed before, addition of sulfur to CIGSe absorber increases the open circuit voltage and hence the efficiency of the solar cell. Efforts were made to improve the process for CIGSeS thin film absorbers. Sulfur replaces or occupies the selenium vacancies

in lattice. It is advisable to first partially selenize and then sulfurize. Hence it is essential to optimize the selenization parameters in order to prepare device quality CIGSeS absorber.

CuGa-In precursors were deposited on molybdenum coated sodalime glass substrates. The deposition timings were optimized so as to achieve a copper poor absorber. Selenization experiment was carried out at 450 ºC for 45 minutes with 9 torr DMSe. The sulfurization experiment was carried out at 525 ºC for 5 minutes in diluted H_2S gas. Samples were also annealed at 550 ºC for homogenization. The heterojunction partner layer, CdS was deposited by chemical bath deposition, ZnO window layer was deposited by RF magnetron sputtering and finally the front contacts, Cr-Ag fingers were deposited by thermal evaporation.

EPMA and EDS were carried out to study the composition of the film and XRD was used to study the structure and the phases. SEM and TEM analyses were carried out to study the microstructure.

Table 5.12 shows the composition of the CIGSeS absorber as measured by EPMA and EDS. The EPMA data provided in the thesis is a 10 point average value. The EPMA data shows that the films are Cu-poor with the Cu/In+Ga ratio = 0.92 and the S/S+Se ratio was 0.47. The 20 keV EPMA data indicate that the formation of $Cu(In_{0.69}Ga_{0.31})(Se_{0.53}S_{0.47})_2$ phase. Figure 5.39 shows the EDS spectra for the CIGSeS thin film absorber. The amount of sulfur in the film is excessive. As mentioned earlier, for optimum performance, it is essential that sulfur be incorporated near the absorber surface. As sulfur diffuses further into the absorber film toward the back contact, bandgap of the bulk of the absorber film increases. This increase in the bandgap is due to the lowering of the valence band maxima. The lowered valence band maxima at the absorber-back contact interface acts as a mirror for holes and reflects the holes away from the

back contact. This results in increase of the recombination of the holes and thus reducing the generated current.

Table 5.12: Chemical composition of CIGSeS thin film selenized at 450 ºC.

Analyses	Atomic Percentage					Cu/In+Ga	S/S+Se
	Cu	In	Ga	Se	S		
EPMA (@20 kV)	25.01	18.81	8.39	25.47	22.32	0.92	0.47
EDS (@16 kV)	24.07	19.6	6.15	26.59	23.59	0.93	0.47

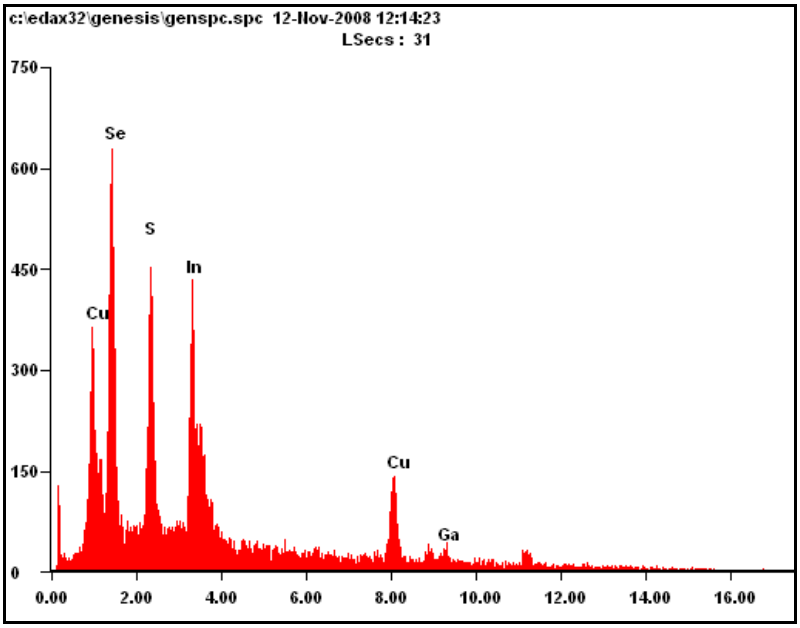

Figure 5.39: EDS spectra of CIGSeS thin film selenized at 450 ºC

The XRD pattern for the CIGSe thin film provided in the Figure 5.40 shows the (101), (112), (201), (211), (220/204), (312/116), and other reflections of highly crystalline chalcopyrite CIGSe and also the reflection from molybdenum. The molybdenum reflection was observed at $2\theta = 40.52°$. The strongest reflection was from (112) plane at $2\theta = 27.62°$. This indicates the

presence of a significant amount of sulfur. The lattice parameters calculated using the XRD data were a_0 = 5.586 Å and c_0 = 11.161 Å.

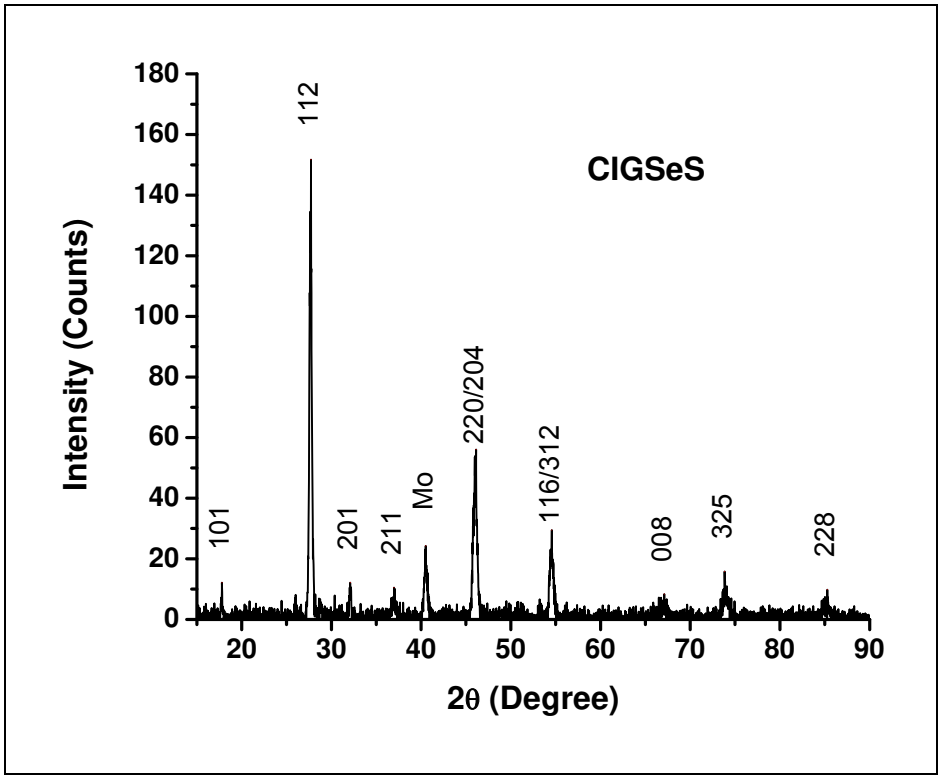

Figure 5.40: XRD spectra of CIGSeS thin film selenized at 450 ºC for 45 minutes

Figure 5.41 shows the optical micrographs of the CIGSeS thin film absorber selenized at 450 ºC. Figure 5.42 and Figure 5.43 shows the surface SEM image and the cross sectional TEM image of the CIGSeS sample. It is evident from the SEM image that the surface even. However, the TEM image shows the presence of some pits that are up to ~0.25 μm deep. The film also appears to be porous at the molybdenum-CIGSeS interface. The porosity may be an artifact of sample preparation by focused ion beam milling.

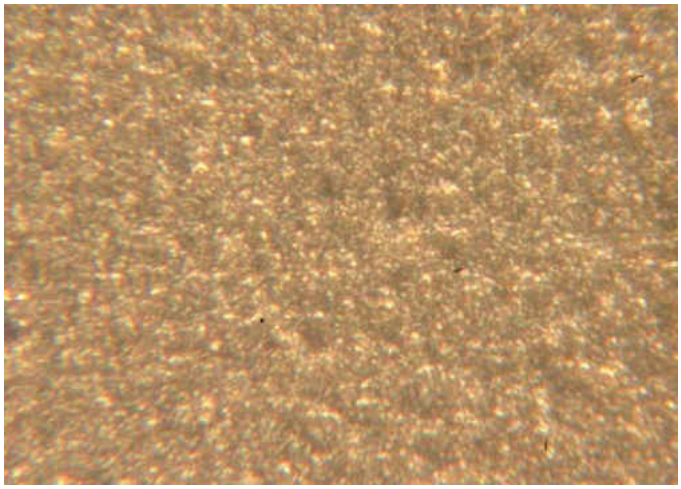

Figure 5.41: Optical micrograph (x500) of CIGSeS thin film selenized at 450 ºC.

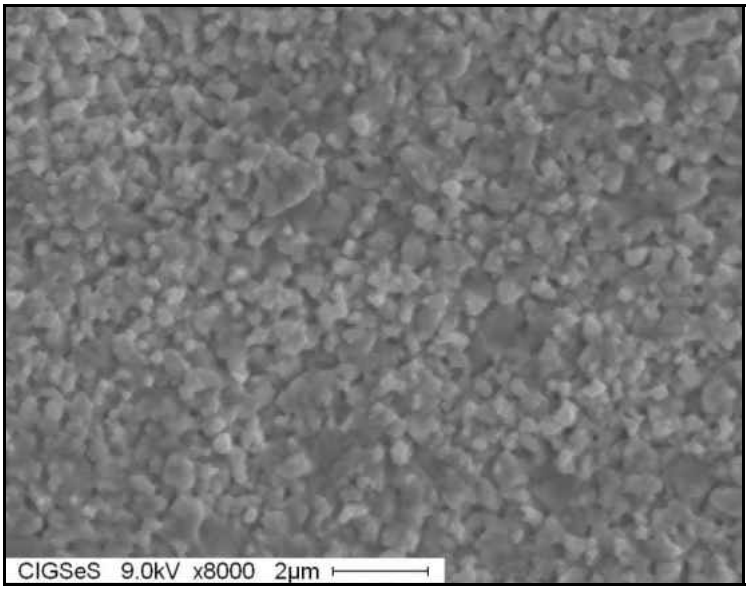

Figure 5.42: SEM image of CIGSeS thin film selenized at 450 ºC for 45 minutes.

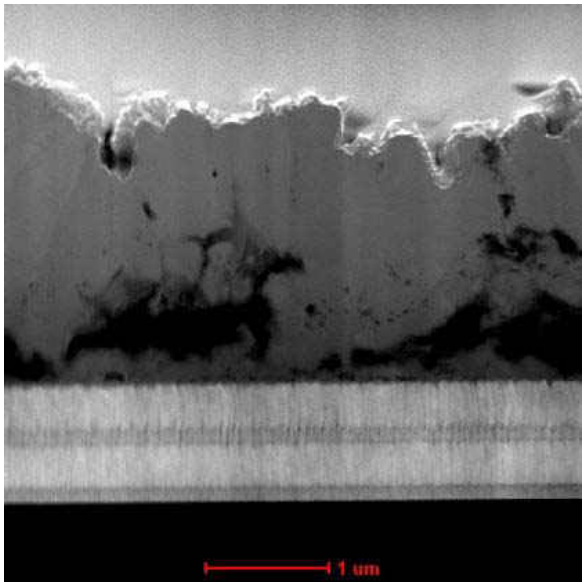

Figure 5.43: Bright filed TEM image of CIGSeS thin film selenized at 450 ºC for 45 minutes.

The current-voltage (I-V) characteristics were measured under simulated AM 1.5 spectrum using an in-house built I-V setup. The cells prepared on this absorber had inferior device properties. The device properties of the cell with maximum efficiency are as follows: V_{oc}= 250 mV, J_{sc}= 21.47 mA/cm^2, fill factor = 34.37 %, efficiency= 1.84 %. The series and shunt resistance were 16 Ω-cm^2 and 65 Ω-cm^2 respectively. The shunt resistance and the fill factor indicate that the quality of the bulk of the absorber needs to be improved so as to improve the efficiency of the cell. From above analyses it can be concluded that the absorber was not selenized enough suggesting the need for higher selenization temperature. Thus, the selenization temperature was increased to 475 ºC.

Experiment: Selenization Temperature - 475 ºC and Time - 35 Minutes.

Selenization at higher temperature would enhance the selenium incorporation into the absorber. The precursor sample for absorber preparation was chosen from the same 6”x4” inch

substrate as used in the earlier experiment. Selenization of the precursors was carried out at 475 ºC for 35 minutes in diluted DMSe in forming gas atmosphere. The sulfurization experiment was carried out at 525 ºC for 5 minutes in diluted H_2S gas. Samples were also annealed at 550 ºC for homogenization. The heterojunction partner layer, CdS was deposited by chemical bath deposition, *i*:ZnO/ZnO:Al window bi-layer was deposited by RF magnetron sputtering and finally the front contacts, Cr-Ag fingers were deposited by thermal evaporation.

EDS was carried out to study the composition of the film. SEM and TEM analyses were carried out to study the microstructure.

Table 5.13 shows the composition of the CIGSeS absorber as measured by EDS. The data shows that the films are Cu-poor with the Cu/In+Ga ratio = 0.89 and the S/S+Se ratio was 0.30. Figure 5.44 shows the EDS spectra for the CIGSeS thin film absorber. The amount of sulfur has reduced as compared to the sample selenized at 450 ºC. The reduction in the amount of sulfur may be due to the improved extent of selenization.

Table 5.13: Chemical composition of CIGSeS thin films absorber.

Analyses	Atomic Percentage					Cu/In+Ga	S/(Se+S)
	Cu	In	Ga	Se	S		
EDS (@16 kV)	23.48	20.52	5.92	35.06	15.02	0.89	0.30

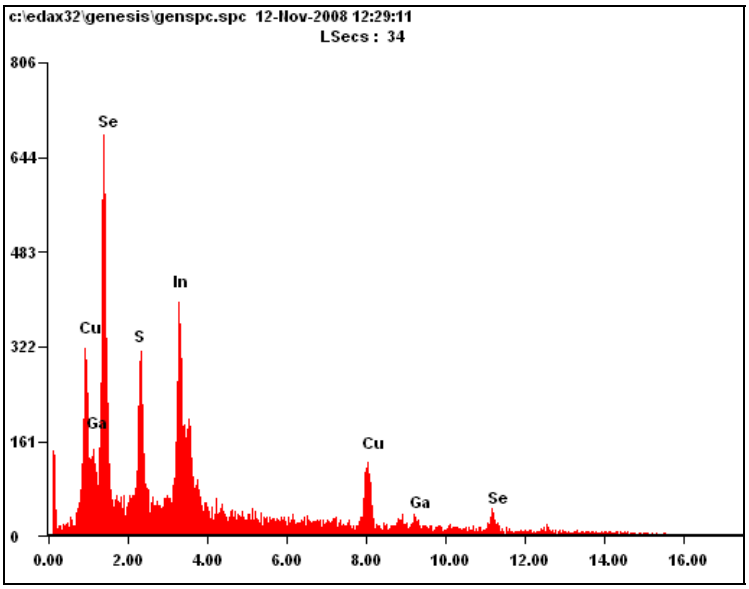

Figure 5.44: EDS spectra of the CIGSeS absorber selenized at 475 ºC for 35 minutes.

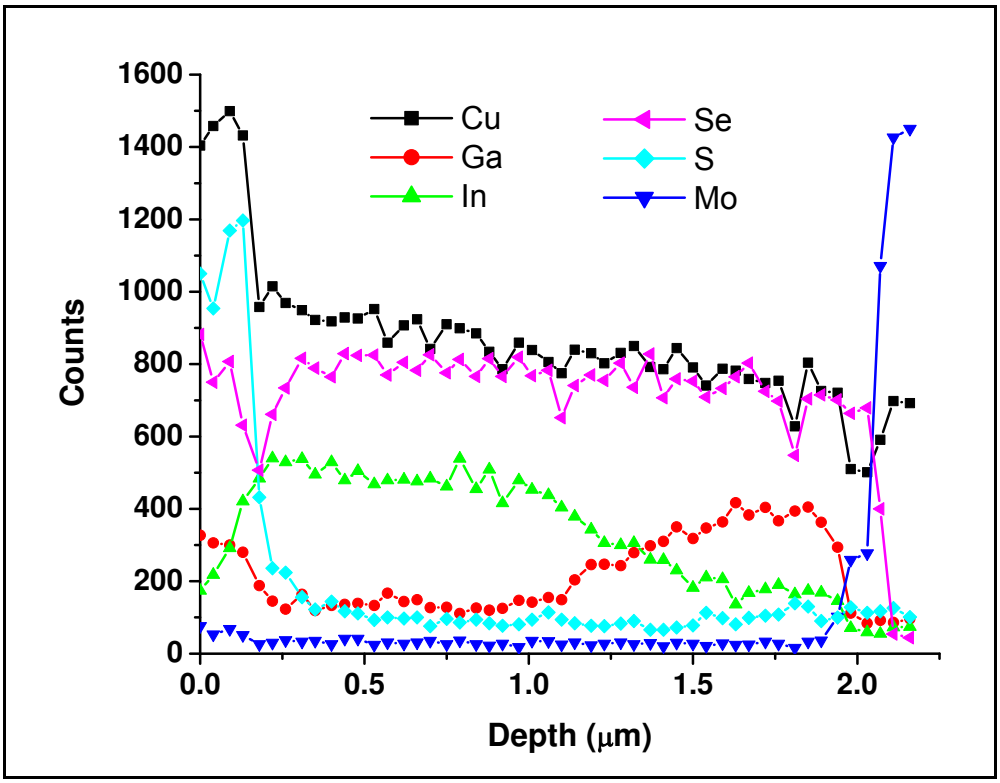

Figure 5.45: EDS lines scan of CIGSeS absorber selenized at 475 ºC.

Figure 5.45 shows the EDS depth profile analysis for the CIGSeS thin film absorber carried out during the TEM. The distribution of copper and selenium is reasonably uniform throughout the depth of the sample. The rise of the molybdenum signal at the back indicates the thickness of the sample, is ~2.1 μm. As expected the intensity of gallium signal starts to increase at a depth ~1.25 μm indicating the segregation of gallium towards the back contact and the intensity of indium signal reduces at approximately the same depth indicating that the gallium atoms have replaced the indium atoms in the lattice. The intensity of sulfur signal is higher at the surface upto 0.25 μm and reduces significantly in the bulk of the material. Figure 5.46 and

Figure 5.47 show the optical micrographs and the SEM image for the CIGSeS absorber. The SEM image indicates an increase in the grain size as compared to absorber selenized at 450 ºC. Figure 5.48 shows the cross sectional TEM image of the sample. As indicated by the TEM the sample has an undulating surface.

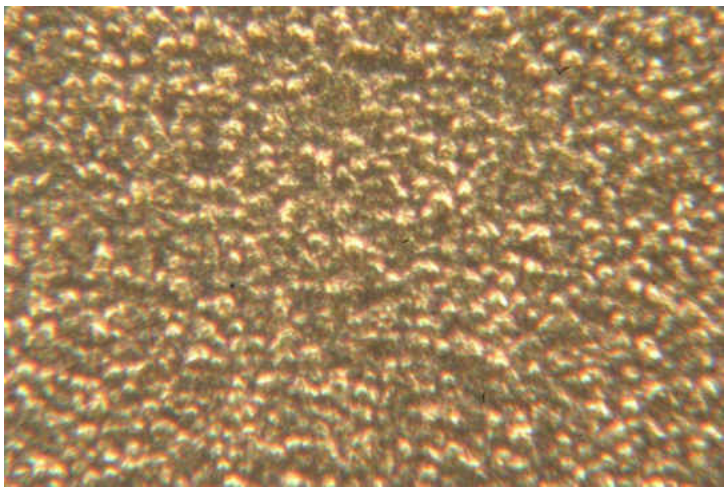

Figure 5.46: Optical Micrograph (x500) of CIGSeS selenized at 475 ºC

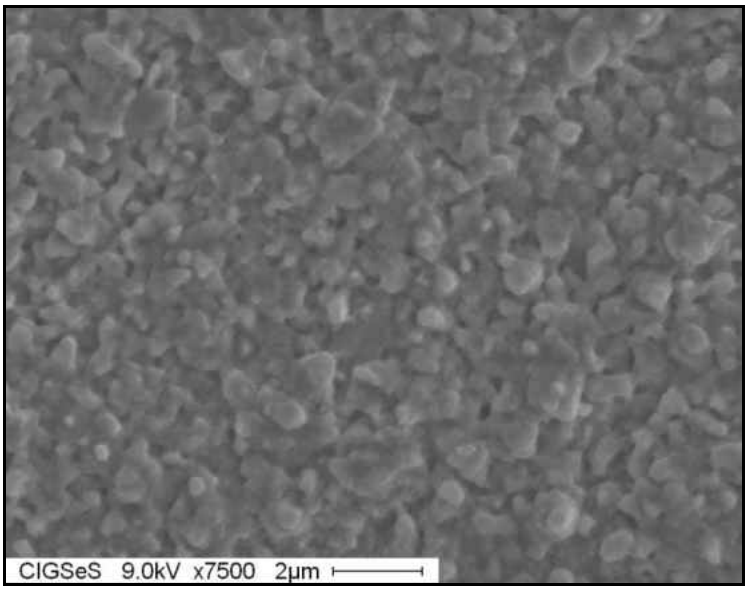

Figure 5.47: SEM image of CIGSeS absorber selenized at 475 ºC.

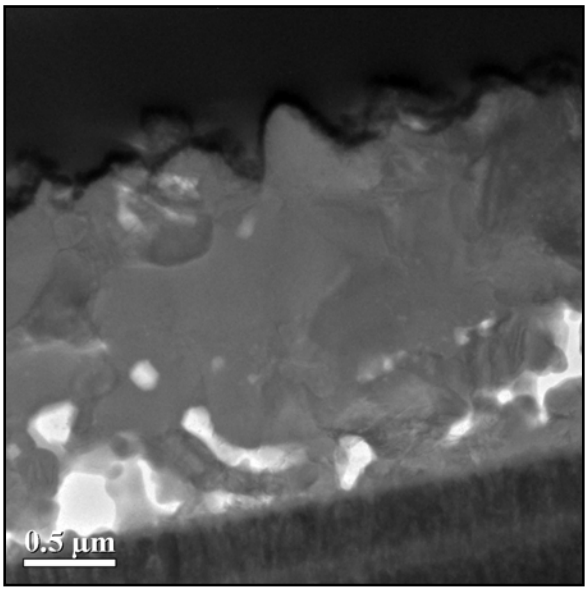

Figure 5.48: Cross sectional TEM image of CIGSeS absorber selenized at 475 ºC.

The current-voltage (I-V) measurements were carried out at FSEC. The cell parameters were as follows: V_{oc} = 280 mV, J_{sc} = 22.19 mA/cm^2, FF = 37.47 and an efficiency of 2.62 %. The series and shunt resistance were 15 Ω-cm^2 and 119 Ω-cm^2. A slight increase in each of the factors can be observed as compared to the sample selenized at 450 ºC. From the above analyses

it can be concluded that the increase in selenization temperature did improve the device performance. However, it is still necessary to further enhance selenization of the absorber. Hence, the selenization temperature was increased to 500 ºC for the next experiments

Experiment: Selenization Temperature - 500 ºC and Time - 25 Minutes

Selenization/ sulfurization experiment was carried out using the same precursor from the previous experiment. The temperature and time for selenization was 500 ºC and 25 minutes. The parameters used sulfurization and annealing were kept constant. Sulfurization was carried out at 525 ºC for 5 minutes and later annealed in nitrogen ambient for 30 minutes at 550 ºC. The cells were completed by depositing ~ 50 nm CdS heterojunction partner layer followed by 50 nm *i*:ZnO, 500 nm thick ZnO:Al and finally a Cr/Ag front contacts.

The composition of the film was studied using EPMA and EDS. The EDS depth profile was carried out during TEM analyses to study the distribution of elements. XRD analyses was carried out study the phases and also to calculate the lattice parameters. SEM and TEM were used to analyze the microstructure of the film. Finally I-V and QE measurements were carries to analyze the PV properties.

Table 5.14 show as the chemical composition of the CIGSeS absorber measured by EPMA and EDS. The EPMA analyses indicate that the film is Cu-poor with the Cu/In+Ga ratio = 0.91 and the S/S+Se ratio = 0.32. The EDS data also indicates approximately similar ratios, Figure 5.49 shows the EDS spectra for the CIGSeS absorber.

Table 5.14: Chemical composition of CIGSeS thin film.

Analyses	Atomic Percentage					Cu/In+Ga	S/(Se+S)
	Cu	In	Ga	Se	S		
EPMA (@20 kV)	24.77	19.39	7.66	32.63	15.56	0.91	0.32
EDS (@16 kV)	23.32	17.03	7.78	35.77	16.11	0.93	0.31

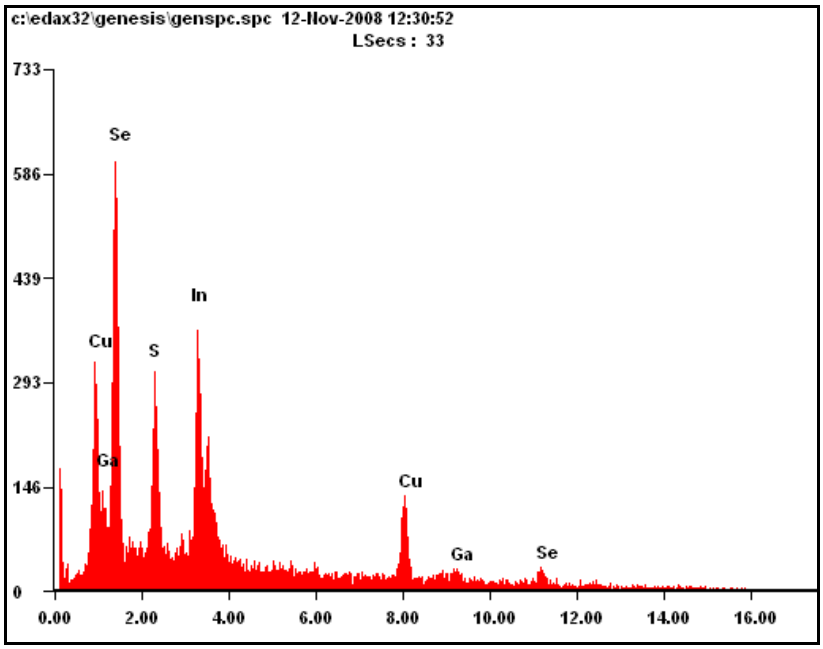

Figure 5.49: EDS spectra of CIGSeS thin film

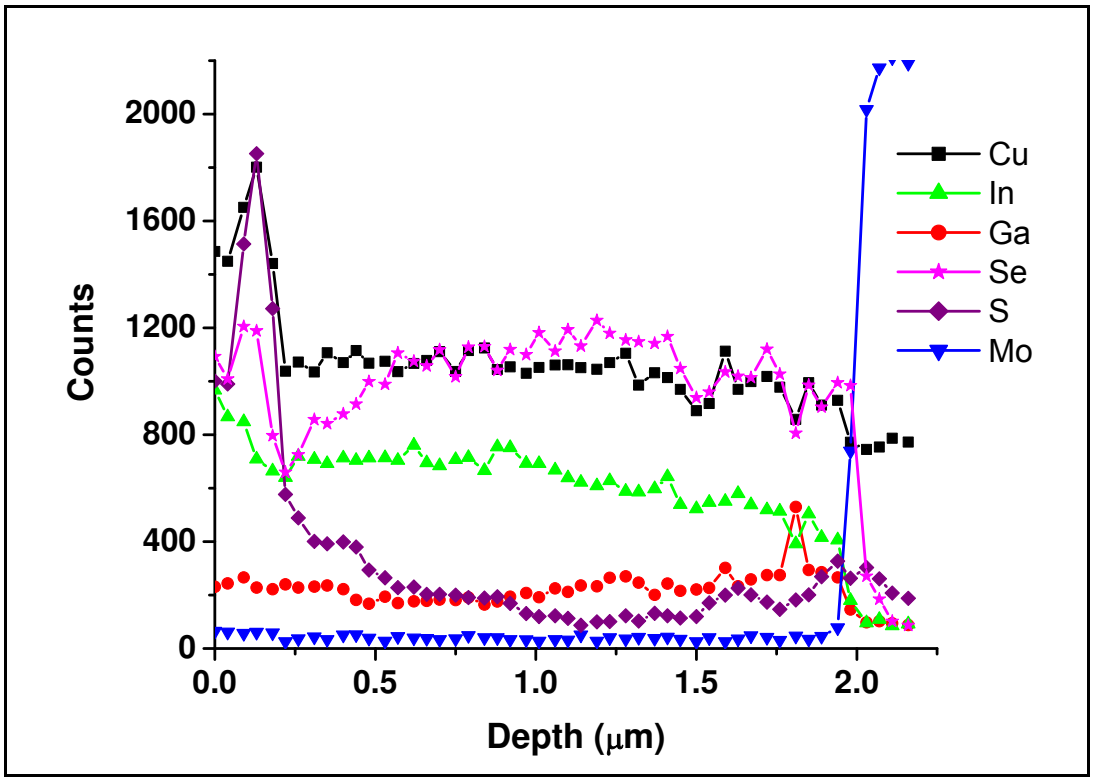

Figure 5.50: EDS line scan along the depth of the CIGSeS Thin Film

Figure 5.50 shows the EDS line scan along depth of the CIGSeS absorber. The EDS line scan analyses was carried out during TEM analyses. The EDS line scan shows that the distribution of copper and selenium is uniform throughout the bulk of the absorber. The scan indicates the presence of sulfur at the surface (~0.25 μm) and slightly increases near the back. The intensity of gallium is uniform throughout the bulk as compared to the sample selenized at 475 ºC.

Figure 5.51 shows the XRD spectra for the CIGSeS thin films solar cell with all the major reflections. The molybdenum reflection was observed at 2θ = 40.48°. The strongest reflection was from (112) plane at 2θ = 27.26 °. The lattice parameters calculated using the XRD data were a_0 = 5.658 Å and c_0 = 11.348 Å. The lattice parameters obtained from the XRD data match with the calculated lattice parameters of the $Cu(In_{0.8}Ga_{0.2})(Se_{2-y}S_y)$ phase. However, the

EPMA data indicates the formation of $Cu(In_{0.72}Ga_{0.28})(Se_{0.68}S_{0.32})_2$ phase. The composition obtained from XRD is a rough estimate of the compound.

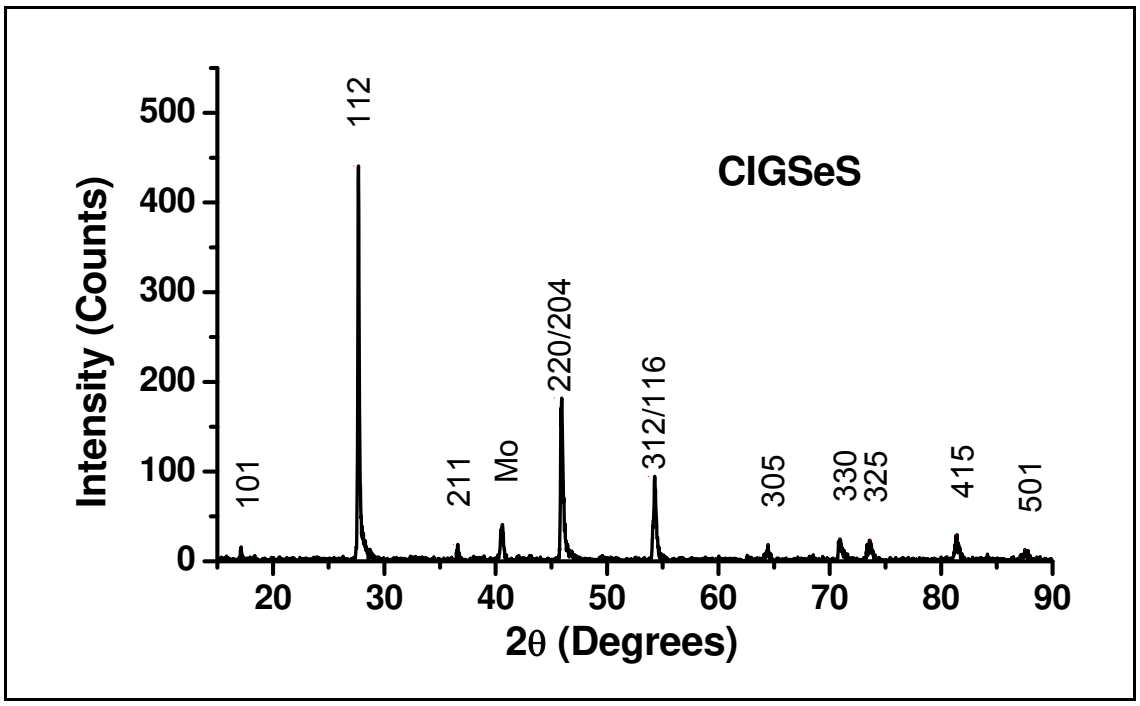

Figure 5.51: XRD pattern of CIGSeS thin film

Figure 5.53 shows the SEM image of the CIGSeS thin film absorber selenized at 500 ºC. The grains are larger than those in sample selenized at 450 ºC and 475 ºC. This indicates that increase in the selenization temperature improved the surface morphology. The grains are compactly packed and the surface is smooth. The average grain size was ~0.5 μm. Figure 5.54 shows the cross sectional TEM image for the CIGSeS thin film selenized at 500 ºC. The TEM image indicates a less undulating surface as compared to the sample selenized at 475 ºC

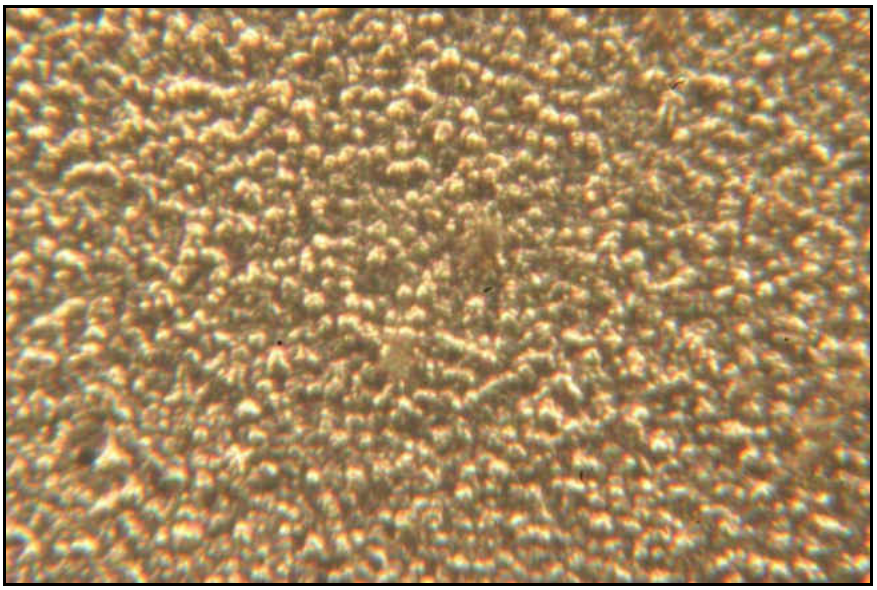

Figure 5.52: Optical Micrograph (x500) of CIGSeS thin film.

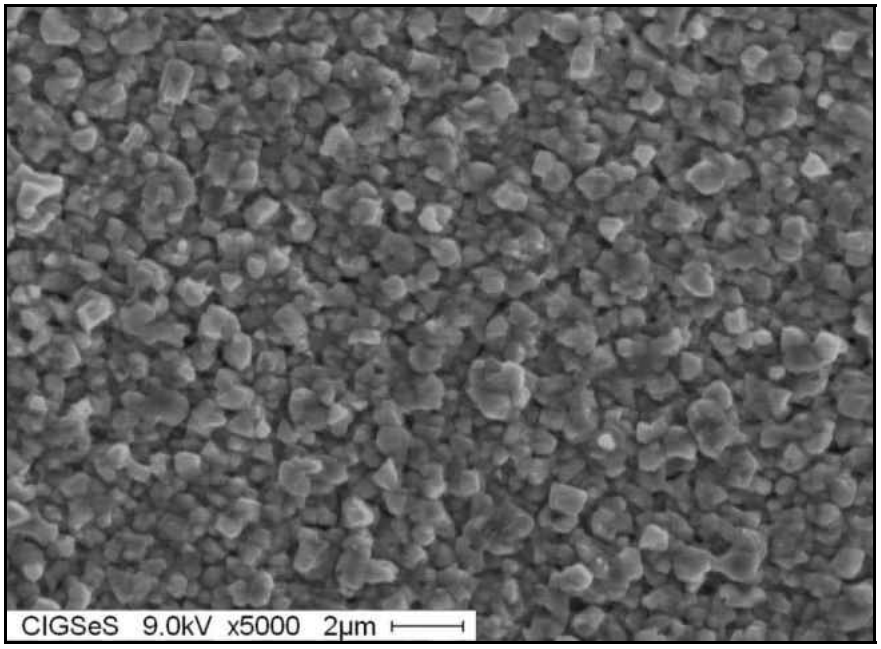

Figure 5.53: SEM of CIGSeS thin film

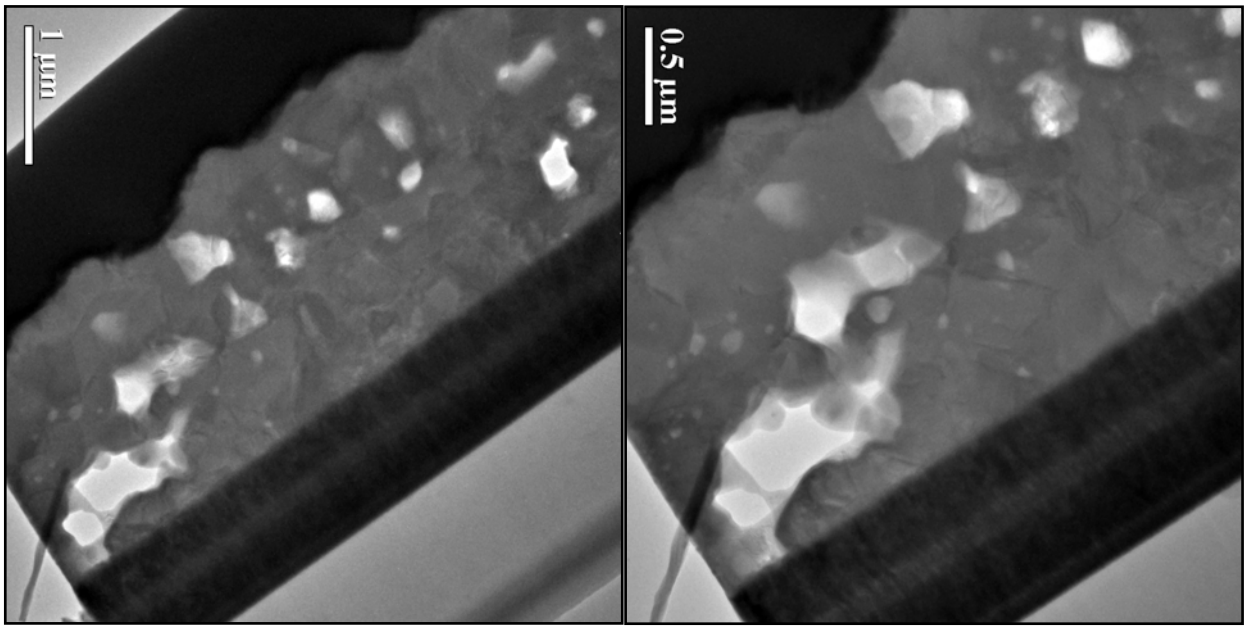

Figure 5.54: Bright field TEM image of CIGSeS thin film.

Current-voltage (I-V) measurement was carried out at FSEC. The cells showed better performance as compared to the earlier cells. The cell parameters were: V_{oc} = 460 mV, J_{sc} = 21.54 mA/cm^2, FF = 52.7% and η = 5.22%. The sample was sent to National Renewable Energy Laboratory (NREL) for I-V and QE measurements. Figure 5.55 and

Figure 5.56 show the I-V and QE curve measured at NREL. The official confirmed cell efficiency measured at NREL is 9.95%. The efficiency of the sample measured at NREL almost doubled as compared to the efficiency measured at FSEC. The detailed photovoltaic parameters are provided in Table 5.15. The series and shunt resistance were 6 Ω-cm^2 and 809 Ω-cm^2 respectively. There is significant increase in the shunt resistance as compared to the cell measured from the sample selenized at 450 ºC. Hence, this suggests that the quality of the bulk of the absorber has improved and also the surface appears to be smoother. It can also be concluded that the selenization temperature of 450 ºC and 475 ºC are not sufficient to prepare

device quality absorber. Moreover, the QE curve shows reasonably good response with lower loss of low-energy photons due to recombination in bulk.

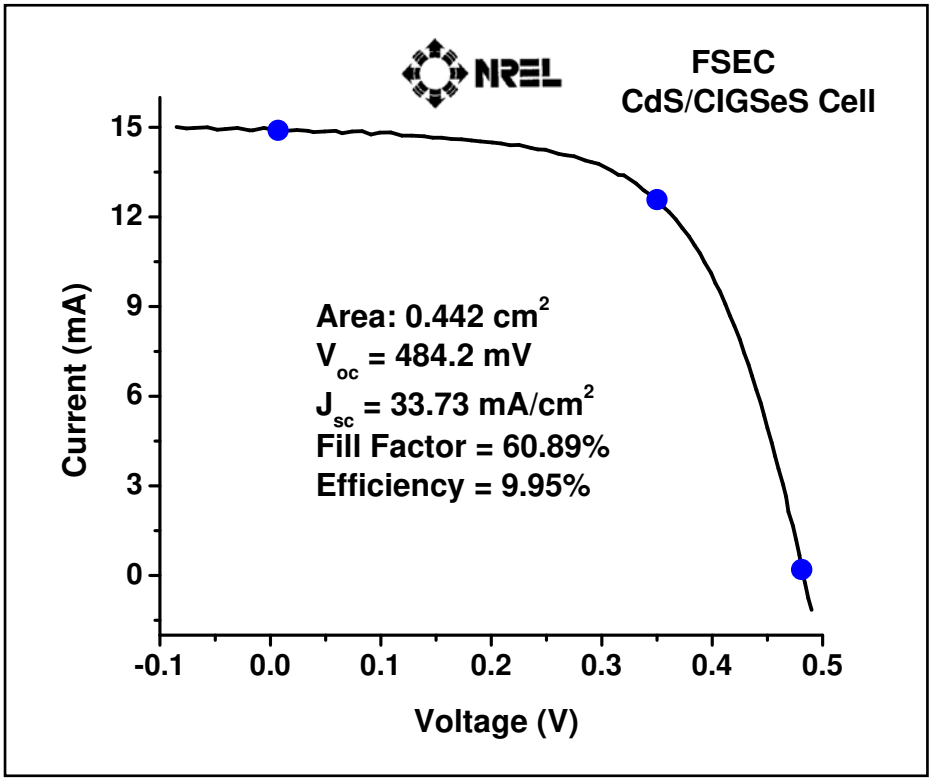

Figure 5.55: Current-voltage characteristics of CIGSeS thin film solar cell

Table 5.15: CIGSeS/CdS solar cell PV parameters

Area	0.442 cm^2
Open Circuit Voltage (V_{oc})	484.2 mV
Short Circuit Current (I_{sc})	14.909 mA
Short Circuit Current Density (J_{sc})	33.73 mA/cm^2
Peak Voltage (V_{max})	353.7 mV
Peak Current (I_{max})	12.426 mA
Fill Factor (FF)	60.89 %
Efficiency (η)	9.95 %

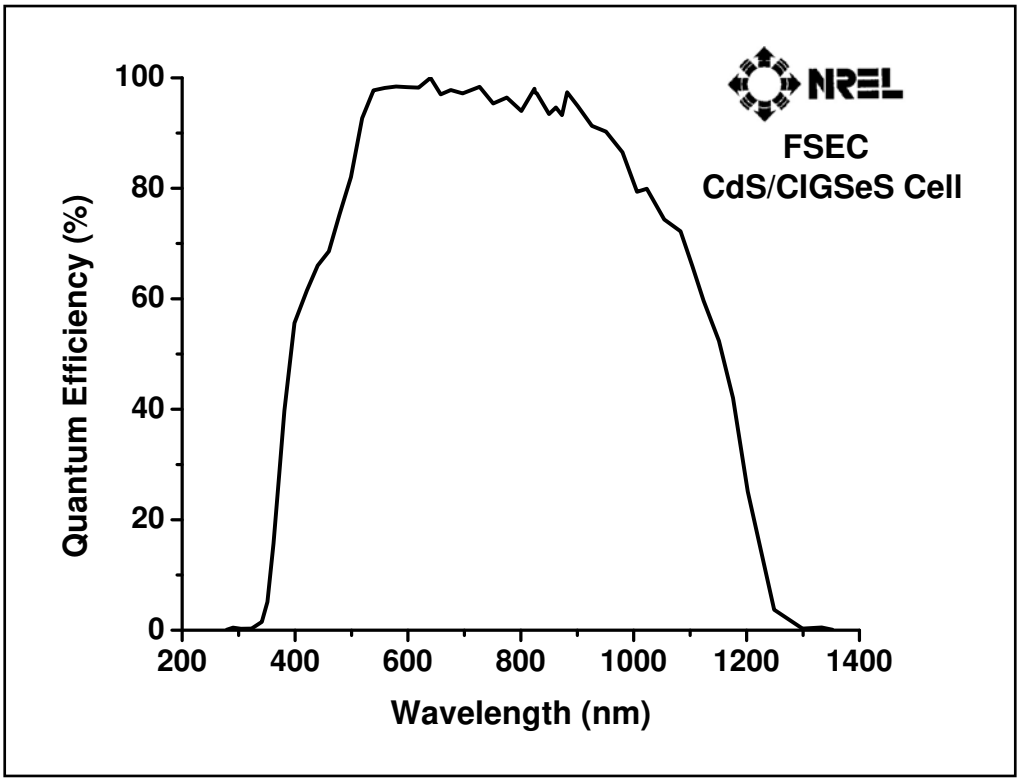

Figure 5.56: Quantum efficiency characteristics of CIGSeS thin film solar cell.

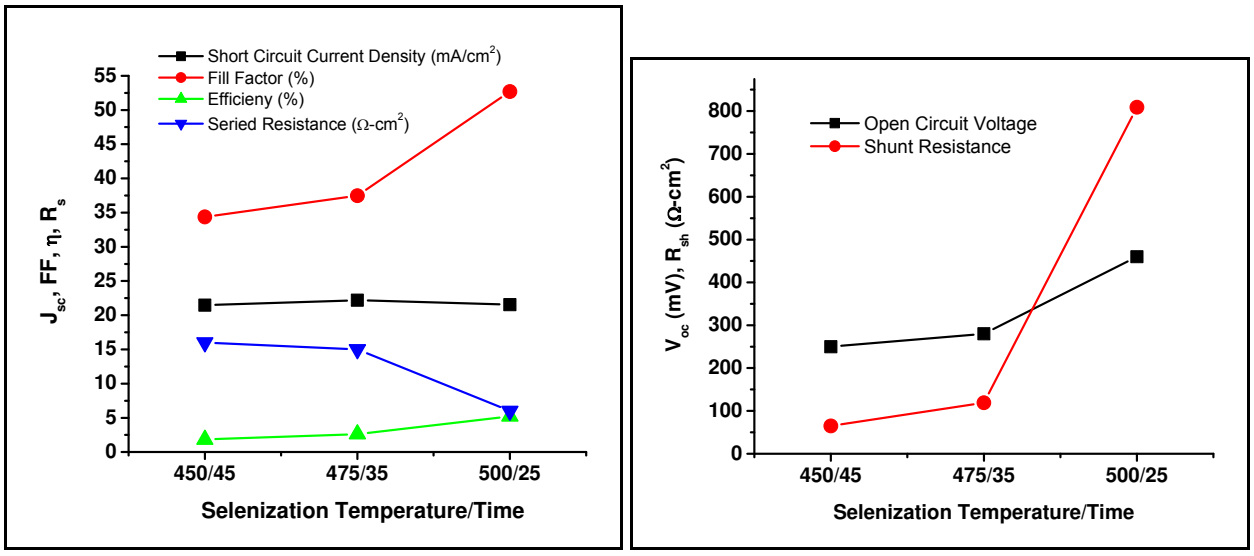

Figure 5.57: Comparison of PV parameters of CIGSeS thin film solar cells measured at FSEC.

The variations of the PV parameters for the three different CIGSeS thin film solar cells are shown in Figure 5.57. As can bee seen in the figure there is progressive drop in series resistance and a progressive increase in the open circuit voltage, shunt resistance, fill factor and the efficiency with an increase in the selenization temperature. It can be seen that the selenization temperature has no effect on the short circuit current. No change in the short circuit current indicates that the number of electron-hole pairs generated in each of the representative cell were same thus suggesting that the bandgap of the absorber in each of the completed cell was approximately same. Therefore, the increase in the open circuit voltage cannot be due to the bandgap variation. Based on the TEM micrographs of the three absorbers [Figure 5.43 (Selenized at 450 ºC), Figure 5.48 (Selenized at 475 ºC), and Figure 5.54 (Selenized at 500 ºC)] it can be said that the surface morphology of the absorber improved as the selenization temperature was increased. The improved surface morphology results in smoother absorber films that subsequently result in reduction in the interfacial recombination. Reduced interfacial recombination is probably due to reduction of shunt paths resulting in lower reverse saturation current and consequently higher open circuit voltage. The reduced recombination will also result in higher shunt resistance and consequently a higher fill factor. The SEM micrographs [Figure 5.42 (Selenized at 450 ºC), Figure 5.47 (Selenized at 475 ºC), and Figure 5.53 (Selenized at 500 ºC)] of the absorbers also indicate an increase in the grain size of the absorber as well as improved morphology of the film. Moreover, as the selenization temperature increased the degree of selenization thus improving the CIGS phase formation and reduction compensating Se vacancies in the bulk of the film. This resulted in higher p-type doping concentration and consequently the reduction in the bulk resistance of the absorber causing the reduction in the series resistance of the device. Fill factor is directly dependant on the shunt resistance and

inversely proportional to the series resistance. Hence, as the selenization temperature was increased there was a corresponding increase in the fill factor. Thus, the increase in PV conversion efficiency with increase in the selenization temperature can be attributed to higher open circuit voltage and higher fill factor that are direct result of improved surface morphology and improved degree of selenization consequently improving the CIGS matrix in the bulk of the film.

5.7. EBSD Analyses of CIGSeS Thin Films

Electron backscatter diffraction (EBSD) in scanning electron microscopy (SEM) is a powerful technique which allows crystallographic information such as the grain orientation, grain boundaries and also the grain size to be obtained. In a SEM, the electron beam generates various types of signals such as secondary electrons, X-rays and back scattered electrons. The EBSD technique is based on the diffraction of back scattered electrons at the crystalline planes. This generates orientation maps of the region in the vicinity of the sample surface. The scattered electrons travel in all directions (mainly forward). The diffracted electrons appear in form cones rather than well defined beams. These cones are termed as Kossel cones. However, the screen is flat and nearly normal to the incident beam, these cones appear as parabolas. The parabolas look like parallel line on a fluorescent screen in the area close to the optic axis. These lines are termed as the *Kikuchi* lines. Kikuchi pattern consists of sets of two mutually parallel Kikuchi lines. The Kikuchi lines with higher scattering angles to the incident beam are brighter than the background whereas the lines with smaller angle are less intense than the diffuse background. The distance between the parallel lines corresponds to the total scattering angle 2θ. The Kikuchi pattern is characteristic of the crystal structure and orientation of the sample region from which it was

generated. The crystal orientation at each point is determined when the beam is scanned across a polycrystalline sample. The resulting map will reveal the constituent grain boundaries, morphology and orientations. A comprehensive and quantitative representation of the microstructure of a sample can be established with EBSD.

The important characteristics of EBSD are:

1) The depth from which the diffracted electrons come from.

2) The angle between the sample surface and the electron beam.

The formation of Kikuchi patterns is due to the electrons that did not interact with sample after being diffracted. The EBSD technique analyzes the material few tens of nanometers beneath the surface because all the patterns generated are by the electrons coming from the top layer. The sample material at the surface has to be reasonably crystalline, defect free and flat. The intensity of the patterns increase with the decrease in the angle of incidence of the beam on the sample surface. However, to obtain good Kikuchi patterns the sample tilt angle is set at 70º from the horizontal. This inclination causes shadowing effect on samples with a rough surface (R_a > 100 nm) due to the presence of surface features. Hence, the diffracted electrons cannot reach the detector. To avoid the problem of shadowing, the surface of the sample needs to be polished carefully providing a mirror-finish.

Mechanical polishing or ion milling technique can be employed to polish the surface. However, this depends on the surface roughness of the sample. Surface polishing using Ion milling is simple technique. The CIGSeS thin film absorbers prepared by two stage process were not completely flat. Different combinations of voltages (5 kV and 5.5 kV) and beam angles (1º, 5º, 9º and 15 º) were used for polishing the sample surface by ion milling. Some of the samples were polished for significant duration up to 3 hours. Some of the samples appeared to have

smoother surface. Two of the best polished samples were sent for EBSD analysis to NREL. Figure 5.58 shows the SEM image of the ion milled surface. The structure of the grains should not be visible for EBSD analyses. However, it can be observed from the image that the structure of the grains is visible and the film is flat enough for EBSD analyses. Therefore, for this sample the Kikuchi patterns were not good.

New set of CIGSeS samples were prepared for EBSD analyses. The process of polishing the sample by ion milling did not result in adequately smooth surfaces for EBSD. Hence, it was decided to carry out mechanical polishing of the surfaces. The samples were polished by hand on a dimpler with 0.05 μm alumina suspension. The samples were then etched with bromine/methanol for two seconds. Several areas of the samples were again polished for 10 – 30 seconds. Most of polished area produced good Kikuchi patterns (Figure 5.59). The indexing of the sample was poor. This is because of the departure of the crystalline structure of the films from the $CuInSe_2$ structure.

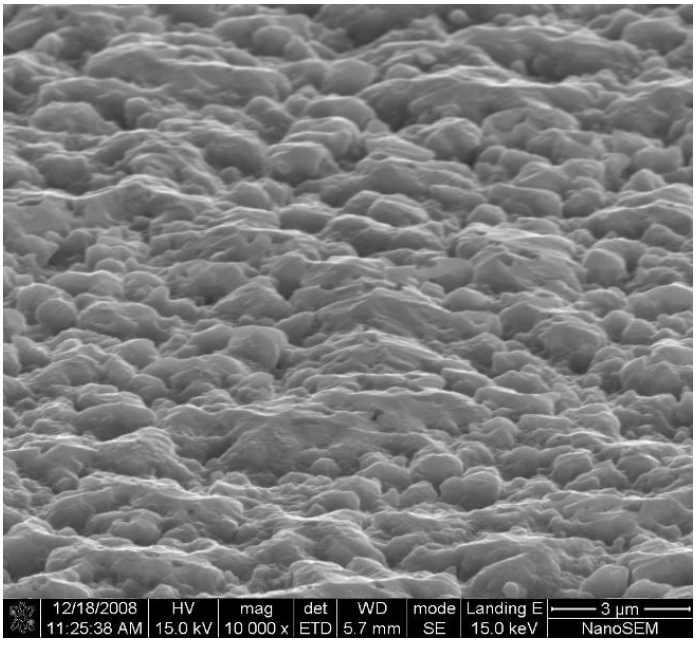

Figure 5.58: SEM image of Ion milled CIGSeS thin film surface.

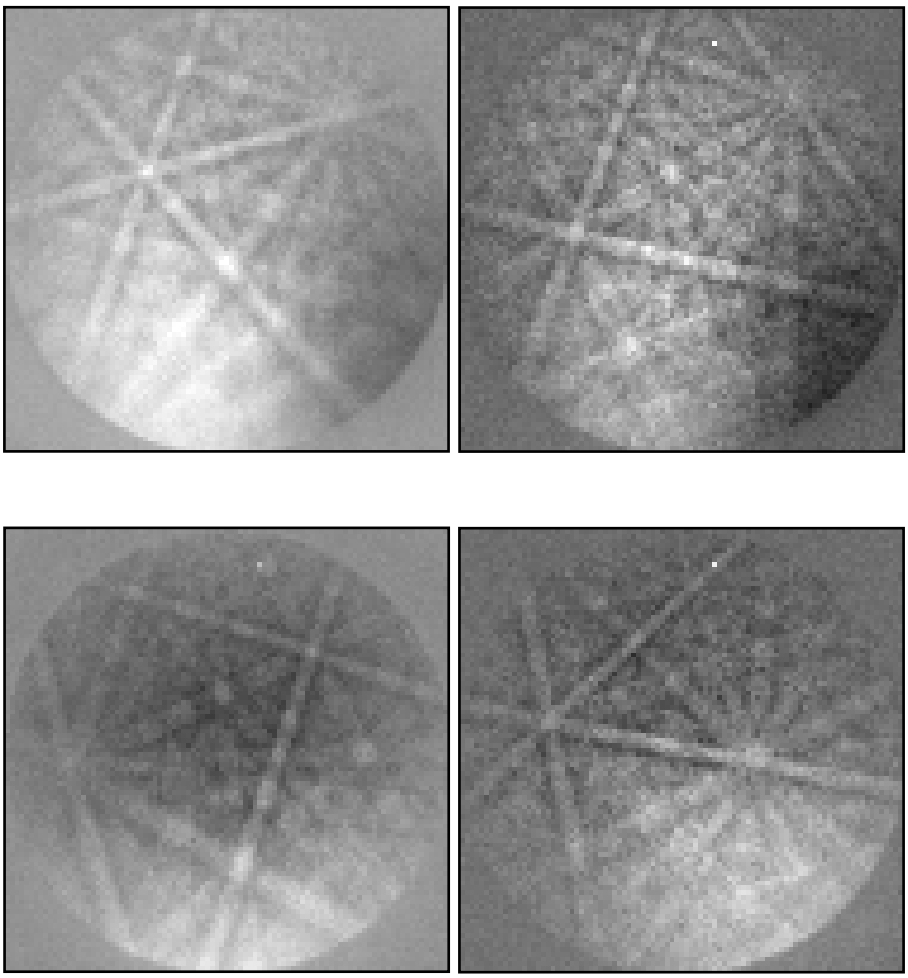

Figure 5.59: Kikuchi patterns form different grains of CIGSeS thin film absorber

Figure 5.60 shows the EBSD maps for the CIGSeS samples. Grains with various orientations can be clearly observed. However, it can also be observed that some pixels have not been indexed by the software. This might be due to the departure of crystalline structure of the film from $CuInSe_2$ as well as due to the presence of amorphous phases. It may be noted that EBSD analysis is being carried out on CIGSeS absorber for the first time. Lattice spacings and position of atoms with various combinations of Ga/In+Ga and S/Se+S in CIGSeS have not yet been recorded. Hence, it was not possible for the software to determine the various phases and

grain orientations in the film. In the future, the lattice parameters and the position of the atoms would become available and usable for indexing the various grains in CIGSeS absorber.

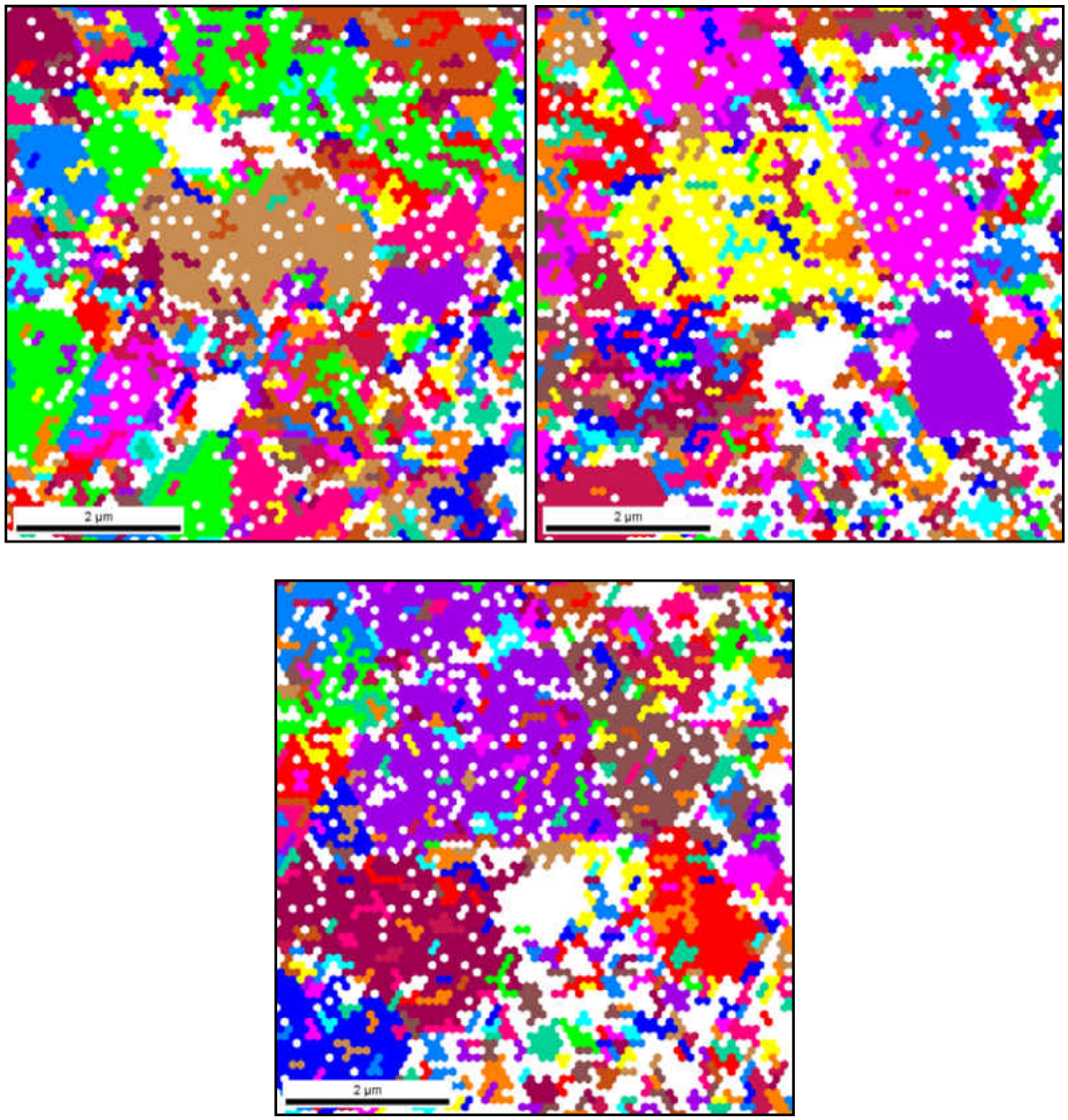

Figure 5.60: EBSD Orientation Maps for CIGSeS thin film

Manual procedure for identification of the planes:

Figure 5.61(a) represents the schematic drawing of 3-pairs of Kikuchi lines in a typical Kikuchi pattern. Each band has a pair of lines: an excess line shown as solid lines and a deficit line shown

as dashed lines. The dotted line is drawn symmetrically between the pairs of Kikuchi lines for the sake of measuring the angles α_i. The bands in a diffraction patterns represent planes in the crystal. The widths of the bands or distances between the parallel lines (w_1, w_2 and w_3) which correspond to the total scattering angle 2θ are inversely proportional to the *d*-spacing of the corresponding crystallographic planes through the Bragg's Law given by,

$$\lambda = 2d_{hkl} \sin\theta$$

λ = Wavelength of the incident radiation determined by e-beam accelerating voltage

d_{hkl} = d-spacing of the reflecting plane.

2θ = Angle between the bands, equal to the width.

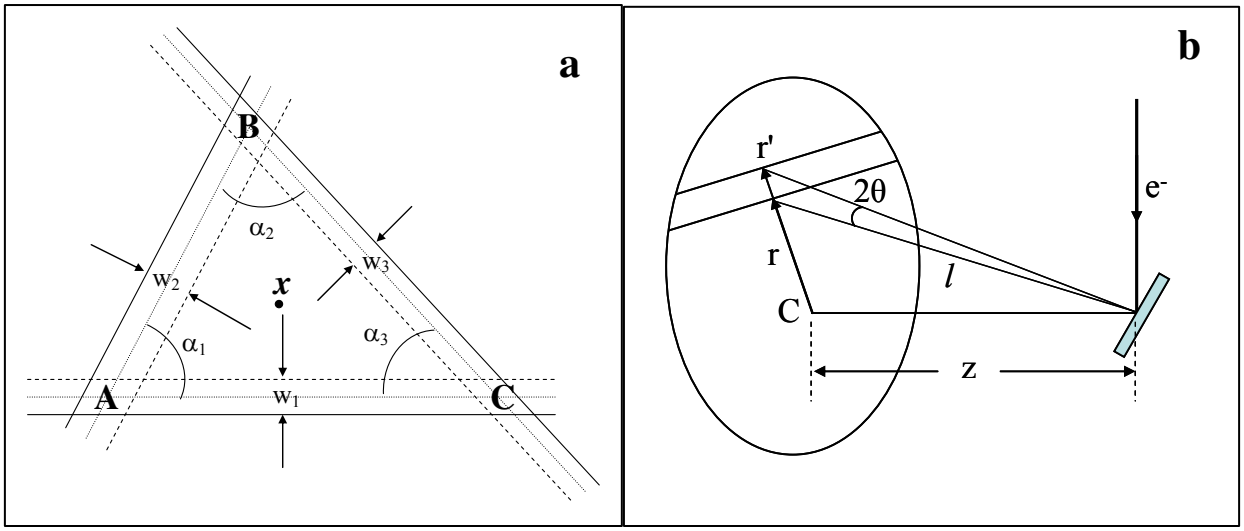

Figure 5.61: a) Three Kikuchi line pairs. *x*: Direction of incident beam, α_i: Angle between two non parallel Kikuchi line pair. b) Diagram showing the band width relation (C: Pattern Center)

The width of the pair of Kikuchi lines is a function of the geometry of the system. (Figure 1b)

For small angles, $\sin\theta \sim \tan\theta \sim \frac{1}{2}\tan 2\theta$

From geometry of figure 1b,

$\tan 2\theta = \frac{r'-r}{l} = \frac{w}{l}$, where, l = camera length, characteristics of the optics of the microscope and w = width of the band

Therefore, substituting values of tan 2θ into the above equation and then into the Bragg's law:

$$2d_{hkl}\frac{1}{2}\frac{w}{l} = \lambda$$

$$\lambda l = wd_{hkl}$$

The values of d-spacing derived from bands are then compared with the theoretical d-spacing values and the angles α_i between them to find the corresponding reflecting plane.

6. Summary and Conclusions

CIGSeS thin film solar cell with an efficiency of 13.73% was prepared at FSEC PV Material Lab. However, there was not a complete understanding of some the effects that were observed during the preparation of this device. Hence, one of the primary goals of this research was to carry out a detailed study to elucidate the effect of process parameters on material properties of the absorber film and attempt to correlate it with device performance. Even though the positive effect of sodium on device performance was observed from earlier research, there was no clear understanding of the mechanism for this beneficial effect. The knowledge of this mechanism is necessary to further improve the device performance. For this reason, efforts were carried out to study the effect of sodium on the morphology and structure of the CIGSe and CIGSeS thin films. The degree of (112) orientation for all the samples of CIGSe and CIGSeS showed progressive increase with the amount of sodium supplied. The presence of sodium during the absorber preparation leads to the increase in the grain size for both CIGSe and CIGSeS thin films. The AFM analyses also confirmed that the surface roughness of the films decreased with increase in the amount of sodium. The surface roughness value for sample with no NaF was 310 nm and for the sample with 80 Å NaF was 160nm. The amount of sulfur in the CIGSeS thin film decreased with increase in the amount of sodium.

As mentioned earlier sodium is known to have beneficial effect on device performance and this becomes an added advantage as conventionally used substrate, sodalime glass, tends to diffuse sodium into the absorber. However, this sodium diffusion is uneven and uncontrollable affecting the yield of absorber preparation. The proposed solution for this issue is the deposition of a barrier layer with sodium precursor as source of sodium. Silicon nitride was the choice of barrier layer and efforts were carried out to deposit the desired thickness of barrier layer. The

process parameters for depositing the Silicon nitride alkali barrier layer were optimized. Deposition structure of molybdenum back contact layer was modified. The molybdenum layers were deposited with alternate tensile and compressive molybdenum layers were deposited so as to nullify the net residual stress. The first molybdenum layer deposited on the sodalime glass substrate was the tensile in nature. This layer has a rough surface and hence adheres well with the substrate. The top layer in the stacking is compressive in nature. These layers have smoother surface required for the absorber growth.

The higher efficiency CIGSeS thin film solar cell was prepared using DESe as the selenium precursor during the selenization of the precursor. However, the sudden non-availability of DESe forced the use of DMSe as an alterative selenium source. The experiments using DMSe were started without much hope. However, DMSe has been successfully used to prepare CIGSe and CIGSeS thin film solar cells. CIGSe thin film solar cells with an efficiency of 6.52% were fabricated. The films were selenized at temperature: 550 ºC and time: 60 minutes. This resulted in a ~0.1μm thick $MoSe_2$ layer which leads to the increase in the series resistance. The process parameters used for selenization were excessive. Selenization/sulfurization process parameters have been optimized using DMSe as selenium source. CIGSeS thin films were prepared with a PV Conversion efficiency of 9.95%. The thickness of the absorber layer has also been reduced to ~2 μm. Further process optimization can help to improve the efficiency of the cell. This research demonstrated the potential of using ***Dimethyl Selenide*** as a selenium precursor for preparation CIGSeS thin-film solar cells by an easily scalable technique. The process parameters for the deposition of CdS heterojunction layer and the ZnO transparent conducting oxide were also optimized.

Electron backscattered diffraction technique was used for first time to analyze the CIGSeS thin film absorbers. Mechanical polishing of the absorber resulted in a better surface as compared to the ion milled surface for EBSD analyses. Kikuchi patterns and EBSD maps were obtained on the polished samples. However, some of pixels were not indexed by the software. This might be due to the departure of crystalline structure of the film from $CuInSe_2$ as well as due to the presence of amorphous phases. Since EBSD analysis is being carried out on CIGSeS absorber for the first time. Lattice spacings and position of atoms with various combinations of Ga/In+Ga and S/Se+S in CIGSeS have not yet been recorded. However, with the help of the lattice parameters and the position of the atoms in the base the data file can be created for CIGSeS material.

Future Work:

The study of the effects of sodium was carried out on the basis of the absorber morphology and structure. It would be interesting to study the effects of sodium on the PV parameters of the solar cells prepared by selenization / sulfurization process using organometallic compound as the selenium precursor. The formation of $MoSe_2$ interfacial layers depends on the process parameters. Sodium is reported to influence formation of $MoSe_2$ during the selenization process. The present study did not indicate a correlation between the amount of sodium and the extent of $MoSe_2$ formation. It would therefore, be interesting to continue the study on the effects of sodium on the $MoSe_2$ layer formation.

The samples were annealed at 550 ºC for 30 minutes after the selenization/sulfurization process. The annealing step can enhance elemental interdiffusion and homogenization of the absorber and would also promote recrystallization of the absorber. Moreover, in this study, the

sulfurization parameters were kept constant. Therefore it is recommended that this study should be extended by varying the sulfurization and annealing time and temperature profiles with an aim to improve the efficiency of the solar cell.

The contribution made through efforts carried out in this research as follows:

1. The correlation between the amount incorporated sodium and device performance was explained based on the effect of sodium on the absorber morphology and structure.
2. CIGSeS thin film solar cell with an efficiency of 9.95% was prepared using of dimethyl selenide as an alternative selenium precursor. A thin film deposition technique preparing solar cell with an efficiency of ~10% can considered as a plausible process choice for high volume production. Hence it was successfully demonstrated the use of dimethyl selenide as an alternative selenium precursor for a two stage process.
3. EBSD characterization technique was introduced for the in-depth analyses of CIGSeS thin films. However, due to the non-existence of data file in the present available software it was difficult to analyze the patterns and maps. Data files can be created for CIGSeS material with the help of the lattice parameters and the position of the atoms in the base.

APPENDIX A: Degree of Preferred Orientation Calculation

The intensities of all the CIGSe or CIGSeS reflections were determined by integrating the areas below the peaks. The ratio of the each intensity with respect to the total area of intensities of all the peaks was calculated. The integrated intensities of the XRD data of a randomly prepared (usually a powder) sample are usually considered to estimate the degree of preferred orientation. The JCPDS data is from a randomly prepared sample. Hence the JCPDS data was used for the comparison to calculate the degree of preferred orientation. The estimates of the degrees of preferred orientation for all the peaks are provided below. As can be seen the error in the calculations become large when the peaks such as 211 and 336 are very weak. Therefore, only the most intense peaks (112, 220/204 and 116/312) are considered in these estimates.

Degree of preferred orientation calculations for CIGSe thin film absorber without NaF

Peak	**JCPDS**		**No NaF**			**Degree of Preferred Orientation**
	Intensity	$\frac{Peak\ Area}{\sum Peak\ Areas}$	**Area**	**2θ**	$\frac{Peak\ Area}{\sum Peak\ Areas}$	
101	7	0.025	55	17.14	0.022	0.849
112	100	0.364	885	26.68	0.348	0.958
211	2	0.007	91	35.62	0.036	4.948
220/204	80	0.291	551	44.28	0.217	0.746
312/116	50	0.182	305	52.50	0.120	0.660
400/008	8	0.029	141	64.40	0.056	1.911
316/332	10	0.036	148	71.06	0.058	1.598
228	12	0.044	156	81.48	0.061	1.404
336	6	0.022	209	87.44	0.082	3.774

Degree of preferred orientation calculations for CIGSe thin film absorber with 40 Å NaF

Peak	JCPDS		40 Å NaF			Degree of Preferred Orientation
	Intensity	$\frac{Peak\ Area}{\sum Peak\ Areas}$	Area	2θ	$\frac{Peak\ Area}{\sum Peak\ Areas}$	
101	7	0.025	59	17.16	0.022	0.853
112	100	0.364	1018	26.66	0.375	1.032
211	2	0.007	95	35.58	0.035	4.814
220/204	80	0.291	576	44.28	0.212	0.730
312/116	50	0.182	301	52.44	0.111	0.611
400/008	8	0.029	136	64.36	0.050	1.724
316/332	10	0.036	156	71.02	0.057	1.580
228	12	0.044	159	81.56	0.059	1.341
336	6	0.022	213	87.66	0.078	3.593

Degree of preferred orientation calculations for CIGSe thin film absorber with 80 Å NaF

Peak	JCPDS		80 NaF			Degree of Preferred Orientation
	Intensity	$\frac{Peak\ Area}{\sum Peak\ Areas}$	Area	2θ	$\frac{Peak\ Area}{\sum Peak\ Areas}$	
101	7	0.025	57	17.16	0.022	0.873
112	100	0.364	976	26.70	0.379	1.041
211	2	0.007	89	35.58	0.035	4.776
220/204	80	0.291	516	44.32	0.200	0.688
312/116	50	0.182	273	52.40	0.106	0.583
400/008	8	0.029	144	64.48	0.056	1.920
316/332	10	0.036	147	71.06	0.057	1.574
228	12	0.044	157	81.54	0.061	1.393
336	6	0.022	217	87.54	0.084	3.864

Degree of preferred orientation calculations for CIGSeS thin film absorber with 40 Å NaF

Peak	JCPDS		40 NaF			Degree of Preferred Orientation
	Intensity	$\frac{Peak\ Area}{\sum Peak\ Areas}$	Area	2θ	$\frac{Peak\ Area}{\sum Peak\ Areas}$	
101	7	0.025	718	17.22	0.1311	4.815
112	100	0.364	2402	27.10	0.4384	1.127
211	2	0.007	216	36.14	0.0393	5.055
204/220	80	0.291	320	45.00	0.0584	0.187
116/312	50	0.182	961	53.46	0.1754	0.902
008/400	8	0.029	577	65.92	0.1053	3.383
316/332	10	0.036	285	72.50	0.0520	1.337

Degree of preferred orientation calculations for CIGSeS thin film absorber with 80 Å NaF

Peak	JCPDS		80 NaF			Degree of Preferred Orientation
	Intensity	$\frac{Peak\ Area}{\sum Peak\ Areas}$	Area	2θ	$\frac{Peak\ Area}{\sum Peak\ Areas}$	
101	7	0.025	585	17.32	0.0691	2.538
112	100	0.364	3730	26.9	0.4408	1.133
211	2	0.007	331	35.9	0.0391	5.030
204/220	80	0.291	512	44.8	0.0606	0.195
116/312	50	0.182	1768	52.98	0.2089	1.074
008/400	8	0.029	1054	65.24	0.1246	4.003
316/332	10	0.036	481	71.84	0.0568	1.461

Degree of preferred orientation calculations for CIGSeS thin film absorber with 120 Å NaF

Peak	JCPDS		120 NaF			Degree of Preferred Orientation
	Intensity	$\frac{Peak\ Area}{\sum Peak\ Areas}$	Area	2θ	$\frac{Peak\ Area}{\sum Peak\ Areas}$	
101	7	0.025	737	17.3	0.0796	2.923
112	100	0.364	4163	26.96	0.4497	1.156
211	2	0.007	401	36.02	0.0433	5.566
204/220	80	0.291	550	44.92	0.0594	0.191
116/312	50	0.182	1815	53.26	0.1961	1.008
008/400	8	0.029	1087	65.44	0.1175	3.774
316/332	10	0.036	503	72.06	0.0544	1.397

APPENDIX B: Lattice Parameter Calculations

Lattice parameter calculation for CIGSe and CIGSeS absorber:
Wavelength used for calculations:

$Cu_{K\alpha 1}$ = 1.540562 nm
$Cu_{K\alpha 2}$ = 1.544390 nm

$$Cu_{K\alpha} = \frac{2\,x\,Cu_{K\alpha_1} + Cu_{K\alpha_2}}{3}$$

$Cu_{K\alpha}$ = 1.541838 nm

From Bragg's law:

$$d_\alpha = \frac{\lambda}{2\,Sin\theta}$$

For the CIGSeS chalcopyrite α phase having a tetragonal structure,

$$d_\alpha = \frac{1}{\sqrt{\frac{h^2+k^2}{a^2} + \frac{l^2}{c^2}}} \quad \text{..... (1)}$$

Sample Calculations of a_0 and c_0 for ***Sample Id: C16***

For (220) peak,

$$d_\alpha = \frac{\lambda}{2\sin\theta} = \frac{1.541838}{2 * \sin\left(\frac{22.14 * \pi}{180}\right)} = 2.046 \text{ Å}$$

The lattice constant a_0 is calculated for all *hkl* (peaks) where *l*=0 i.e., (220), (400) using equation 1:

$$a_0 = d_\alpha \sqrt{h^2 + k^2} = 2.046\sqrt{2^2 + 2^2} = 5.786 \text{ Å} \quad \text{- for } hkl = 220$$

Similarly, for (400), a_0= 5.787 Å

The percentage of measurement error is higher for the lower intensity peaks. Hence, the a_0 value calculated using the measured 2θ of the higher intensity peak (220) is given a higher weightage while averaging to calculate the c_0 value as compared to the a_0 value of the lower intensity peak (400).

The value of c_0 is calculated using equation 1:

$$c^2 = \frac{l^2}{\frac{1}{d^2} - \frac{h^2 + k^2}{a^2}}$$

Lattice parameters for CIGSe sample with No NaF (Sample ID: C16)

Serial	Measured		d_α	Possible Plane Indices			Calculated		*Weighted* Average	
No	2θ	Counts		*h*	*k*	*l*	a_0	c_0	a_0	c_0
1	17.14	155	5.179	1	0	1		11.551	5.786	11.540
2	26.68	3552	3.344	1	1	2		11.579		
3	27.74	181	3.216	1	0	3		11.605		
4	35.62	183	2.525	2	1	1		11.136		
5	42.24	128	2.140	1	0	5		11.514		
6	44.28	1373	2.046	2	2	0	5.786			
7	44.28	1373	2.046	2	0	4		11.571		
8	52.5	645	1.746	1	1	6		11.560		
9	52.5	645	1.746	3	1	2		11.460		
10	64.4	127	1.447	4	0	0	5.787			
11	64.4	127	1.447	0	0	8		11.574		
12	70.86	187	1.33	3	1	6		11.617		
13	81.48	192	1.182	2	2	8		11.575		
14	87.44	201	1.115	3	3	6		11.632		

Lattice parameters for CIGSe sample with 40 Å NaF (Sample ID: C17)

Serial	Measured		Actual	Possible Plane Indices			Calculated		Weighted Average	
No	2q	Counts	d_α	*h*	*k*	*l*	a_0	c_0	a_0	c_0
No	17.16	223	5.167	1	0	1		11.476	5.787	11.565
1	26.66	4291	3.343	1	1	2		11.600		
2	27.72	496	3.218	1	0	3		11.616		
3	35.56	260	2.524	2	1	1		11.466		
4	44.28	1714	2.045	2	2	0	5.786			
5	44.28	1714	2.045	2	0	4		11.569		
6	52.42	615	1.745	1	1	6		11.579		
7	52.42	615	1.745	3	1	2		11.617		
8	64.36	136	1.447	4	0	0	5.790			
9	64.36	136	1.447	0	0	8		11.580		

10	71.02	209	1.327	3	1	6		11.566		
11	81.42	194	1.182	2	2	8		11.584		
12	87.66	159	1.113	3	3	6		11.558		

Lattice parameters for CIGSe sample with 80 Å NaF (Sample ID: C18)

Serial	Measured		Actual	Possible Plane Indices			Calculated		Weighted Average	
No	2q	Counts	d_α	*h*	*k*	*l*	a_0	c_0	a_0	c_0
1	17.16	187	5.167	1	0	1		11.487	5.781	11.531
2	26.7	3752	3.338	1	1	2		11.554		
3	27.68	467	3.222	1	0	3		11.641		
4	35.58	230	2.5232	2	1	1		11.394		
5	44.32	1429	2.043	2	2	0	5.781			
6	44.32	1429	2.043	2	0	4		11.552		
7	52.5	627	1.743	1	1	6		11.560		
8	52.5	627	1.743	3	1	2		11.467		
9	64.48	149	1.445	4	0	0	5.780			
11	64.48	149	1.445	0	0	8		11.561		
12	81.54	161	1.180	2	2	8		11.565		
13	87.54	161	1.114	3	3	6		11.601		

Lattice parameters for CIGSe absorber selenized at 550 ºC for 60 minutes (Sample ID: C38A)

Serial	Measured		d_α	Possible Plane Indices			Calculated		Weighted Average	
No	2q	Counts		*h*	*k*	*l*	a_0	c_0	a_0	c_0
1	17.12	155	5.179	1	0	1		11.618	5.786	11.596
2	26.66	3552	3.344	1	1	2		11.604		
3	27.74	181	3.216	1	0	3		11.605		
4	35.56	183	2.525	2	1	1		11.508		
5	44.28	1373	2.046	2	2	0	5.786			
6	44.28	1373	2.046	2	0	4		11.571		
7	52.4	645	1.746	1	1	6		11.585		
8	52.4	645	1.746	3	1	2		11.685		
9	64.4	127	1.447	4	0	0	5.787			
11	64.4	127	1.447	0	0	8		11.574		
12	70.86	187	1.330	3	1	6		11.617		
13	81.4	192	1.182	2	2	8		11.589		
14	87.44	201	1.115	3	3	6		11.632		

Lattice parameters for CIGSeS absorber selenized at 500 ºC for 25 minutes (Sample ID: C60A)

Serial	Measured		d_α	Possible Plane Indices			Calculated		Weighted Average	
No	2θ	Counts		*h*	*k*	*l*	a_0	c_0	a_0	c_0
1	17.28	16	5.132	1	0	1		11.241	5.658	11.348
2	27.26	441	3.271	1	1	2		11.365		
3	36.2	19	2.481	2	1	1		11.363		
4	45.26	182	2.004	2	2	0	5.667			
5	45.26	182	2.004	2	0	4		11.351		
6	53.72	95	1.706	3	1	2		11.335		
7	53.72	95	1.706	1	1	6		11.319		
8	64.54	19	1.444	3	0	5		11.222		
9	71	25	1.328	3	3	0	5.632			
11	81.52	29	1.181	4	1	5		11.586		

Lattice parameters for CIGSeS absorber selenized at 450 ºC for 45 minutes (Sample ID: C60B)

No	Measured		d_α	Possible Plane Indices			Calculated		Weighted Average	
	2q	Counts		*h*	*k*	*l*	a_0	c_0	a_0	c_0
1	17.6	12	5.039	1	0	1		11.251	5.586	11.168
2	27.62	152	3.230	1	1	2		11.218		
5	45.92	56	1.976	2	2	0	5.590			
6	45.92	56	1.976	2	0	4		11.186		
7	54.56	30	1.682	3	1	2		11.003		
8	54.56	30	1.682	1	1	6		11.154		
9	67.1	8	1.395	0	0	8		11.159		
10	67.1	8	1.395	4	0	0	5.580			

7. REFERENCES

[1] "International Energy Outlook," September 2008, *Report #: DOE/EIA-0484(2008)*, Page 7.

[2] "Fossil Fuel," *http://en.wikipedia.org/wiki/Fossil_fuel*.

[3] "Global Warming," *http://cobwebsandseaslugs.com/global-warming*.

[4] A. Luque and S. Hegedus, "Status, Trends, Challenges and the Bright Future of Solar Electricity," in *Handbook of Photovoltaic Science & Engineering*, A. Luque and S. Hegedus, Eds., John Wiley & Sons, Ltd., 2003, ch. 1, pp. 1-43.

[5] "The History of Solar," *www1.eere.energy.gov/solar/pdfs/solar_timeline.pdf*.

[6] "History: Photovoltaics Timeline," *http://inventors.about.com/od/timelines/a/Photovoltaics.htm*.

[7] "Solar Cell," *http://en.wikipedia.org/wiki/Solar_cell*.

[8] M. A. Barteau and R. L. Pigford, "Perspectives on Energy," *University of Delaware Energy Institute Symposium*, March 17, 2008

[9] R. Nielsen, "How Much Solar Energy Can We Harvest?," *http://home.iprimus.com.au/nielsens/*, 2005.

[10] "2007 World PV Industry Report Highlights," *http://www.solarbuzz.com/Marketbuzz2008-intro.htm*, March 17, 2008.

[11] http://www.earth-policy.org/Indicators/Solar/2007_data.htm.

[12] European Photovoltaic Industry Association, Brussels – Belgium, "Global Market Outlook for Photovoltaics until 2012," Feb 18, 2008.

[13] Thin Film vs Silicon Market Share

[14] J. Zhao, A. Wang, M. A. Green and F. Ferrazza, "19.8% Efficient "Honeycomb" Textured Multicrystalline and 24.4% Monocrystalline Silicon Solar Cells," *Applied Physics Letters*, vol. 73, pp. 1991-1993, 1998.

[15] J. Zhao, A. Wang, F. Yun, G. Zhang, D. M. Roche, S. R. Wenham and M. A. Green, "20,000 PERL silicon cells for the '1996 World Solar Challenge' solar car race," *Progress in Photovoltaics: Research and Applications,* vol. 5, pp. 269–276, 1997.

[16] D. Rose, O. Koehler, N. Kaminar, B. Mulligan and D. King, "Mass Production of PV modules with 18% total-area efficiency and high energy delivery per peak watt," *Conference Record, IEEE 4th World Conference on Photovoltaic Energy Conversion*, Waikoloa, HI, 7–12 May 2006; pp. 2018–2023, 2006.

[17] H. Rao, "Polysilicon prices go through the roof", http://www.projectsmonitor.com/detailnews.asp?newsid=16898, Sep 8-14, 2008.

[18] I. Repins, M.A. Contreras, B. Egaas, C. DeHart, J. Scharf, C.L. Perkins, B. To and R. Noufi, "19.9% Efficient ZnO/CdS/$CuInGaSe_2$ Solar Cell with 81.2% Fill Factor," *Progress in Photovoltaics: Research and Applications*, vol. 16, pp. 235-239, 2008.

[19] Y. Tanaka, N. Akema, T. Morishita, D. Okumura and K. Kushiya, "Improvement of V_{oc} upward of 600mV/cell with CIGS-based absorber prepared by selenization/sulfurization," *Proceedings of the 17th European Photovoltaic Solar Energy Conference*, pp. 989-994, October 2001.

[20] X. Wu, J.C. Keane, R.G. Dhere, C. DeHart, D.S. Albin, A. Duda, T.A. Gessert, S. Asher, D.H. Levi and P. Sheldon, "16.5% Efficient CdS/CdTe Polycrystalline Thin-Film Solar Cells," *Proceedings of the 17th European Photovoltaic Solar Energy Conference,* pp. 995-1000, October 2001.

[21] Steve Bush, "Thin film CdTe solar cells to be 12% efficent in 2012 - First Solar," http://www.electronicsweekly.com/Articles/2008/07/25/44199/thin-film-cdte-solar-cells-to-be-12-efficent-in-2012-first-solar.htm, July 25, 2008.

[22] J. Yang, A. Banerjee, T. Glatfelter, K. Hoffman, X. Xu, S. Guha, "Progress in triple-junction amorphous silicon based alloy solar cells and modules using hydrogen dilution," *Conference Record, 1st World Conference on Photovoltaic Energy Conversion*, Hawaii, pp. 380–385, 1994.

[23] H. S. Ullal and B. Roedern, "Critical issues for commercialization of thin-film PV technologies," *Solid State Technology*, vol. 51, pp. 52-54, 2008.

[24] "Thin film technology set to top 30% of solar cell market by 2015," http://www.semiconductor-today.com/news_items/2008/SEPT/TIN_080908.htm, September 8, 2008.

[25] J. Lindmayer and C. Y. Wrigley, "Semiconductor Junctions or Diodes," in *Fundamentals of Semiconductor Devices*, Princeton, New Jersey: Van Nostrand Reinhold Co., Ch. 2, pp. 16-61, 1965.

[26] S. M. Sze, *Physics of Semiconductor Devices*, New York: Wiley-Interscience, 1981.

[27] "Reference Solar Spectral Irradiance: Air Mass 1.5, " http://rredc.nrel.gov/solar/spectra/am1.5/#about

[28] U. Rau and H.W. Schock, "Cu(In,Ga)Se_2 Solar Cells," in *Clean Electricity from Photovoltaics*, M.D. Archer and R. Hill, Imperial College Press, vol. 1, Ch. 7, pp. 277-345, 2001.

[29] T. Haalboom, T. Gödecke, F. Ernst, M. RuHle, R. Herberholz, H.W. Schock, C. Beilharz and K.W. Benz, "Phase Relation and Microstructure in Bulk Materials and Thin Films of the Ternary System Cu-In-Se," *Proceedings of the 11th International Conference on Ternary and Multinary compounds*, ICTMC-11, University of Salford, pp. 249-252, 1997.

[30] T. Negami, N. Kohara, M. Nishitani, T. Wada and T. Hirao, "Preparation and characterization of $Cu(In_{1-x}Ga_x)_3Se_5$ thin films," *Applied. Physics Letters*, vol. 67, pp. 825-827, 1995.

[31] D. Schmid, M. Ruckh, F. Grunwald and H.W. Schock, "Chalcopyrite/defect chalcopyrite heterojunctions on the basis of $CuInSe_2$," *Journal of Applied Physics*, vol. 73, pp. 2902-2909, 1993.

[32] A. Niemegeers, M. Burgelman, R. Herberholz, U. Rau, D. Hariskos and H.W. Schock, "Model for Electronic Transport in Cu(In,Ga)Se_2 Solar Cells," *Progress in Photovoltaics: Research and Applications*, vol. 6, pp. 407-421, 1998.

[33] H. W. Schock and R. Noufi, "CIGS-based solar cells for the next millennium," *Progress in Photovoltaics: Research and Applications*, vol. 8, pp. 151-160, 2000.

[34] R. Klenk, "Characterisation and modelling of chalcopyrite solar cells," *Thin Solid Films*, vol. 387, pp. 135-140, 2001.

[35] R. Herberholz, U. Rau, H.W. Schock, T. Haalboom, T. Gödecke, F. Ernst, C. Beilharz, K.W. Benz and D. Cahen, "Phase segregation, Cu migration and junction formation in Cu(In, Ga)Se_2," *The European Physical Journal Applied Physics*, vol. 6, pp. 131-139, 1999

[36] W. Hörig, H. Neumann, H. Sobotta, B. Schumann and G. Kühn, "The optical properties of $CuInSe_2$ thin films," *Thin Solid Films*, vol. 48, pp. 67-72, 1978.

[37] L.L. Kazmerski, F.R. White, M.S. Ayyagari, Y.J. Juang and R.P. Patterson, "Growth And Characterization of Thin-Film Compound Semiconductor Photovoltaic Heterojunctions," *Journal of Vacuum Science Technology*, vol. 14, pp. 65-68, 1977.

[38] G. Hodes, T. Engelhard, D. Cahen, L.L. Kazmerski and C.R. Herrington, "Electroplated $CuInS_2$ and $CuInSe_2$ layers: Preparation and physical and photovoltaic characterization," *Thin Solid Films*, vol. 128, pp. 93-106, 1985.

[39] B. M. Basol, V. K. Kapur, A. Halani, C. R. Leidholm, J. Sharp, J. R. Sites, A. Swartzlander, R. Matson, and H. Ullal, "Cu(In,Ga)Se_2 thin films and solar cells prepared by selenization of metallic precursors," *Journal of Vacuum Science & Technology A: Vacuum, Surfaces, and Films,* vol. 14, pp. 2251-2256, 1996.

[40] M. Marudachalam, R. W. Birkmire, H. Hichri, J. M. Schultz, A. Swartzlander, and A. M. M. Jassim, "Phases, morphology, and diffusion in $CuIn_xGa_{1-x}Se_2$ thin films," *Journal of Applied Physics*, vol. 82, pp. 2896-2905, 1997.

[41] N.G. Dhere, S.S. Kulkarni, A.H. Jahagirdar and A.A. Kadam, "Composition and morphology of partially selenized $CuIn_{1-x}Ga_xSe_2$ thin films prepared using diethylselenide (DESe) as selenium source," *Journal of Physics and Chemistry of Solids*, vol. 66, pp. 1876-1879, 2005.

[42] R.W. Birkmire, L.C. DiNetta, P.G. Lasswell, J.D. Meakin and J.E. Phillips, "High efficiency $CuInSe_2$ based heterojunction solar cells: Fabrication and results," *Solar Cells*, vol. 16, pp. 419-427, 1986.

[43] M.A. Contreras, B. Egaas, K. Ramanathan, J. Hiltner, A. Swartzlander, F. Hasoon and R. Noufi, "Progress toward 20% efficiency in Cu(In,Ga)Se_2 polycrystalline thin-film solar cells," *Progress in Photovoltaics: Research and Applications*, vol. 7, pp. 311-316, 1999.

[44] W.N. Shafarman and J. Zhu, "Effect of substrate temperature and deposition profile on evaporated Cu(InGa)Se_2 films and devices," *Thin Solid Films*, vol. 361-362, pp. 473-477, 2000.

[45] T. Negami, Y. Hashimoto and S. Nishiwaki, "Cu(In,Ga)Se_2 thin-film solar cells with an efficiency of 18%," *Solar Energy Materials and Solar Cells*, vol. 67, pp. 331-335, 2001.

[46] J. Piekoszewski, J.J. Loferski, R. Beaulieu, J. Beall, B. Roessler and J. Shewchun, "RF-sputtered $CuInSe_2$ thin films," *Solar Energy Materials,* vol. 2, pp. 363-372, 1980

[47] V.K. Kapur, B.M. Basol and E.S. Tseng, "Low cost methods for the production of semiconductor films for $CuInSe_2$/CdS solar cells," *Solar Cells*, vol. 21, pp. 65-72, 1987

[48] Y. Ueno, H. Kawai, T. Sugiura and H. Minoura, "Electrodeposition of $CuInSe_2$ films from a sulphate bath," *Thin Solid Films*, vol. 157, pp. 159-168, 1988.

[49] V.K. Kapur, A. Bansal, P. Le and O.I. Asensio, "Non-vacuum processing of $CuIn_{1-x}Ga_xSe_2$ solar cells on rigid and flexible substrates using nanoparticle precursor inks," *Thin Solid Films*, vol. 431-432, pp. 53-57, 2003.

[50] T.F. Ciszek, "Growth and properties of $CuInSe_2$ crystals produced by chemical vapor transport with iodine," *Journal of Crystal Growth,* vol. 70, pp. 405-410, 12. 1984.

[51] J.A. Thornton, T.C. Lommasson, H. Talieh and B. Tseng, "Reactive sputtered $CuInSe_2$," *Solar Cells*, vol. 24, pp. 1-9, 1988.

[52] K.R. Murali, "Preparation and characterization of chemically deposited $CuInSe_2$ films," *Thin Solid Films*, vol. 167, pp. L19-L22, 1988.

[53] L.D. Laude, M.C. Joliet and C. Antoniadis, "Laser-induced synthesis of thin $CuInSe_2$ films," *Solar Cells,* vol. 16, pp. 199-209, 1986.

[54] C. R. Abernathy, Jr, A. A. Anani, B. Haba, and G. Smestad, "Production of single phase chalcopyrite $CuInSe_2$ by spray pyrolysis," *Applied Physics Letters*, vol. 45, pp. 890-892, 1984.

[55] C.W. Bates, K.F. Nelson, S. Atiq Raza, J.B. Mooney, J.M. Recktenwald, L. Macintosh and R. Lamoreaux, "Spray pyrolysis and heat treatment of $CuInSe_2$ for photovoltaic applications," *Thin Solid Films*, vol. 88, pp. 279-283, 1982.

[56] J. Bougnot, S. Duchemin and M. Savelli, "Chemical spray pyrolysis of $CuInSe_2$ thin films," *Solar Cells*, vol. 16, pp. 221-236, 1986.

[57] B. Schumann, A. Tempel and G. Kühn, "Epitaxial layers of $CuInSe_2$," *Solar Cells,* vol. 16, pp. 43-63, 1986.

[58] H. Takenoshita, "Liquid phase epitaxial growth and electrical characterization of $CuInSe_2$," *Solar Cells*, vol. 16, pp. 65-89, 1986.

[59] K. Guenoun, K. Djessas, and G. Massé, "Temperature distribution and transport mode in a close-spaced vapor transport reactor for $CuInSe_2$ depositions," *Journal of Applied Physics*, vol. 84, no. 1, pp. 589-595, 1998.

[60] K. Zweibel, "Harnessing Solar Power: The Photovoltaic challenge," ISBN 0-306-43564-0, 1st ed., Plenum Publishing, New York, 1990.

[61] S.F. Chichibu, M. Sugiyama, M. Ohbasami, A. Hayakawa, T. Mizutani, H. Nakanishi, T. Negami and T. Wada, "Use of diethylselenide as a less-hazardous source for preparation of CuInSe2 photo-absorbers by selenization of metal precursors," *Journal of Crystal Growth*, vol. 243, pp. 404-409, 2002.

[62] A. Kadam, "Preparation of efficient $CuIn_{1-x}Ga_xSe_{2-y}S_y$/CdS thin-film solar cells by optimizing the molybdenum back contact and using diethylselenide as selenium precursor," Orlando, Fla.: University of Central Florida; pp. 139, 2006. Available: http://purl.fcla.edu/fcla/etd/CFE0001035.

[63] Dimmler, H. Dittrich, R. Menner, and H.W. Schock, "Performance and Optimization of Heterojunctions Based on Cu(Ga,In)Se_2", *Proceedings of 19th IEEE Photovoltaic Specialist Conference*, New York, 1454, 1987.

[64] D.S. Albin,. J.J.. Carapella, J.R. Tuttle, and. R. Noufi, *Material Research Society Symposium Proceedings*, vol. 228, pp. 267-272, 1991.

[65] M. Kemell, M. Ritala and M. Leskela, "Thin Film Deposition Methods for $CuInSe_2$ Solar Cells," *Critical Reviews in Solid State and Material Sciences,* vol. 30, pp. 1-31, 2005.

[66] H. Dittrich, U. Prinz, J. Szot and H.W. Schock, "Analysis of Reaction Kinetics of Selenized $CuInSe_2$ and $CuGaSe_2$ Thin Films," *Proceedings 9th European Community Photovoltaic Solar Energy Conference*, pp. 163, 1989.

[67] S. H. Wei, S. B. Zhang, and A. Zunger, "Effects of Ga addition to $CuInSe_2$ on its electronic, structural, and defect properties," *Applied Physics Letters,* vol. 72, pp. 3199-3201, 1998.

[68] T. Dullweber, O. Lundberg, J. Malmström, M. Bodegård, L. Stolt, U. Rau, H.W. Schock and J.H. Werner, "Back surface band gap gradings in $Cu(In,Ga)Se_2$ solar cells," *Thin Solid Films*, vol. 387, pp. 11-13, 2001.

[69] R. Klenk, U. Blieske, V. Dieterle, K. Ellmer, S. Fiechter, I. Hengel, A. Jäger-Waldau, T. Kampschulte, C. Kaufmann, J. Klaer, M.C. Lux-Steiner, D. Braunger, D. Hariskos, M. Ruckh and H.W. Schock, "Properties of $CuInS_2$ thin films grown by a two-step process without H_2S," *Solar Energy Materials and Solar Cells*, vol. 49, pp. 349-356, 1997.

[70] A. Rockett, "Performance-limitations in Cu(In,Ga)Se2-based heterojunction solar cell," *Proceedings of 29th IEEE Photovoltaic Specialists Conference*, pp. 587-591, 2002.

[71] T. Nakada, H. Ohbo, T. Watanabe, H. Nakazawa, M. Matsui and A. Kunioka, "Improved $Cu(In,Ga)(S,Se)_2$ thin film solar cells by surface sulfurization," *Solar Energy Materials and Solar Cells*, vol. 49, pp. 285-290, 1997.

[72] L. Stolt, J. Hedström, J. Kessler, M. Ruckh, K. O. Velthaus, and H. W. Schock, "ZnO/CdS/$CuInSe_2$ thin-film solar cells with improved performance," *Applied Physics Letters*, vol. 62, pp. 597-599, 1993.

[73] D. Rudmann, D. Bremaud, A.F. da Cunha, G. Bilgec, A. Strohc, M. Kaelin, H. Zogga, A.N. Tiwarid, "Sodium incorporation strategies for CIGS growth at different temperatures" *Thin Solid Films*, vol. 480–481, pp. 55– 60. 2005.

[74] Jorg Palm , Volker Probst, Franz H. Karg, "Second generation CIS solar modules" *Solar Energy*, vol. 77, pp. 757–765, 2004.

[75] K. Granath, M. Bodegard, and L. Stolt, "The effect of NaF on $Cu(In,Ga)Se_2$ Thin Film Solar Cells," *Solar Energy Materials and Solar Cells*, vol. 60, pp. 279-293, 2000.

[76] J. E. Granata, J. R. Sites, S. Asher, and R. Matson, "Quantitative incorporation of sodium in $CuInSe_2$ and $Cu(In,Ga)Se_2$ photovoltaic devices," *Proceedings of 26th IEEE Photovoltaic Specialists Conference*, pp. 387-390, 1997.

[77] Rockett, J. S. Britt, T. Gillespie, C. Marshall, M. M. Al Jassim, F. Hasoon, R. Matson, and B. Basol, "Na in selenized Cu(In,Ga)Se_2 on Na-containing and Na-free glasses: Distribution, Grain structure, and Device performances," *Thin Solid Films*, vol. 372, pp. 212-217, 2000.

[78] M. Ruckh, D. Schmid, M. Kaiser, R. Schaffler, T. Walter, and H. W. Schock, "Influence of substrates on the electrical properties of Cu(In,Ga)Se_2 thin films," *Proceedings of the IEEE First World Conference on Photovoltaic Energy Conversion*, vol. 1, pp. 156-159, 1994.

[79] M. Bodegård, K. Granath and L. Stolt, "Growth of Cu(In,Ga)Se_2 thin films by coevaporation using alkaline precursors," *Thin Solid Films*, vol. 361-362, pp. 9-16, 2000.

[80] J. Hedstrom, H. Ohlsen, M. Bodegard, A. Kylner, L. Stolt, D. Hariskos, M. Ruckh and H.-. Schock, "ZnO/CdS/Cu(In,Ga)Se_2 thin film solar cells with improved performance," *Proceedings of the 23rd IEEE Photovoltaic Specialists Conference*, 1993., pp. 364-371, 1993.

[81] D. Rudmann, G. Bilger, M. Kaelin, F.-. Haug, H. Zogg and A.N. Tiwari, "Effects of NaF coevaporation on structural properties of Cu(In,Ga)Se_2 thin films," *Thin Solid Films*, vol. 431-432, pp. 37-40, 2003.

[82] M. Lammer, U. Klemm and M. Powalla, "Sodium co-evaporation for low temperature Cu(In,Ga)Se_2 deposition," *Thin Solid Films*, vol. 387, pp. 33-36, 2001.

[83] M.A. Contreras, B. Egaas, P. Dippo, J. Webb, J. Granata, K. Ramanathan, S. Asher, A. Swartzlander and R. Noufi, "On the role of Na and modifications to Cu(In,Ga)Se_2 absorber materials using thin-MF (M=Na, K, Cs) precursor layers [solar cells]," *Proceedings of the 26th IEEE Photovoltaic Specialists Conference*, pp. 359-362, 1997.

[84] B.M. Keyes, F. Hasoon, P. Dippo, A. Balcioglu and F. Abulfotuh, "Influence of Na on the electro-optical properties of Cu(In,Ga)Se_2," *Proceedings of the 26th IEEE Photovoltaic Specialists Conference*, 1997., pp. 479-482, 1997.

[85] T. Nakada, D. Iga, H. Ohbo and A. Kunioka, "Effects of Sodium on Cu(In,Ga)Se_2-Based Thin Films and Solar Cells," *Japanese Journal of Applied Physics*, vol. 36, pp. 732-737, 1997.

[86] J.E. Granata, J.R. Sites, S. Asher and R.J. Matson, "Quantitative incorporation of sodium in $CuInSe_2$ and Cu(In,Ga)Se_2 photovoltaic devices," *Proceedings of the 26th IEEE Photovoltaic Specialists Conference*, 1997., pp. 387-390, 1997.

[87] S. H. Wei, S. B. Zhang, and A. Zunger, "Effects of Na on the electrical and structural properties of $CuInSe_2$," *Journal of Applied Physics*, vol. 85, no. 10, pp. 7214-7218, 1999.

[88] U. Rau and H.W. Schock, "Electronic properties of Cu(In,Ga)Se_2 heterojunction solar cells - recent achievements, current understanding, and future challenges," *Applied Physics A: Materials Science & Processing*, vol. 69, pp. 131-147, 1999.

[89] D. Cahen and R. Noufi, "Defect chemical explanation for the effect of air anneal on CdS/$CuInSe_2$ solar cell performance," *Applied Physics Letters*, vol. 54, pp. 558-560, 1989.

[90] L. Kronik, U. Rau, J. Guillemoles, D. Braunger, H. Schock and D. Cahen, "Interface redox engineering of Cu(In,Ga)Se_2 - based solar cells: oxygen, sodium, and chemical bath effects," *Thin Solid Films*, vol. 361-362, pp. 353-359, 2000.

[91] D. Braunger, D. Hariskos, G. Bilger, U. Rau and H.W. Schock, "Influence of sodium on the growth of polycrystalline Cu(In,Ga)Se_2 thin films," *Thin Solid Films*, vol. 361-362, pp. 161-166, 2000.

[92] T. Wada, N. Kohara, S. Nishiwaki and T. Negami, "Characterization of the Cu(In,Ga)Se_2/Mo interface in CIGS solar cells," *Thin Solid Films*, vol. 387, pp. 118-122, 2001.

[93] N. K. Shiro Nishiwaki, Takayuki Negami, and Takahiro Wada, "$MoSe_2$ Layer Formation at the Cu(In,Ga)Se_2/Mo Interfaces in High Efficiency Cu($In_{1-x}Ga_x$)Se_2 Solar Cells," *Japanese Journal of Applied Physics*, vol. 37, pp. L71-L73, 1998.

[94] P. A. G. O'Hare, I. R. Tasker, J. M. Tarascon, "A Flourine-Combustion Calorimetric Study of Two Molybdenum Selenides: $MoSe_2$ and Mo_6Se_6," *Journal of Chemical Thermodynamics*, vol. 19, pp. 61-68, 1987.

[95] N. K. T. Wada, S. Nishiwaki, T. Negami, "Characterization of the Cu(In,Ga)Se_2/Mo interface in CIGS Solar Cells," *Thin Solid Films*, vol. 387, pp. 118-122, 2001.

[96] W. N. Shafarman and J. E. Phillips, "Direct current-voltage measurements of the Mo/CuInSe2 contact on operating solar cells," *Proceedings of the 25th IEEE Photovoltaic Specialists Conference, 1996.,* pp. 917-919, 1996.

[97] D. F. M. R. Wurz, A. Meeder, A. Rumberg, S. M. Babu, Th. Schedel-Niedrig, U. Bloeck, P. Schubert-Bischoff, M. Ch. Lux-Steiner, "Formation of an Interfacial $MoSe_2$ layer in CVD Grown $CuGaSe_2$ Based Thin Film Solar Cells," *Thin Solid Films*, vol. 431-432, pp. 398-402, 2003.

[98] P. Garg, A. Garg, A. C. Rastogi, and J. C. Garg, "Growth and characterization of electrodeposited cuinse2 thin films from seleno-sulphate solution," *Journal of Physics D: Applied Physics*, vol. 24, no. 11, pp. 2026-2031, 1991.

[99] S. N. Sahu, R. D. L. Kristensen, and D. Haneman, "Electrodeposition of $CuInSe_2$ thin films from aqueous solution," *Solar Energy Materials*, vol. 18, pp. 385-397, 1989.

[100] C. X. Qiu and I. Shih, "Investigation of electrodeposited $CuInSe_2$ films," *Canadian Journal of Physics*, vol. 65, pp. 1011-1014, 1987.

[101] V. K. Kapur, B. M. Basol, and E. S. Tseng, "Low cost methods for the production of semiconductor films for $CuInSe_2$/CdS solar cells," *Solar Cells*, vol. 21, pp. 65-72, 1987.

[102] S. N. Qiu, L. Li, C. X. Qiu, I. Shih, and C. H. Champness, "Study of $CuInSe_2$ thin films prepared by electrodeposition," *Solar Energy Materials and Solar Cells*, vol. 37, pp. 389-393, 1995.

[103] W.N. Shafarman and L. Stolt, "$Cu(InGa)Se_2$ Solar Cells," in Handbook of Photovoltaic Science & Engineering, A. Luque and S. Hegedus, Eds., John Wiley & Sons, Ltd, 2003, ch. 13, pp. 567-616.

[104] M. A. Contreras, M. J. Romero, B. To, F. Hasoon, R. Noufi, S. Ward, and K. Ramanathan, "Optimization of CBD CdS process in high-efficiency $Cu(In,Ga)Se_2$-based solar cells," *Thin Solid Films*, vol. 403-404, pp. 204-211, 2002.

[105] S. N. Qiu, W. W. Lam, C. X. Qiu, and I. Shih, "ZnO/CdS/$CuInSe_2$ photovoltaic cells fabricated using chemical bath deposited CdS buffer layer," *Applied Surface Science*, vol. 113-114, pp. 764-767, 1997.

[106] Y. Hashimoto, N. Kohara, T. Negami, N. Nishitani and T. Wada, "Chemical bath deposition of Cds buffer layer for CIGS solar cells," *Solar Energy Materials and Solar Cells*, vol. 50, pp. 71-77, 1998.

[107] S. Ishizuka, K. Sakurai, A. Yamada, K. Matsubara, P. Fons, K. Iwata, S. Nakamura, Y. Kimura, T. Baba, and H. Nakanishi, "Fabrication of wide-gap $Cu(In_{1-x}Ga_x)Se_2$ thin film solar cells: a study on the correlation of cell performance with highly resistive i-zno layer thickness," *Solar Energy Materials and Solar Cells*, vol. 87, no. 1-4, pp. 541-548, 2005.

[108] J. Schoenes, K. Kanazawa, and E. Kay, "Band and hopping conduction in high-resistivity ZnO," *Journal of Applied Physics*, vol. 48, no. 6, pp. 2537-2542, 1977.

[109] G. Neumann, "On the defect structure of zinc-doped zinc oxide," *physica status solidi (b)*, vol. 105, no. 2, pp. 605-612, 1981.

[110] T. Nakada, N. Murakami, A. Kunioka, "Comparison between Al- and B-doped ZnO window layers for $CuInSe_2$ thin film solar cells," *Material Research Society Symposium*, Vol. 426, pp. 411-410, 1996.

[111] B. Choi, H. B. Im, J. S. Song, and K. H. Yoon, "Optical and electrical properties of Ga_2O_3-doped ZnO films prepared by r.f. sputtering," *Thin Solid Films*, vol. 193-194, pp. 712-720, 1990.

[112] J. Duenow, T. Gessert, D. Wood, D. Young, and T. Coutts, "Effects of hydrogen content in sputtering ambient on ZnO:Al electrical properties," *Journal of Non-Crystalline Solids*, vol. 354, pp. 2787-2790, 2008.

[113] R. Cebulla, R. Wendt, and K. Ellmer, "Al-doped zinc oxide films deposited by simultaneous rf and dc excitation of a magnetron plasma: Relationships between plasma parameters and structural and electrical film properties," *Journal of Applied Physics*, vol. 83, pp. 1087-1095, 1998.

[114] W. D. Westwood, "Reactive Sputter Deposition," in *Handbook of Plasma Processing Technology: Fundamentals, Etching, Deposition, and Surface Interactions*, S. M. Rossnagel, J. J. Cuomo and W. D. Westwood, Eds., Park Ridge, N.J., U.S.A: Noyes Publications, Ch. 9, pp. 233-259, 1990.

[115] D. Tarrant and R. Gay, *Proceedings 2001 NCPV Program Review Meeting*, pp. 113–114, 2001.

[116] L. Stolt, J. Hedstrom, and J. Skarp, "CIS solar cells with ZnO windows deposited by ALE," *1994 IEEE First World Conference on Photovoltaic Energy Conversion,* vol. 1, pp. 250-253, 1994.

[117] Wang, J. Dai, J. Cheng, M. P. Chudzik, T. J. Marks, R. P. H. Chang, And C. R. Kannewurf, "Charge Transport, Optical Transparency, Microstructure, And Processing Relationships In Transparent Conductive Indium-Zinc Oxide Films Grown By Low-Pressure Metal Organic Chemical Vapor Deposition," *Applied Physics Letters*, vol. 73, pp. 327–329, 1998.

[118] M. Hiramatsu, K. Iameda, N. Horio, And M. Nawata, "Transparent Conducting ZnO Thin Films Prepared By Xecl Excimer Laser Ablation," *Journal Of Vacuum Science And Technology A*, vol. 16, pp. 669– 673, 1998.

[119] E. Jim´Enez-Gonz´Alez, J. A. S. Urueta, And R. Su´Arez-Parra, "Optical And Electrical Characteristics Of Aluminum Doped ZnO Thin Films Prepared By Solgel Technique," *Journal Of Crystal Growth*, vol. 192, pp. 430–438, 1998.

[120] S. Ashour, S. Alkuhaimi, H. Moutinho, R. Matson and F. Abou-Elfotouh, "Junction formation and characteristics of CdS/$CuInSe_2$/metal interfaces," Thin Solid Films, vol. 226, pp. 129-134, 1993.

[121] E. Moons, T. Engelhard and D. Cahen, "Ohmic contacts to *p*-$CuInSe_2$ crystals," Journal of Electronic Materials, vol. 22, pp. 275-280, 1993.

[122] K. Orgassa, H. W. Schock, J. H. Werner, "Alternative back contact materials for thin film $Cu(In,Ga)Se_2$ solar cells," *Thin Solid Films*, vol. 431 –432, pp. 387–391, 2003.

[123] K. Granath, A. Rockett, M. Bodegård, C. Nender, L. Stolt, "Mechanical Issues of Mo Back Contact for $Cu(In,Ga)Se_2$," 13th European Photovoltaic Solar Energy Conference, pp. 1983, 1995.

[124] N. G. Dhere, V. S. Gade, A. A. Kadam, A. H. Jahagirdar, S. S. Kulkarni and S. M. Bet, "Development of CIGS2 Thin Film Solar Cells," Materials Science and Engineering B, vol. 116, pp. 303, 2005.

[125] E N Deryagina, M G Voronkov, N A Korchevin, “Selenium- and tellurium-centred radicals”, Russian Chemical Reviews, vol. 62, pp. 1107-1117, 1993.